Borohydride-Scaffolded Li/Na/Mg Fast Ionic Conductors for Promising Solid-State Electrolytes

Jing Cuan, You Zhou, Tengfei Zhou, Shigang Ling, Kun Rui, Zaiping Guo,* Huakun Liu, and Xuebin Yu*

Borohydride solid-state electrolytes with room-temperature ionic conductivity up to ≈70 mS cm^{-1} have achieved impressive progress and quickly taken their place among the superionic conductive solid-state electrolytes. Here, the focus is on state-of-the-art developments in borohydride solid-state electrolytes, including their competitive ionic-conductive performance, current limitations for practical applications in solid-state batteries, and the strategies to address their problems. To open, fast Li/Na/Mg ionic conductivity in electrolytes with BH$_4^-$ groups, approaches to engineering borohydrides with enhanced ionic conductivity, and later on the superionic conductivity of polyhedral borohydrides, their correlated conductive kinetics/thermodynamics, and the theoretically predicted high conductive derivatives are discussed. Furthermore, the validity of borohydride pairing with coated oxides, sulfur, organic electrodes, MgH$_2$, TiS$_2$, Li$_4$Ti$_5$O$_{12}$, electrode materials, etc., is surveyed in solid-state batteries. From the viewpoint of compatible cathodes, the stable electrochemical windows of borohydride solid-state electrolytes, the electrode/electrolyte interface behavior and battery device design, and the performance optimization of borohydride-based solid-state batteries are also discussed in detail. A comprehensive coverage of emerging trends in borohydride solid-state electrolytes is provided and future maps to promote better performance of borohydride SSEs are sketched out, which will pave the way for their further development in the field of energy storage.

1. Introduction

The development of batteries with higher specific energy, eliminated risk of explosion, and extended service lifetime is crucial to satisfy the stringent demands for large-scale energy-storage devices and for various types of consumer electronics. All-solid-state rechargeable batteries (ASSBs) utilizing solid-electrolyte separators rather than combustible liquid electrolytes possess the inherent advantages of enhanced safety and stability for state-of-the-art battery technologies.[1] Recently, ASSBs have attracted a resurgence of interest as ideal candidates for the next generation of electrochemical-energy-storage devices. The superiority of ASSBs could be ascribed to the distinctive attributes of solid-state electrolytes (SSEs), including high Li-ion transference number and safety, and comparable ionic conductivity to their liquid counterparts.[2] The adoption of SSEs could offer new opportunities for the high-temperature electrical-energy-storage market and pave the way for the utilization of high-capacity electrodes, such as Li, Na, and sulfur.[2c,3] In contrast, in conventional batteries employing liquid electrolytes, the high-capacity electrodes may meet with detrimental side reactions, causing problems such as dendrite growth, reactivity, and/or dissolution in the solvent.[4,5] With the construction of rigid solid electrolyte separators and stable interfaces in ASSBs, dendrite growth can be effectively mitigated, thus improving the safety of the batteries.[4,6] Owing to these benefits, in battery research, the number of studies on fabricating superionic SSEs has grown rapidly. Despite great progress gained these years, issues

Dr. J. Cuan, Dr. T. Zhou, Dr. K. Rui, Prof. Z. Guo, Prof. H. Liu
Institute for Superconducting and Electronic Materials
University of Wollongong
Wollongong, NSW 2522, Australia
E-mail: zguo@uow.edu.au
Dr. Y. Zhou
Faculty of Materials Science and Chemical Engineering
Ningbo University
Ningbo 315211, Zhejiang, China

Dr. T. Zhou
Key Laboratory of Catalysis and Materials Science of the State Ethnic
Affairs Commission and Ministry of Education
South-Central University for Nationalities
Wuhan 430074, P. R. China
Dr. S. Ling
Beijing National Laboratory for Condensed Matter Physics
Institute of Physics
Chinese Academy of Sciences
Beijing 100190, China
Prof. X. Yu
Department of Materials Science
Fudan University
Shanghai 200433, China
E-mail: yuxuebin@fudan.edu.cn

1803533 (1 of 31)

including sluggish interfacial kinetics,[7] chemomechanical coupling (loss of contact and inefficient utilization of active material induced by chemical expansion of working electrodes),[8] and relatively poor electrochemical stability of SSEs at the cathode side[9] still impede the achievement of reliable ASSBs and remain as challenges to be addressed.[10]

Hitherto, the actively investigated inorganic SSEs have included oxides (sodium and lithium superionic conductors (NASICON and LISICON), perovskites, and garnet-type oxides), sulfides (chalcogenides and thiophosphates), and borohydrides in the complex hydride family, which present ionic conductivities from $\approx 10^{-3}$ to several tens of milli-Siemens per centimeter (mS cm^{-1}) (**Figure 1**a).[11–14]

More specifically, a variety of oxide SSEs have been developed in the past few years, with representatives from the garnet series such as $Li_3Ln_3Te_2O_{12}$ (Ln = Y, Pr, Nd, Sm–Lu) (Li$_3$-phases), $Li_{3+x}Nd_3Te_{2-x}Sb_xO_{12}$ (x = 0.05–1.5), $Li_5La_3M_2O_{12}$ (M = Nb, Ta, Sb) (Li$_5$-phases), $Li_6ALa_2M_2O_{12}$ (A = Mg, Ca, Sr, Ba; M = Nb, Ta) (Li$_6$-phases), and $Li_7La_3M_2O_{12}$ (M = Zr, Sn) (Li$_7$-phases).[15] Some representative NASICONs include $L_{1+x}M^{4+}_{2-x}M'^{3+}_x(PO_4)_3$ (L = Li or Na; M = Ti, Ge, Sn, Hf, or Zr; and M' = Cr, Al, Ga, Sc, Y, In, or La), which have MO_6 octahedra linked with PO_4 tetrahedra through corner sharing in alternating sequences.[12d] Owing to the stiffness and brittleness of ceramic oxide SSEs, harsh technological standards have restricted the fabrication of oxide-based ASSBs.[16] In addition, the preparation of electrode composites (cathode/oxide SSEs) needs further high-temperature sintering to ensure intimate contact,[16c] which results in complicated and costly manufacturing processes, and may block their large-scale production.

Sulfides with representative series of $Li_{10}MP_2S_{12}$ (M = Si, Ge, or Sn), $Na_{10}SnP_2S_{12}$, $Li_{9.54}Si_{1.74}P_{1.44}S_{11.7}Cl_{0.3}$, and $Li_{11}Si_2PS_{12}$[14,17] could exhibit ionic conductivities in the range of 10^{-2} to 10^{-3} S cm^{-1} at room temperature (RT), and their good ductility enables much simplified fabrication techniques for ASSBs, avoiding the high-temperature sintering process. The combined results of experiments and first-principles computations, however, suggest only limited electrochemical stability for sulfide SSEs. For example, $Li_{10}GeP_2S_{12}$ was suggested to be stable only in the voltage range of 1.71–2.14 V. When charged above 2.14 V, the delithiation of $Li_{10}GeP_2S_{12}$ to Li_3PS_4, S, and GeS_2 may start, and the reduction of $Li_{10}GeP_2S_{12}$ to Li_4GeS_4, P, and Li_2S may commence from 1.71 V.[18] To suppress the decomposition of sulfide SSEs and ensure the good operation of solid-state batteries, two strategies may be effective: i) applying artificial coating layers at the cathode/electrolyte and anode/electrolyte interfaces, or ii) limiting the voltage of the battery at the sacrifice of energy density or cost.

In contrast to oxide and sulfide SSEs, borohydride SSEs in the complex hydride family have emerged as promising candidates for large-scale energy storage, which may benefit from their intrinsic features and the inherited merits of complex hydrides (Figure 1b). Complex hydrides have been widely studied as hydrogen-storage materials, and they are usually composed of a metal cation (alkali metal and alkaline-earth metal ions such as Li$^+$, Na$^+$, AND Mg^{2+}) and a complex anion ($[BH_4]^-$, $[NH_2]^-$, $[AlH_4]^-$, $[AlH_6]^{3-}$, etc.).[19] The intrinsic nature of complex hydrides makes them reliable for integration into ASSBs, with their favorable properties including low grain-boundary resistance,

Jing Cuan received her Master's degree in chemistry from Tongji University in 2014, and she is currently a Ph.D. student in the Institute for Superconducting and Electronic Materials at the University of Wollongong under the supervision of Prof. Zaiping Guo. Her current research is focused on solid-state electrolytes, novel nanomaterials design, and the preparation of Li/Na rechargeable batteries.

Zaiping Guo received her Ph.D. degree in materials engineering from the University of Wollongong in December 2003. She is a Senior Professor in the school of Mechanical, Materials, Mechatronic, and Biomedical Engineering, University of Wollongong. She received the Queen Elizabeth II Fellowship in 2010 and a Future Fellowship (FT3) in 2015 from the Australian Research Council. Her research is focused on the design and application of nanomaterials for energy storage and conversion, including rechargeable batteries, hydrogen storage, and fuel cells.

Xuebin Yu received his Ph.D. degree from the Shanghai Institute of Microsystem and Information Technology, Chinese Academy of Science in 2004. He then worked as a postdoctoral fellow at the University of Nottingham and the University of Wollongong from January 2005 to December 2006 and March 2007 to March 2008, respectively. In 2008, he joined Fudan University and now works as a professor in the Department of Materials. His research interests cover hydrogen storage, fuel-cell integration with hydrogen systems, hydride-based solid-state electrolytes, lithium/sodium-ion batteries, and preparation of nanomaterials for energy storage.

ion selectivity, reduction stability, mechanical flexibility, easy device integration, and low processing costs, while their practical application as SSEs has fallen behind due to their unsatisfactory ionic conductivity.[20] In 1979, Boukamp and Huggins discovered Li_2NH with an ionic conductivity of 3×10^{-4} S cm^{-1} at low temperature, which was the first reported Li$^+$ fast ionic conductor
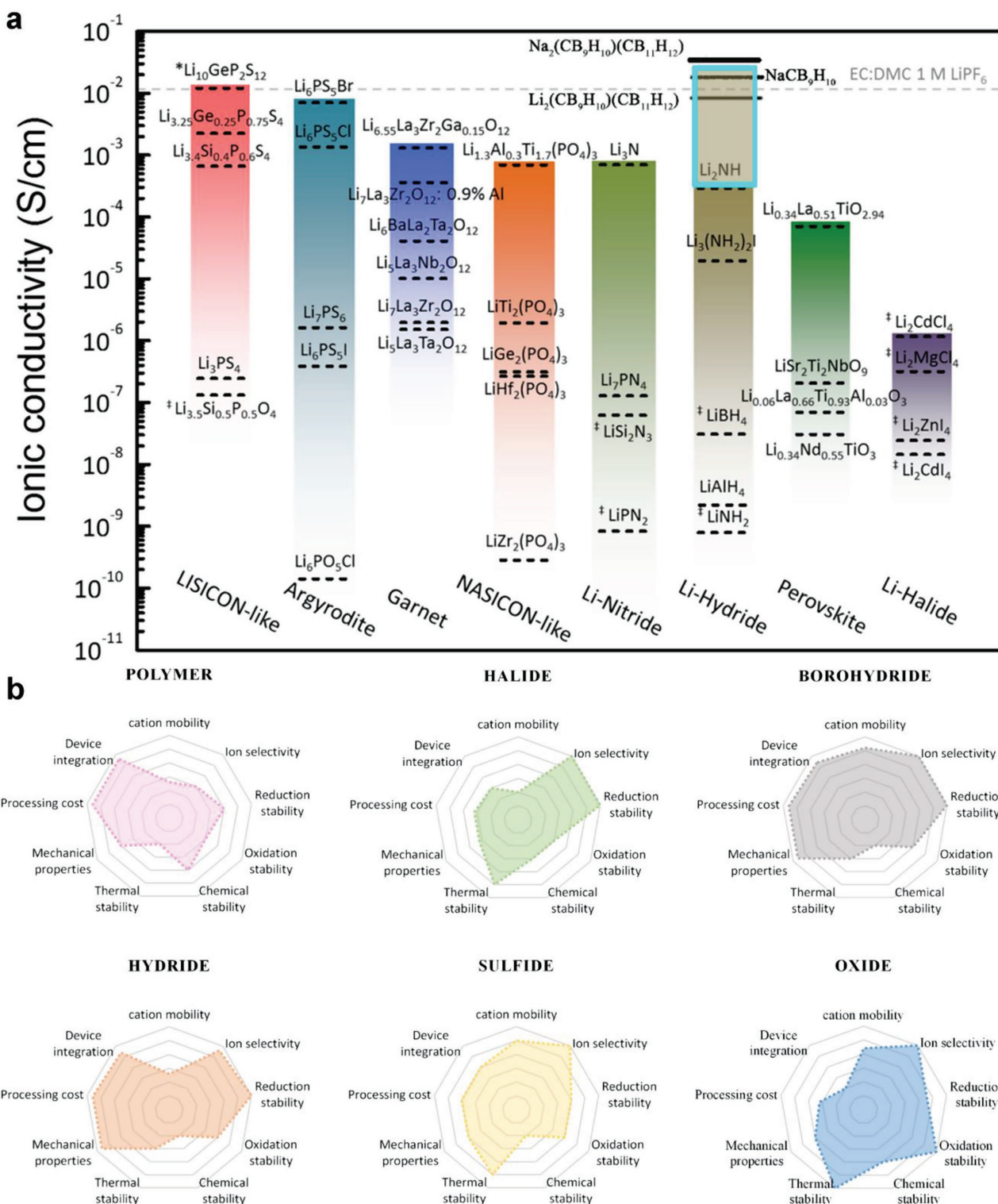
Figure 1. a) Summary of the reported ionic conductivities in different families of SSEs at room temperature. b) Comparisons of properties relevant to the evaluation of SSEs: for polymer SSEs, halide SSEs, borohydride SSEs, hydride SSEs, sulfide SSEs, and oxide SSEs. a) Adapted with permission.[12d] Copyright 2016, American Chemical Society. b) Adapted with permission.[20] Copyright 2017, Springer Nature.

in the complex hydride family,[21] and for a long time, there was only a little subsequent research regarding Li^+/Na^+ conduction in complex hydrides.[19b] $LiNH_2$ exhibits an ionic conductivity of 4×10^{-10} S cm^{-1} at 300 K.[19b] $LiAlH_4$ and Li_3AlH_6 present ionic conductivities of 5×10^{-6} S cm^{-1} (393 K) and 2×10^{-5} S cm^{-1} (393 K), respectively.[22] The turning point came after the first

discovery of the ionic conductivity of borohydride in 2007 and the following successful preparation of RT-stabilized, highly conductive hexagonal $LiBH_4$ in 2009.[23] In particular, in the last three years, polyhedral borohydrides have featured RT Li^+ and Na^+ conductivities that even reach above 0.01 S cm^{-1}, which quickly put them among the leading ionic-conductive electrolytes.[24] Additionally, in consideration of their different types of crystal structures, Li^+ coordination numbers, anion valences, and ionic radii, the structural tuning of borohydrides may create more possibilities that could have an impact on new areas of battery chemistry. It is of high scientific interest to investigate the origins of the high ionic conductivities of borohydrides and their correlated advanced structures, which may empower the rational structural design of borohydride SSEs.

Here, we review investigations of simple borohydrides, polyhedral borohydrides, their derivatives with ionic-conductive properties, effective strategies toward engineering this emerging SSE system with enhanced ionic conductivity, and research work regarding the ionic-conduction mechanisms and thermodynamics/kinetics behind the highly conductive structures. Furthermore, we conclude with a discussion of 1) the advantages and challenges correlated with the application of borohydride SSEs for ASSBs; 2) the reasons for the main bottlenecks relating to cell integration, the chemical and electrochemical decomposition or stability of borohydride SSEs, and borohydride SSE/electrode composites; and 3) more reliable approaches to select compatible components to promote better performance of borohydride-based ASSBs. New avenues to explore borohydrides SSE are considered, which will facilitate their application in next-generation batteries.

2. Progress of Borohydride-Based Solid-State Electrolytes and Approaches for Increasing the Conductivity

In this section, the structural-tuning approaches to improve the ionic conductivity of borohydrides are presented by employing $LiBH_4$ as an example. The structures of Na^+, K^+, Mg^{2+}, or Al^{3+} salts with BH_4^-/polyhedral borohydride anions may also be tailored by these strategies to favor fast ionic mobility. The ionic-conduction mechanisms and thermodynamics/kinetics correlated with ionic conductivity behind these strategies have also been probed to streamline the development of the key structures/properties that dominate the ionic conductivity.

### 2.1. Strategies to Enhance Ion Conduction for $LiBH_4$/$NaBH_4$ SSEs

2.1.1. Strategies to Improve Li^+ Mobility for $LiBH_4$ SSEs

$LiBH_4$ as the first discovered ionic-conductive borohydride was reported by Matsuo et al. in 2007.[23a] The ionic conductivity of $LiBH_4$ increases by 4–5 orders of magnitude from 10^{-7} S cm^{-1} at room temperature to 10^{-2} S cm^{-1} (443 K), accompanied by a phase transition from orthorhombic Pnma to hexagonal P63/mmc phase above 390 K, as described in **Figure 2**a. Furthermore, no polarization has been detected at the

$LiBH_4$–lithium-metal interface, even when tested under a high current density of 40 mA cm^{-2}, which confirms the stability of the lithium-metal–$LiBH_4$ interface and the high electrochemical reaction rates using $LiBH_4$ SSEs.[22,23b,25] Possible mechanisms for the superionic conductivity of hexagonal $LiBH_4$ have been probed. The combined results from experimental and theoretical investigations on frequency-dependent nuclear magnetic resonance (NMR) spectroscopy, spin–lattice relaxation (SLR), and ab initio nonequilibrium molecular dynamics (AIMD) have suggested that 2D Li^+ conduction may take place in the hexagonal plane (Figure 2b), and a double splitting of the Li^+ lattice sites may play an important role in the high ionic conductivity of hexagonal $LiBH_4$.[23a,26,27] Ikeshoji et al.[28] discovered through first-principles molecular dynamics simulations that interstitial sites occupied by Li^+ in a metastable state may also contribute to the superionic conductivity of hexagonal $LiBH_4$.

Given the excellent ionic conductivity of hexagonal $LiBH_4$, improving the ionic conductivity of orthorhombic $LiBH_4$ or synthesis of RT-stabilized hexagonal $LiBH_4$ through structural tuning is highly desirable, which is the key step toward bringing borohydride solid-state electrolytes into practical application in solid-state batteries.[12d] The effective modification strategies involve second-phase incorporation, aliovalent ion doping, interface engineering, etc.

Second-Phase Incorporation: Maekawa et al. developed the first RT-stabilized hexagonal $LiBH_4$ composites by the incorporation of lithium halide LiX (X = Cl, Br, and I).[23b] The addition of lithium halide assisted in lowering the activation energies, as well as reducing the phase-transition temperature of all composites to below 353 K, even with the smallest LiI dopant amount of 12.5%. The phase-transition temperatures reduced significantly with the expanded anionic radius of the dopant, and the highest ionic conductivity was achieved by 3$LiBH_4$–LiI composite. The X-ray diffraction (XRD) patterns of 3$LiBH_4$–LiI proved that only hexagonal $LiBH_4$ existed. The highly polarized I^- ions embedded in the anionic frameworks may contribute to the reconstruction of wider Li^+ diffusion channels, which result in reduced electrostatic interactions between the Li^+ and the anionic skeleton, thus facilitating faster Li^+ mobility than that from doping with F^- or Cl^-. Vegge and co-workers studied the $LiBH_4$–LiI system in detail through both experimental and computational methods.[26,29] $LiBH_4$–LiI solid solutions with varied content (6.25–50%) of LiI were obtained by annealing the ball-milled composites at 413 K, and the obtained $LiBH_4$–xLiI composites presented linearly reduced phase-transition temperature with the increasing content of LiI (Figure 2c). The XRD patterns confirmed that only hexagonal $LiBH_4$ existed at dopant ratios higher than 12.5%, and the optimum ionic conductivity was obtained near the $Li(BH_4)_{0.8}I_{0.2}$ composite.[29] The ^7Li NMR lineshape of 25% LiI-doped $LiBH_4$ at 298 K resembled that of hexagonal $LiBH_4$ (Figure 2d,e), and did not change from 423 K to room temperature, demonstrating that the superionic phase was stabilized at room temperature. The combined results of density functional theory (DFT) calculations and quasielastic neutron scattering (QENS) indicated that an abundance of lithium defects was created, and a high concentration ($\approx 5 \times 10^{18}$ cm^{-3}) of Frenkel pairs (formation energy of 0.44 eV) could mainly contribute to the improved ionic conductivity in

**ADVANCED
SCIENCE NEWS**

www.advancedsciencenews.com

**ADVANCED
MATERIALS**

www.advmat.de
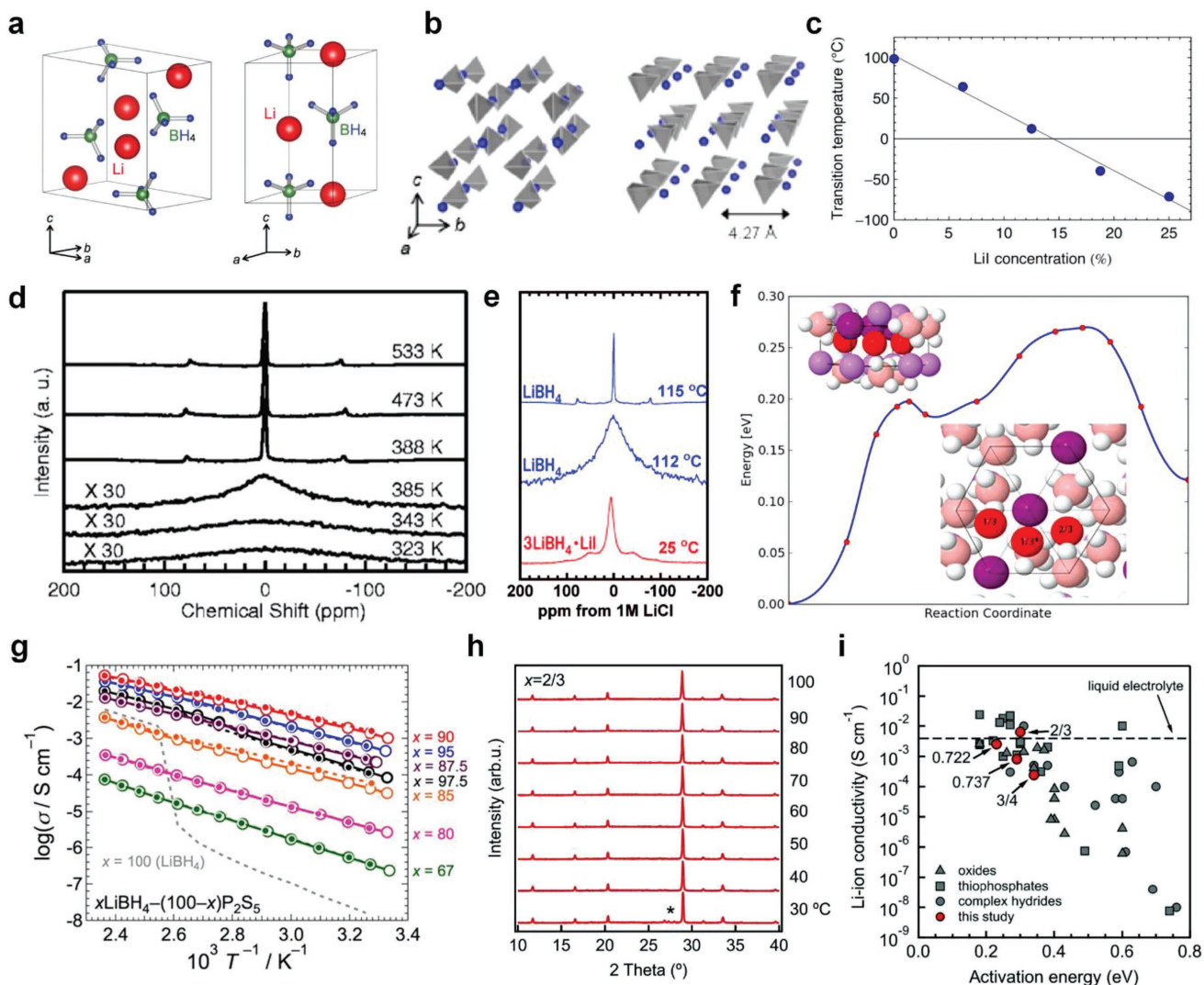
Figure 2. a) Crystal structures of $LiBH_4$: left) orthorhombic low temperature phase and right) hexagonal high-temperature phase.[22] b) Different Li arrangements for $LiBH_4$: left) in the LT phase and right) in the HT phase; gray tetrahedra: BH_4 groups; blue balls: Li. c) LiI concentration dependence of phase-transition temperatures for the $(1 − x)LiBH_4+xLiI$ composite.[29] d,e) Comparison of ^7Li NMR spectra at several chosen temperatures for d) pure $LiBH_4$ and e) $3LiBH_4·LiI$ composite. f) Li^+ migration path with the lowest energy cost in the $Li(BH_4)_{0.75}I_{0.25}$ composite from a 1/3 to a 2/3 interstitial site, passing through a 1/3* interstitial site, with Li, I, B, and H atoms represented by pale purple, dark purple, pink, and white, respectively. g) Temperature dependence of ionic conductivities for $xLiBH_4−(100 − x)P_2S_5$ ($x = 100$, 97.5, 95, 90, 87.5, 85, 80, and 67). h) XRD patterns at selected temperatures for $Li(BH_4)_{1−x}(NH_2)_x$ when $x = 2/3$. i) Li^+ conductivities versus activation energy for $Li(BH_4)_{1−x}(NH_2)_x$ with different components at 40 °C (red dots), with the numbers beside the arrows denoting the composition x and the dashed line depicting the estimated Li-ion conductivity of the liquid electrolyte 1 M $LiPF_6$ in ethylene carbonate:ethyl methyl carbonate (EC:EMC) 1:1 (v:v). a) Reproduced with permission.[22] Copyright 2014, Wiley-VCH. b,d) Reproduced with permission.[23a] Copyright 2007, AIP Publishing. c) Reproduced with permission.[29] Copyright 2013, American Chemical Society. e) Reproduced with permission.[23b] Copyright 2009, American Chemical Society. f) Reproduced with permission.[26b] Copyright 2013, American Chemical Society. g) Reproduced with permission.[38] Copyright 2015, Royal Society of Chemistry. h,i) Reproduced with permission.[31] Copyright 2017, Wiley-VCH.

the solid solution. The low energy barriers (0.2–0.3 eV) between the stable defect sites allow high defect mobility in $Li(BH_4)_{0.75}I_{0.25}$ composites (Figure 2f).[26b] Matsuo et al. developed the $Li_2(BH_4)(NH_2)$ and $Li_4(BH_4)(NH_2)_3$ systems, which are Li-ion conducting SSEs synthesized by mechanically milling different stoichiometric ratios of $LiBH_4$ with $LiNH_2$.[30] The $Li_2(BH_4)(NH_2)$ and $Li_4(BH_4)(NH_2)_3$ compounds presented high RT ionic conductivities of $2 × 10^{-4}$ and $8 × 10^{-4}$ S cm^{-1}, respectively, which are 4–5 orders of magnitude higher than for both

parent hydrides. When heated above 370 K, the ionic conductivity of $Li_4(BH_4)(NH_2)_3$ was increased to $1 × 10^{-3}$ S cm^{-1}, and, more impressively, $Li_2(BH_4)(NH_2)$ could reach up to $6 × 10^{-2}$ S cm^{-1} above the transition temperature. Slim-shaped ^7Li NMR spectra were seen for both $Li_2(BH_4)(NH_2)$ and $Li_4(BH_4)(NH_2)_3$, even around RT, which verified the presence of highly mobile Li^+ species in the complex hydrides at RT. Meanwhile, contributions from a broad Gaussian component and a narrow Lorentzian component were observed in the RT ^7Li

NMR spectrum of the $Li_2(BH_4)(NH_2)$ compound, suggesting the coexistence of low-mobility Li^+ species and high-mobility Li^+ species. Both $Li_2(BH_4)(NH_2)$ and $Li_4(BH_4)(NH_2)_3$ showed multiple Li^+ occupation sites in their crystal structures, and, as a suitable measurement for Li^+-diffusion bottlenecks, the size of each site was calculated by the definition of the largest radius of a sphere encircled by the adjacent hydrogen atoms of anions in every unit cell. $Li_2(BH_4)(NH_2)$ was found to possess two types of inequivalent lithium sites: 18 Li(1)s (calculated size of Li(1)s site: 0.16 nm) and 18 Li(2)s (0.09 nm) sites. $Li_4(BH_4)(NH_2)_3$ was also found to exhibit three types of unidentical lithium sites: 12 Li(1)s (0.17 nm), 12 Li(2)s (0.11 nm), and 8 Li(3)s (0.11 nm). In $Li_2(BH_4)(NH_2)$, 50% of the Li ions abnormally occupied the smaller low-mobility Li(2) site, which could rationally explain the larger activation energy and higher contribution of the Gaussian component to the observed RT ^7Li NMR spectrum of $Li_2(BH_4)(NH_2)$ rather than $Li_4(BH_4)(NH_2)_3$. The crystal structures of $Li_2(BH_4)(NH_2)$ (trigonal, $a = 1.4492(1)$, $c = 0.9236(1)$ nm) and $Li_4(BH_4)(NH_2)_3$ (cubic, $a = 1.0669(1)$ nm) were totally different from those of the parent $LiBH_4$ or $LiNH_2$. Owing to the synergistic effect of BH_4^- and NH_2^- anions, new Li^+ occupation sites were created that were tetrahedrally coordinated by a combination of BH_4^- and NH_2^- anions, resulting in an enhanced ionic conductivity at low temperature. Recently, Yan et al. developed a new solid solution of $Li(BH_4)_{1-x}(NH_2)_x$ ($x = 2/3$) by modulating the precursor ratio $LiBH_4$:$LiNH_2$ to 1:2, with a Li^+ conductivity of 6.4×10^{-3} S cm^{-1} at 313 K, which is 1 order of magnitude larger than that of $Li(BH_4)_{1-x}(NH_2)_x$ ($x = 1/2$) and $Li(BH_4)_{1-x}(NH_2)_x$ ($x = 3/4$) compounds.[31] $Li(BH_4)_{1-x}(NH_2)_x$ ($x = 2/3$) underwent a phase transition around 313 K, and this was consistent with the steepened slope of the Arrhenius plot in the same temperature range. In addition, the $Li(BH_4)_{1-x}(NH_2)_x$ ($x = 2/3$) compound presented a preserved cubic α phase with a slightly increased lattice parameter (10.670 Å) compared to the cubic $Li(BH_4)_{1-x}(NH_2)_x$ ($x = 3/4$) (10.655 Å) reported in the literature.[30] A small peak at $2\theta \approx 25°$–30° (marked by a star) was observed in the $x = 2/3$ phase (Figure 2h), which could be ascribed to a previously reported metastable γ phase within the amide–borohydride phase diagram.[31,32] These peaks were absent in the patterns of the $x = 3/4$ phase. Li^+ conductivities and activation energies for $Li(BH_4)_{1-x}(NH_2)_x$ with different components at 313 K are summarized in Figure 2i, demonstrating the optimum ionic-conductive behavior of $Li(BH_4)_{1-x}(NH_2)_x$ in the $x = 2/3$ phase. The energy barriers for lithium conduction in the cubic α phase were examined by DFT, using the climbing-image nudged-elastic-band method. The investigated lithium-hopping process includes: i) Li^+ hopping from the filled sublattice into the empty sublattice, and ii) Li^+ shuttling between empty sublattices. The calculated energy barrier for the former Li^+-hopping events surpasses 1 eV, demanding high energy to occupy the empty sublattice, which may be realized in the presence of rich structural defects and small grain size. In contrast, the latter hopping case within the empty sublattice possessed lower energy barriers of 0.3–0.4 eV, a value that well conforms to the obtained activation energy from the Arrhenius plot. It was reported that the body-centered-cubic (bcc) lattices of sulfide-based SSEs could enable energetically less expensive Li^+ hopping, which is realized through migration between face-sharing tetrahedral sites. Such face-sharing tetrahedral sites are absent in the face-centered-cubic (fcc) lattices, however. In the fcc lattices with only edge- and corner-sharing tetrahedral sites, Li ions are found to migrate along the intermediate octahedral sites.[33] After mapping the cubic α phase of lithium amide–borohydrides to a distorted fcc lattice, to accommodate the fast reorientation of highly polarized NH_2^- groups, a different, yet less-energy-demanding, migration within two edge-sharing tetrahedral sites is adopted, which enables improved lithium-ion hopping and high ionic conductivity of the lithium amide–borohydride compound.[31] The sulfides generally exhibit faster Li^+-ion diffusion.[34] A simple substitution for O in $Li_{3+x}(P_{1-x}Si_x)O_4$ by S could give rise to 3 orders of magnitude higher ionic conductivity in $Li_{3+x}(P_{1-x}Si_x)S_4$ so that S emerges as a very useful element for the enhancement of total ionic conductivity.[14,17d,35] The favorable ionic-conductivity properties of sulfides might originate from the large anionic frameworks with high polarizability, which could enlarge the primary diffusion channels and mitigate the electrostatic restriction of Li^+ mobility, which is reminiscent of the similar role of LiI in $LiBH_4$.[34a] Liang and co-workers further evidenced the feasibility of sulfide incorporation to improve the ionic conductivity of other solid-state electrolytes.[36] The synthesized $Li_7La_3Zr_2O_{12}/\beta$-Li_3PS_4 SSE composites showed better ionic conductivity than either of the parent electrolytes. The addition of "soft" sulfide into the composites could also help to weaken the processability barriers of the "hard" oxide electrolytes, manifesting superior "whole greater than the sum of parts" effects. Therefore, fabricating novel thio–borohydride composites is a promising alternative, by which the achievement of novel properties and extended new chemistry in borohydride SSEs are anticipated.[12d,35] Tatsumisago and co-workers developed $(100 - x)(0.75Li_2S \cdot 0.25P_2S_5) \cdot x$ $LiBH_4$ glass electrolytes by mechanically milling mixtures of bulk $LiBH_4$ and $75Li_2S \cdot 25P_2S_5$.[37] The optimal RT ionic conductivity of 1.6×10^{-3} S cm^{-1} was reached by the $67(0.75Li_2S \cdot 0.25P_2S_5) \cdot 33LiBH_4$ composition. The incorporation of highly polarized sulfide enables the negative charges in BH_4^- ions to be delocalized, which leads to reduced electrostatic interactions and enhanced ionic conductivity of the glass electrolytes. Unemoto et al. developed a new sulfide–borohydride composite, $90LiBH_4$:$10P_2S_5$, which presented a high ionic conductivity of 10^{-3} S cm^{-1} at RT with the activation energy of 0.38 eV (Figure 2g).[38] QENS and elastic-scattering fixed-window scans (FWSs) of $90^7Li^{11}BH_4$:$10P_2S_5$ and $^7Li^{11}BH_4$ revealed the dynamics of the anionic units. The observed width of H jumps (2 Å) in $90^7Li^{11}BH_4$:$10P_2S_5$ agreed with the H–H distances in both $[BH_4]^-$ and $-BH_3$ entities, confirming the presence of two different quasielastic components from two hydrogenous bodies. The different widths were in proportion to the reorientational mobility, and the jump frequencies of the two hydrogenous entities were estimated to be on the order of 10^{11} s^{-1}. Although it is difficult to probe into the intrinsic nature of mobile species precisely, from the above evidence, the fast reorientational mobility of the anionic units, as an important variable altering the ionic conductivity of borohydrides, may contribute most to the fast ionic conductivity of $90LiBH_4$:$10P_2S_5$ composite.[25a,39]

From the above discussion, the introduction of a second phase with a large anionic radius and high polarizability could

**ADVANCED
SCIENCE NEWS**

www.advancedsciencenews.com

**ADVANCED
MATERIALS**

www.advmat.de
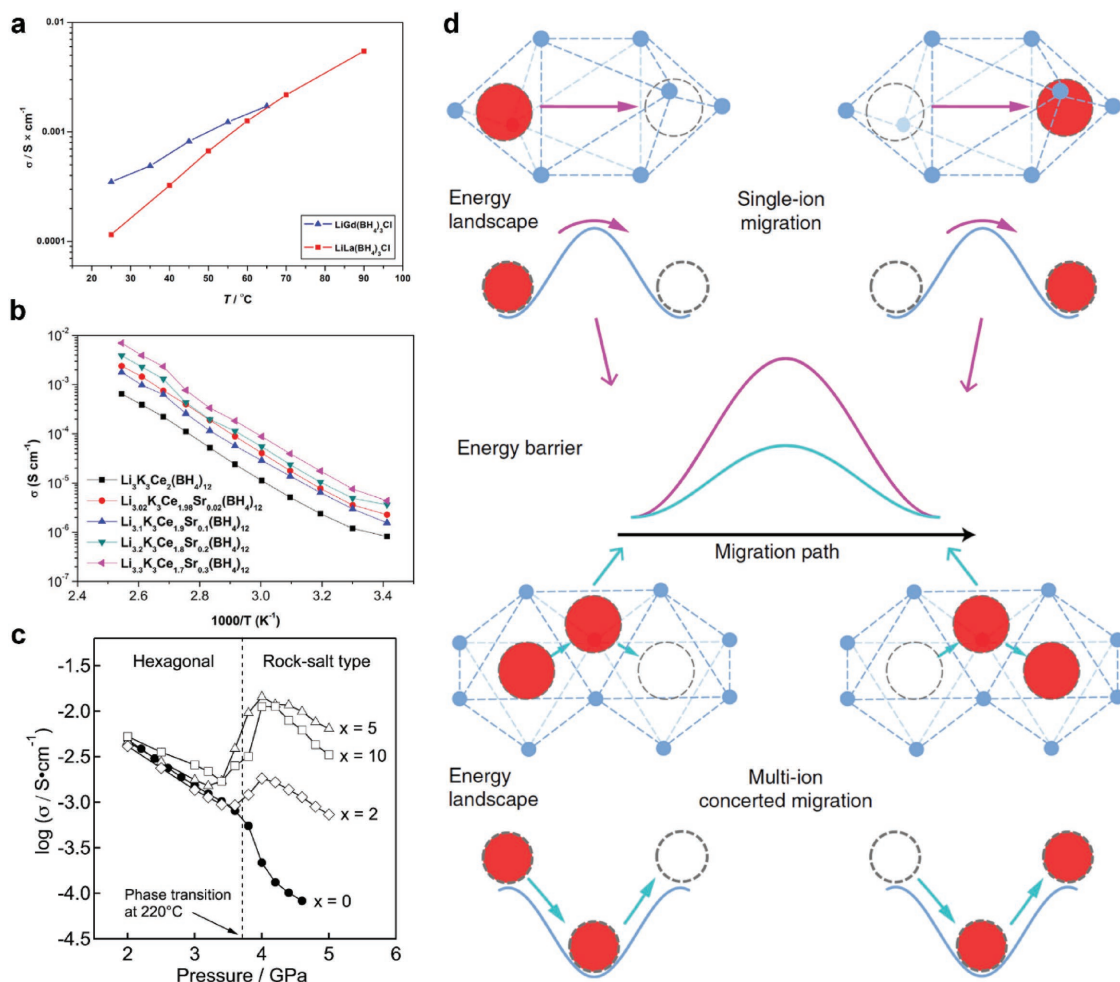
Figure 3. a) Temperature dependence of ionic conductivity for LaCl$_3$–LiBH$_4$ (1:3) and GdCl$_3$–LiBH$_4$ (1:3). b) Temperature dependence of ionic conductivity for Li$_3$K$_3$Ce$_2$(BH$_4$)$_{12}$ and Sr-doped Li$_3$K$_3$Ce$_2$(BH$_4$)$_{12}$. c) Pressure dependence of Li$^+$ conductivity for LiBH$_4$–x mol% Ca(BH$_4$)$_2$ (x = 0, 2, 5, and 10). d) Comparison of single-ion migration and the multi-ion concerted-migration process. a) Reproduced with permission.[40a] Copyright 2012, American Chemical Society. b) Reproduced with permission.[41] Copyright 2015 Elsevier B.V. c) Reproduced with permission.[42] Copyright 2016, American Chemical Society. d) Reproduced with permission.[47] Copyright 2017, Springer Nature.

bring marked changes to the environment of Li$^+$ in pristine LiBH$_4$, which would further facilitate fast Li$^+$ diffusion and contribute to enhancement of the ionic conductivity.

Aliovalent-Ion Doping: Jensen and co-workers developed bimetallic borohydride chlorides LiM(BH$_4$)$_3$Cl (M = La, Gd, Ce) (cubic, space group I-43) by ball-milling of LiBH$_4$ with MCl$_3$ (M = La, Gd, and Ce).[40] The ionic conductivities of LiLa(BH$_4$)$_3$Cl and LiGd(BH$_4$)$_3$Cl at 293 K were 2.3 × 10^{-4} and 3.5 × 10^{-4} S cm^{-1} (**Figure 3**a), respectively, while that of LiCe(BH$_4$)$_3$Cl is around 7 × 10^{-5} S cm^{-1}. In the crystal structures of LiM(BH$_4$)$_3$Cl (M = La, Gd, and Ce) compounds, three chloride atoms and three borohydride groups are coordinated to every lanthanide atom in the octahedral coordination environment. LiCe(BH$_4$)$_3$Cl (cubic, $I\bar{4}3m$, a = 11.7204(2) Å) compounds comprise Li$^+$ cations and tetranuclear anionic clusters of [Ce$_4$Cl$_4$(BH$_4$)$_{12}$]$^{4-}$, with Ce–Cl and Ce–B distances of 2.961(6) and 2.74(2) Å. The combined results from Rietveld refinement of synchrotron-radiation powder X-ray diffraction (SR-PXD) data, powder neutron diffraction (PND) data, and DFT optimization demonstrate

that, for the structure of LiCe(BH$_4$)$_3$Cl, the Li occupied the 12d Wyckoff sites, showing the lowest energy barrier in LiCe(BH$_4$)$_3$Cl. For cubic LiM(BH$_4$)$_3$Cl (M = La, Gd) compounds with corresponding unit-cell parameters a = 11.7955(1) and a = 11.5627(1) Å, the Li$^+$ positions resemble those of LiCe(BH$_4$)$_3$Cl. The ionic-conductivity values are fairly high, considering a high amount of nonconductive LiCl in the composites (mole ratio of LiM(BH$_4$)$_3$Cl to LiCl = 1:2). Taking mixed LiCe(BH$_4$)$_3$Cl as an example, due to the synthesis limitations to obtaining pure LiCe(BH$_4$)$_3$Cl, the mixture contains 49 wt% LiCe(BH$_4$)$_3$Cl, 17 wt% LiCl, and 34 wt% CeCl$_3$.[40b] There is promise of obtaining more conductive pure LiM(BH$_4$)$_3$Cl or LiM(BH$_4$)$_3$I compound after removing excess byproduct in the future. Brighi et al. reported a novel garnet-type metal borohydride, Li$_3$K$_3$Ce$_2$(BH$_4$)$_{12}$, with RT ionic conductivity of 3 × 10^{-7} S cm^{-1}. The influence of cation substitution on the lattice parameters and the ionic conductivity of Li$_3$K$_3$Ce$_2$(BH$_4$)$_{12}$ was studied by investigating a range of metal ions (Na$^+$, K$^+$, Rb$^+$, Ca^{2+}, Sr^{2+}, and Eu^{2+}). The experimentally observed unit-cell evolution

(normalized to the undoped sample $Li_3K_3Ce_2(BH_4)_{12}$) demonstrated that, apart from Ca^{2+}, the doping of other metal ions, such as Na^+, K^+, Rb^+, Sr^{2+}, and Eu^{2+}, could induce cell expansion if the metal ions entered the octahedral Ce-sites. In contrast, with the exception of Rb^+, the substitution of other metal ions caused cell contraction of the composite if the metal ions entered the square antiprismatic K-sites. The substitution on Ce-sites by divalent Sr^{2+} ion doping could efficiently "switch on" high Li^+ mobility in $Li_3K_3Ce_2(BH_4)_{12}$, with enhancement up to 1 order of magnitude in the temperature range from 294 to 416 K (Figure 3b).[41] Takamura and co-workers developed a Ca-substituted rock-salt-type (RST) $LiBH_4$ (Ca–RST-$LiBH_4$) SSE with fast ionic conductivity (Figure 3c).[42] Generally, the ionic conductivity of RST-$LiBH_4$ falls between those of the hexagonal and orthorhombic phases of $LiBH_4$ and is about 1 order of magnitude lower than for the hexagonal phase due to the limited carrier concentration.[43] The ionic conductivities of Ca–RST-$LiBH_4$ and Ca–hexagonal $LiBH_4$ were tested under pressures varying from 1.5 to 6 GPa at a constant temperature of 493 K, using a cubic anvil-type apparatus, and they were further confirmed as pure Li^+ conductors. In comparison with pure hexagonal $LiBH_4$, the observed ionic conductivity of Ca–hexagonal $LiBH_4$ dropped with elevated pressures. As previously discussed, Frenkel-type defects could contribute to Li^+ diffusion in $LiBH_4$ on the basis of the interstitial mechanism.[42] The causes for the fading ionic conductivity of Ca–hexagonal $LiBH_4$ may originate from: i) enough carriers preexisting in the pure hexagonal $LiBH_4$ so that further doping of Ca does not play a conspicuous role in promoting the ionic conductivity of hexagonal $LiBH_4$;[51] ii) the limited solubility of $Ca(BH_4)_2$ in hexagonal $LiBH_4$ phases also weakening the effectiveness in enhancing the mobility of Li ions;[44] and iii) Li^+-diffusion channels in hexagonal $LiBH_4$ contracting under high pressure. In contrast, in RST-$LiBH_4$, the incorporation of 5% Ca could enhance the ionic conductivity from 2.2×10^{-4} to 1.4×10^{-2} S cm^{-1} under 4.0 GPa at 493 K. In Ca–RST-$LiBH_4$, lithium vacancies formed by the Schottky-type defects may mainly contribute to the high mobility of Li^+, which has often been observed in rock-salt-type structures.[45] Therefore, the increased concentration of carriers in Ca–RST-$LiBH_4$ empowered the high ionic conductivity in this compound, and the highest ionic conductivity was reached at the doping ratio of 5% Ca.

In the classical diffusion model, ion transport is generally considered as the hopping of individual ions from one lattice site to another, migrating along the interconnected diffusion channels.[46] The ionic conductivity σ is proportional to $n_c \exp(-E_a/k_B T)$, where n_c is the concentration of mobile ion carriers (e.g., defects and interstitials), E_a is the activation energy at a given temperature T, and k_B is Boltzmann's constant. A high concentration of mobile ion carriers and a low activation energy barrier are highly desirable for achieving high ionic conductivity.[47] To give a more clear analysis of the reduced diffusion activation energy and fast ion conduction that occurs within multiple ions, Mo and co-workers proposed a novel multi-ion concerted-migration process (Figure 3d) based on AIMD simulations over a range of materials.[47] The ion configurations and Coulomb interactions among multiple ions, which were often ignored in classical diffusion models, have been recognized as being valuable for unveiling the mechanisms of

multi-ion concerted migration.[47] In the process of multiple-ion concerted migration, high-energy ions would show downhill diffusion and offset part of the energy needed for residual uphill-climbing ions,[47] which is in good agreement with experimental results. Multi-ion concerted migration is extrapolated to be universally applicable to superionic conductors, including, but not limited to, mobile ions of Li^+, Na^+, and Ag^+.[47] Apart from this, the author further proposed a simplified strategy for designing superionic-conductive composites, which involved the insertion of mobile ions into high-energy sites to "switch on" the concerted ion migration. This strategy could provide some elucidation of the effectiveness of aliovalent ion doping in borohydrides and ignite research interest in designing superior borohydride SSEs with low cation hopping barriers.

Interface Engineering Strategy ("Filler Effect"): de Jongh and co-workers studied the ionic conductivity of nanoconfined $LiBH_4$ in ordered mesoporous silica MCM-41 scaffolds (4 nm pores).[48] MCM41–$LiBH_4$-91 delivered an impressive ionic conductivity of 0.1 mS cm^{-1} at 313 K, which is 1000 times higher than for bulk $LiBH_4$ at the same temperature.[49] In comparison with the activation energies of orthorhombic and hexagonal $LiBH_4$ (0.69 and 0.53 eV), that of the MCM41–$LiBH_4$-91 composite was reduced to 0.43 eV, illustrating the smaller impact of temperature fluctuations on the ionic conductivity of MCM41–$LiBH_4$-91. Static solid-state ^7Li NMR (with ^1H decoupling) revealed an abnormally high ionic mobility in the MCM41–$LiBH_4$-91 nanocomposite. Two types of Li^+ migration were identified in the RT NMR spectra of MCM41–$LiBH_4$-91: i) the broad lines suggested the presence of a slow Li^+ mobility, which might originate from nano-$LiBH_4$ in the central pores of mesoporous MCM-41; and ii) the narrow line suggested the existence of faster Li^+ mobility, which might come from the nano-$LiBH_4$ grown on the walls of MCM-41. The rough calculations of the spectral areas of the two components suggest that the ratio of Li^+ with high mobility to low mobility is 3:7. As the temperature increased, this ratio rose continuously. The narrow-shaped ^7Li NMR (RT) spectrum of MCM41–$LiBH_4$-91 resembled that of highly conductive hexagonal $LiBH_4$. The fast Li^+ mobility in MCM41–$LiBH_4$-91 may be mainly attributed to the interface interactions between nano-$LiBH_4$ and SiO_2, which was further proved by Choi et al.[49] They compared the ionic conductivities of the melt-infiltrated porous-$LiBH_4$–MCM41 (MI-LM) and ball-milled-$LiBH_4$–fumed-SiO_2 (BM-LF) (**Figure 4**a),[49] and the ionic conductivity of the BM-LF sample rivals that of MI-LM, reaching 10^{-4} S cm^{-1}. Note that two conspicuous differences exist between the MI-LM and BM-LF composites: i) the Brunauer–Emmett–Teller (BET) surface area for porous MCM-41 (946 m^2 g^{-1}) is about threefold that for nonporous fumed silica (362 m^2 g^{-1}); and ii) $LiBH_4$ is nanoconfined in pure porous MCM-41, but not in fumed silica. It can be clearly understood that the similar ionic conductivity comes from the strong and identical $LiBH_4$–SiO_2 interactions in both two composites. This research helps to distinguish what really works to accelerate the ion mobility of orthorhombic $LiBH_4$. From the above discussion, the interface engineering via a surface mechanism shows a powerful influence on the ionic conductivity of borohydrides.

So far, there is no detailed summary on the influence of interface engineering on ionic-conductive borohydrides. The following systematic study can follow the research route for
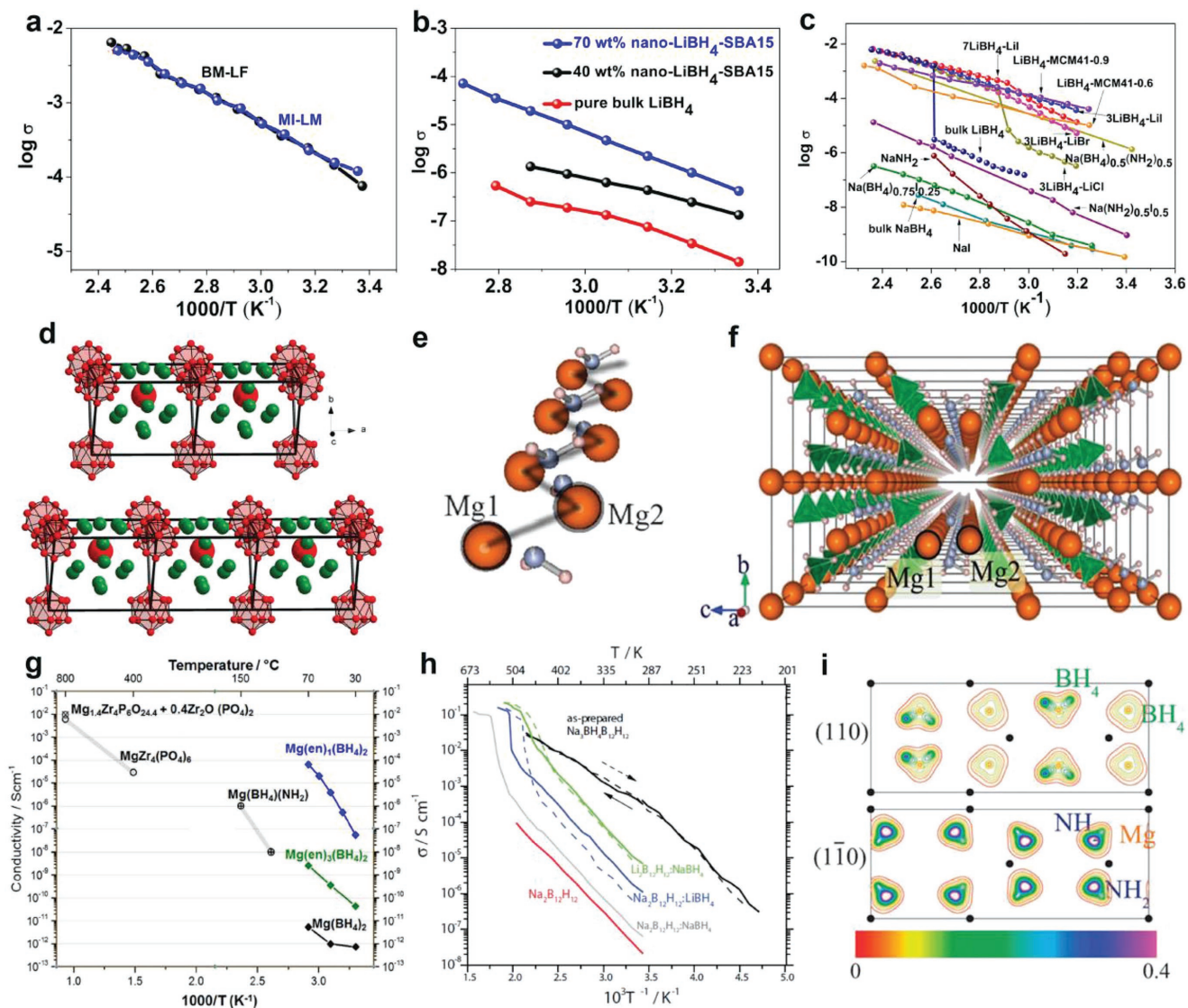
Figure 4. a) Temperature dependence of ionic conductivity for various modified LiBH$_4$ materials, which include melt-infiltration LiBH$_4$-MCM41 (MI-LM) and ball-milled LiBH$_4$-fumed SiO$_2$ (BM-LF).[48,49] b) Temperature dependence of ionic conductivity for 70 wt% nano-LiBH$_4$–30 wt% SiO$_2$, 40 wt% nano-LiBH$_4$–60 wt% SiO$_2$, and bulk LiBH$_4$ measured using a Au blocking electrode. c) Reported ionic conductivity of various modified LiBH$_4$ material as a function of temperature, which include 3LiBH$_4$–LiI,[23b] 7LiBH$_4$–LiI,[23b] LiBH$_4$–MCM41-0.91,[48] 3LiBH$_4$–LiBr,[23b] LiBH$_4$–MCM41-0.6,[48] Na(BH$_4$)$_{0.5}$(NH$_2$)$_{0.5}$,[57] 3LiBH$_4$–LiCl,[23b] bulk LiBH$_4$,[23b] Na(NH$_2$)$_{0.5}$I$_{0.5}$,[19c] NaNH$_2$,[57] Na(BH$_4$)$_{0.75}$I$_{0.25}$,[19c] bulk NaBH$_4$,[57] and NaI.[19c] d) Crystalline structure of Na$_3$BH$_4$B$_{12}$H$_{12}$ in *Cmc*2$_1$, obtained from refined data at 523 K. Small red balls: B atoms on B$_{12}$H$_{12}$ groups; big red balls: BH$_4$ groups; green balls: cations. e) The Mg zigzag arrangement of Mg(BH$_4$)(NH$_2$). f) Schematic illustration of the crystal structure of Mg(BH$_4$)(NH$_2$). g) Temperature dependence of ionic conductivity for Mg ionic conductors. h) Temperature dependence of ionic conductivity for Na$_3$BH$_4$B$_{12}$H$_{12}$ and related composites. i) Contour plots of valence charge for Mg(BH$_4$)(NH$_2$). The black dots represent Mg atoms positioned on the planes. d,h) Reproduced with permission.[58] Copyright 2015, Wiley-VCH. e,f,i) Reproduced with permission.[61] Copyright 2013, Royal Society of Chemistry. g) Reproduced with permission.[60] Copyright 2017, Springer Nature.

other solid-state electrolytes since the concept of interface engineering is exactly the same in borohydrides along with the "filler effect." Besides SiO$_2$, fillers such as TiO$_2$, Al$_2$O$_3$, CeO$_2$, ZrO$_2$, MgO, Li$_6$ZnNb$_4$O$_{14}$, metal-organic frameworks (MOFs), etc., have also been explored for the optimization of SSEs.[50–52] Polu et al. compared the filler effects on the RT ionic conductivity of 85PEG–15Mg(NO$_3$)$_2$, where PEG is poly(ethylene glycol). TiO$_2$ and CeO$_2$ fillers with different doping levels of 0, 5, 10, 15, and 20 wt% were added to 85PEG–15Mg(NO$_3$)$_2$. It was found that, at most, the addition of 10% TiO$_2$ could

raise the RT ionic conductivity of 85PEG–15Mg(NO$_3$)$_2$ to 10^{-4} S cm^{-1}.[50a] Liang and co-workers compared the effects of ion-conducting fillers (Li$_6$ZnNb$_4$O$_{14}$ (LZNO)) and nonconducting fillers (Al$_2$O$_3$, SiO$_2$) on Li$^+$ mobility in β-Li$_3$PS$_4$ (LPS) solid-state electrolyte.[52] For the 10:90 (LZNO:LPS) composite, the ionic conductivity reached 2.44 × 10^{-4} S cm^{-1} and was the highest among the three LPS–filler composites, indicating the unique interface effect between the LZNO and LPS. The 10:90 (LZNO:LPS) composite showed excellent electrochemical stability, and no side reactions were observed at the interface, even

after 100 cycles. Apart from that, nanofillers such as molecular sieves (SBA15, ZSM-5), MOFs with porous hierarchical microstructures, and high surface areas also offer alternative opportunities. Yuan et al. proved the feasibility of MOF fillers for the poly(ethylene oxide)–LiN(SO$_2$CF$_3$)$_2$ (PEO–LiTFSI) polymer electrolyte.[53] With the addition of 10 wt% Zn-MOF-5, the highest ionic conductivity of 3.16×10^{-5} S cm^{-1} was reached, which was fourfold higher than that of pristine PEO–LiTFSI composite (PEO:LiTFSI weight ratio = 10:1). Gerbaldi et al. prepared Al-MOF nanofillers to further modify the ionic conductivity of PEO–LiTFSI composites.[51] With the addition of 10 wt% Al-MOFs, the RT ionic conductivity of PEO–LiTFSI–Al-MOF jumped ≈2 orders of magnitude higher than that of pristine PEO–LiTFSI.[51] It was suggested that the Lewis-acidic sites of Zn-MOF-5 and Al-MOF bonding with the PEO chains and lithium-salt anions may help to reduce the crystallization of PEO and conFigure new Li$^+$ diffusion passages, finally leading to improved Li$^+$ mobility.

Diverse interface engineering is anticipated to be beneficial to the fast ion conduction of borohydrides. Apart from filler types, the filler concentration should be near the optimum value for convenient comparison. As commonly observed, the ionic conductivity shows a nonlinear correlation with the filler concentration.[51] The moderate filler concentration required to achieve maximum ionic conductivity may be 5% and up based on different filler properties.[54] The upper limit of the filler concentration is determined by the dilution effect, which tends to depress the ionic conductivity. At low filler concentrations, the detrimental dilution effect is suppressed owing to the strong interfacial interactions between Li$^+$ and the filler, which positively enhances the ionic conductivity.[51] When the filler concentration is too high, the dominant dilution effect will compromise the beneficial effect of filler incorporation and has an adverse effect on the ionic conductivity.[51] The ionic conductivity of borohydrides could be further optimized through proper selection of fillers with hierarchical ordered nanostructures.

Inspired by this, we utilized a solvothermal method to anchor nano-LiBH$_4$ homogeneously onto the pore walls of mesoporous SiO$_2$ (SBA15, MCM-41, FDU-12, etc.) and the reaction was carried out through a solid–gas reaction between nano-LiH–meso-SiO$_2$ (nano-LiH formed by decomposition of *tert*-butyllithium under 5 MPa H$_2$ pressure) and B$_2$H$_6$ gas. By adjusting the amounts of reactants, different loading ratios of nano-LiBH$_4$ in mesoporous SiO$_2$ were obtained. The soft textures of nano-LiBH$_4$–meso-SiO$_2$ composites resembled that of the meso-SiO$_2$ molecular sieve. It is expected that, through solvothermal synthesis, nano-LiBH$_4$–meso-SiO$_2$ should exhibit higher intrinsic ionic conductivity due to the more uniform dispersion of LiBH$_4$ in mesoporous SiO$_2$ and the fully utilized interface areas between LiBH$_4$ and SiO$_2$. The measured ionic conductivity of 70 wt% nano-LiBH$_4$–30 wt% SBA15 was 10^{-6} S cm^{-1} at 298 K, however, just 2 orders of magnitude higher than that of pure LiBH$_4$ crystal (Figure 4b). Two problematic issues may be responsible for this failure: i) the organic solvent used in the synthesis process could not be thoroughly removed due to experimental limitations since LiH was easily oxidized during removal of the solvent at high temperature and the presence of excess solvent molecules would block the diffusive channels for Li$^+$. ii) When the ionic conductivity is tested from 353 to 413 K,

excess solvent in the composites will evaporate, resulting in cracked electrolyte pellets and degraded testing results. Thus, the measured value of ionic conductivity was much lower than their intrinsic ionic conductivities. Only when these problematic issues are substantially addressed, we can obtain viable LiBH$_4$ superionic-conductive electrolytes, with nano-LiBH$_4$ well dispersed and anchored on the walls of molecular-sieve-like nanofillers. It is worth noting that the soft textures of molecular sieves with high BET surface areas usually deliver poor powder fluidity, generating uneven frictions between inner powder particles or at the interfaces connecting the powder and the mold walls, which often result in chipped pellets during the pressing process. Several molding techniques have been recently developed, including common dry pressing, isostatic pressing, slip-casting, and two-stage pressing. The different nature of nanopowders requires different shaping techniques.[55] The two-stage pressing method appeared to be very useful for processing materials with poor powder fluidity: to improve the liquidity of soft textural powders, at the initial stage, powder granulation is conducted, after that, it becomes much easier to obtain a complete solid electrolyte pellet in the second-stage pressing.

From the above discussion, strategies based on second-phase incorporation, aliovalent ion doping, and interface engineering act toward achieving high ionic conductivity in LiBH$_4$ (Figure 4c). The above strategies could significantly guide the designs of novel high-ionic-conductivity borohydride SSEs, including, but not limited to, NaBH$_4$ and Mg(BH$_4$)$_2$.

2.1.2. Improving the Ionic Conductivity of NaBH$_4$/Mg(BH$_4$)$_2$ SSEs

To mitigate current concerns about a possible lithium shortage, alternative energy-storage systems have also been studied to complement the existing Li-ion technology.[56] Sodium and magnesium solid-state batteries have emerged as promising alternative candidates, which has promoted research on Na and Mg fast ionic conductors. The dual-ligand compound Na$_2$(BH$_4$)(NH$_2$) with an antiperovskite-type structure (*Pm-3m* space group) was found to deliver an RT ionic conductivity of 3×10^{-6} S cm^{-1}, which was 4 orders of magnitude higher than that of NaBH$_4$.[57] The favorable ABX$_3$ structure of (BH$_4$)(NH$_2$)Na$_2$, with BH$_4^-$, NH$_2^-$, and Na$^+$ occupying the A, B, and X sites, respectively, could offer plenty of vacancies (approximately one-third unoccupied X sites) to facilitate fast sodium-ion migration.[57] The Na$^+$ conductivity can be further improved by structural tuning. Sadikin et al. prepared a Na$_3$BH$_4$B$_{12}$H$_{12}$ composite via a solid-phase reaction.[58] Na$_3$BH$_4$B$_{12}$H$_{12}$ is in the space group *Cmc*2$_1$ with lattice parameters of $a = 8.0083(4)$, $b = 21.881(1)$, $c = 7.7672(4)$ Å, and $V = 1361.05(12)$ Å^3 at 523 K. The mobile Na ions in Na$_3$BH$_4$B$_{12}$H$_{12}$ are found in the Na-rich layers, which contain BH$_4^-$ anions and are perpendicular to the *b*-axis (Figure 4d). Furthermore, a larger synchronous thermal expansion of the *a*- and *c*-axes is observed at a certain temperature. This demonstrates that Na$_3$BH$_4$B$_{12}$H$_{12}$ possesses a layered structure, in which Na-rich layers (containing BH$_4^-$ groups) alternate with Na-free layers (containing B$_{12}$H$_{12}^{2-}$ groups). Na$_3$BH$_4$B$_{12}$H$_{12}$ exhibited an RT Na$^+$ conductivity of 5×10^{-4} S cm^{-1} (Figure 4h), which is 2 orders of magnitude higher than that of Na$_2$BH$_4$NH$_2$. Na ions are supposed to migrate along the (0 1 0) planes (2D Na$^+$ migration

paths) of $Na_3BH_4B_{12}H_{12}$. The edge-sharing tetrahedra with an intrasheet edge length of 7.139 Å in the $B_{12}H_{12}^{2-}$ layers are reminiscent of Na^+ migration in $Na_2B_{12}H_{12}$, and the edge-length is close to that (7.013 Å) of low-temperature (LT) $Na_2B_{12}H_{12}$, which has been proved to be energetically expensive for Na^+ migration, and rationally interprets the high energy barrier of Na^+ migration across the closo $B_{12}H_{12}^{2-}$ layer. For $Na_3BH_4B_{12}H_{12}$, the calculated longest length of edges in mixed-anion layers reaches 8.008 Å, which is consistent with the length (8.098 Å) of tetrahedral edges of high-temperature (HT) $Na_2B_{12}H_{12}$, along which highly mobile Na ions hop among the interstitial sites. The activation energies of $Na_3BH_4B_{12}H_{12}$ fitted from the Arrhenius plots are 517 meV (218–273 K) and 340 meV (273–468 K), respectively, indicating the high mobility of Na^+ over the whole temperature range of 273–468 K.[58]

In the case of $Mg(BH_4)_2$, Mg atoms are coordinated by eight hydrogen atoms and confined in the firm tetrahedral cages constructed from BH_4 groups,[59] which gives rise to a strong Coulombic interaction and a low RT Mg^{2+} conductivity (10^{-12} S cm^{-1}).[60] Higashi et al. developed a dual-ligand $Mg(BH_4)(NH_2)$ SSE.[61] Compared with $Mg(BH_4)_2$, the $Mg(BH_4)(NH_2)$ compound with a Mg zigzag chain and tunneling structures (Figure 4e,f) exhibits a shorter distance between the adjacent Mg–Mg (3.59 Å) atoms than that of $Mg(BH_4)_2$ (4.32 Å). $Mg(BH_4)_2$ and $Mg(BH_4)(NH_2)$ present an ionic conductivity of $\approx 1 \times 10^{-9}$ and 1×10^{-6} S cm^{-1} at 423 K, respectively (Figure 4g).[57] It is suggested that, with the formation of Frenkel pairs in $Mg(BH_4)(NH_2)$, Mg atoms could migrate among the interstitial sites at a smaller energy cost, facilitating the Mg^{2+} mobility. The valence charge contour plots for $Mg(BH_4)(NH_2)$ (Figure 4i) show relatively lower localized charge density around Mg atoms than those of BH_4 and NH_2 ligands, implying the ionic-bonding character of $Mg(BH_4)(NH_2)$.[61] Apart from this, Roedern et al. reported the Mg^{2+} conduction in $Mg(en)_1(BH_4)_2$ and $Mg(en)_3(BH_4)_2$ complexes, with Mg^{2+} coordinated by extra neutral bidentate ethylenediamine ligand ($NH_2CH_2CH_2NH_2$, abbreviated as "en").[60] $Mg(en)_1(BH_4)_2$ showed higher ionic conductivity than both $Mg(en)_3(BH_4)_2$ and $Mg(BH_4)_2$. In the case of $Mg(en)_3(BH_4)_2$, with a large $[Mg(en)_3]^{2+}$ cation, Mg^{2+} is coordinated and confined by three chelating bidentate en ligands, whereas in $Mg(en)_1(BH_4)_2$, the number of coordinating en ligands is reduced from three to one, enabling Mg^{2+} to enter into an asymmetric mixed coordination environment (one en and two BH_4^-). The ionic conductivity of $Mg(en)_1(BH_4)_2$ is 5×10^{-8} S cm^{-1} at 303 K, which is several orders of magnitude higher than for both $Mg(BH_4)_2$ and $Mg(en)_3(BH_4)_2$, and this value reaches 6×10^{-5} S cm^{-1} at 343 K. Nevertheless, both sodium and magnesium ionic conductivity within BH_4^- groups needs to be further enhanced to an acceptable value to meet the requirements of practical application in the ASSBs.

2.2. Development of Superionic-Conductive Li/Na/Mg Polyhedral Borohydride SSEs

2.2.1. $Li_2B_nH_n/Na_2B_nH_n$ (n = 10, 12) SSEs

Metal polyhedral borohydrides ($M_{2/x}B_nH_n$, where x denotes the valence of the metal ion) have aroused increasing interest as promising energy-storage materials, specifically in the areas of hydrogen storage and superionic conductors. They are intermediate products after dehydrogenation of MBH_4, and the strong B−B bonds in the near-spherical frameworks hamper the reversible transition of $M_{2/x}B_nH_n$ to MBH_4, which impedes MBH_4 as a promising hydrogen-storage material.[62] Nevertheless, the high thermal stability of the $[B_nH_n]^{2/x-}$ skeletons favors their potential applicability as SSEs. Additionally, it was reported that metal polyhedral borohydrides will not rapidly react with water or release heat/hydrogen since they tend to form stable crystalline hydrates with water,[63] indicating that the "cage"-shaped polyhedral borohydrides can guarantee good thermal and chemical stability when used as SSEs.[64] The geometrical structures of polyhedral borohydride anions can be seen in **Figure 5**a–c.[25a] Taking the icosahedral $B_{12}H_{12}^{2-}$ as an example, the 30 sticks representing the icosahedral skeleton merely suggest the connectivity between cage atoms. 26 electrons from 12 BH vertices and an extra electron pair of negative charges are adopted. The typical (3c2e) bonds are delocalized among the icosahedra for cage bonding. The $B_{10}H_{10}^{2-}$ anions (lateral size: 4.9 Å; longitudinal size: 6.0 Å) are more elliptical than for $B_{12}H_{12}^{2-}$ (lateral size: 5.2 Å; longitudinal size: 5.8 Å) groups. Compared with BH_4^-, the $B_nH_n^{2-}$ anion is larger and possesses a weaker affinity to Li^+, which is more advantageous for facilitating fast cation mobility so that high ionic conductivity is anticipated.

In fact, $Li_2B_{12}H_{12}$ with large divalent $B_{12}H_{12}^{2-}$ anions possesses an ionic conductivity of 0.31 mS cm^{-1} (RT), which reaches as high as $10^{-2.6}$ S cm^{-1} at 393 K, showing an activation energy of 0.34 eV.[63a,65] Udovic et al. and Skripov et al. reported the superionic conductivity of $Na_2B_{12}H_{12}$,[39,66] which showed an impressive value of 0.1 S cm^{-1} around 529 K. Low-temperature $Na_2B_{12}H_{12}$ (LT-$Na_2B_{12}H_{12}$) was found to exist in an ordered monoclinic phase with fully occupied Na^+ cation sites. When the temperature was raised to near 529 K, the quasispherical $B_{12}H_{12}^{2-}$ anions underwent a body-centered-cubic transition, and the reorientational jump rate increased by ≈ 2 orders of magnitude. The phase-transition process is also accompanied by a reduced activation energy from 770 to 270 meV, with the formation of rich vacancies and off-center complex sublattices in various crossed orientations. In the bcc phase, the jumping rate of Na^+ was estimated to be 2×10^8 s^{-1} by ^{23}Na spin–lattice relaxation, and the anion reorientational jump rate reached 10^{11} s^{-1}, which was a 100-fold higher than that of LT-$Na_2B_{12}H_{12}$.[66] At high temperature, the rapidly spinning $B_{12}H_{12}^{2-}$ anions could behave as a "lubricant" for Na^+ diffusion, and the hopping of disordered Na^+ among the tetrahedral interstices finally contributed to the superionic conductivity of $Na_2B_{12}H_{12}$.[39] Bimetallic compounds with two types of mobile cations usually show diverse physicochemical properties. Akiba and co-workers surveyed the ion-mobility behavior in bimetallic $LiNaB_{12}H_{12}$, which showed a lower phase-transition temperature (488 K) in comparison with both monometallic $Li_2B_{12}H_{12}$ (615 K) and monometallic $Na_2B_{12}H_{12}$ (529 K).[64] The ionic conductivity of $LiNaB_{12}H_{12}$ was between those of $Li_2B_{12}H_{12}$ and $Na_2B_{12}H_{12}$ below 488 K; however, above 550 K, it could reach 0.79 S cm^{-1}, higher than those of both $Li_2B_{12}H_{12}$ and $Na_2B_{12}H_{12}$ at the same temperature. Through DC polarization (using Li/Li symmetric electrodes), the lithium transport number of $LiNaB_{12}H_{12}$ at
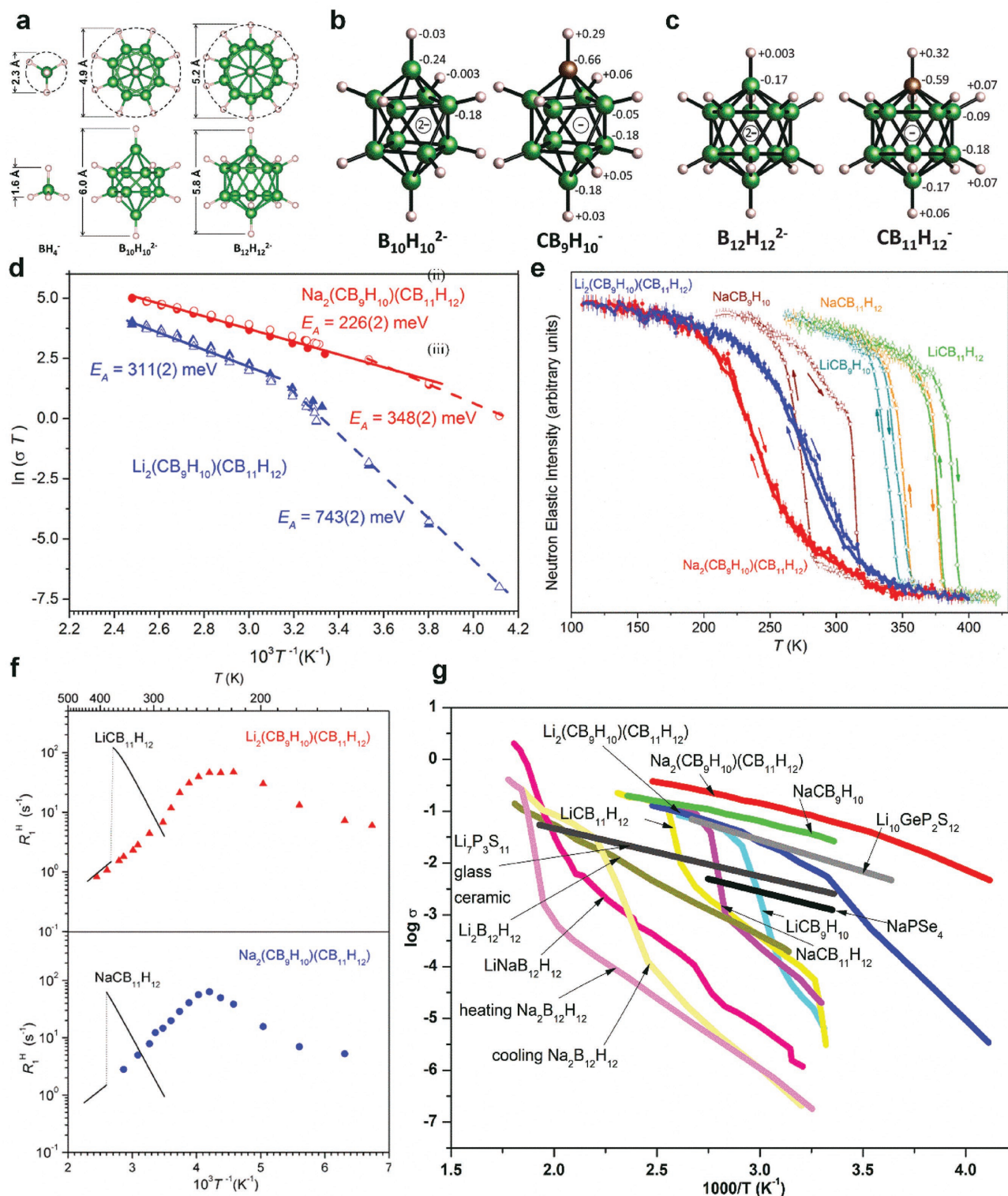
Figure 5. a) Illustrations of the geometric shapes on an identical scale of BH_4^-, $B_{10}H_{10}^{2-}$, and $B_{12}H_{12}^{2-}$ anions, each shown in top and side views. Green balls: B atoms; pink balls: H atoms. b,c) Geometric shapes and Mulliken charges of $B_{10}H_{10}^{2-}$, $CB_9H_{10}^{2-}$, $B_{12}H_{12}^{2-}$, and $CB_{11}H_{12}^-$ anions. Green balls: B atoms; brown balls: C atoms; white balls: H atoms.[24a,70] d) $\ln(\sigma T)$ versus T^{-1} for two solution-dried, cold-pressed $Li_2(CB_9H_{10})(CB_{11}H_{12})$ and $Na_2(CB_9H_{10})(CB_{11}H_{12})$ compounds and the fitted activation energies for the two mixed compounds. Closed and open symbols represent heating and cooling cycles, respectively. e) Temperature dependence of neutron elastic intensity for $Li_2(CB_9H_{10})(CB_{11}H_{12})$ and $Na_2(CB_9H_{10})(CB_{11}H_{12})$ in comparison with those for single-anion component compounds. The arrows indicate the heating and cooling curves, and, for a convenient and rational comparison, the individual data sets have been adjusted and scaled so as to have similar minimum and maximum intensities. f) Temperature dependence of

**ADVANCED
SCIENCE NEWS**
www.advancedsciencenews.com

**ADVANCED
MATERIALS**
www.advmat.de

393 K was determined to be 0.91; however, above 433 K, the lithium transport number fell to 0.71, indicating that the fraction of Li$^+$ species decreased at elevated temperature. In addition, unlike Na$_2$B$_{12}$H$_{12}$, LiNaB$_{12}$H$_{12}$ presented favorable smaller conductivity hysteresis in the cooling process, which is similar to that of Li$_2$B$_{12}$H$_{12}$ and indicates that synergetic effects play a significant role in tuning the ionic-conductive behaviors of polyhedral borohydrides. Na$_2$B$_{10}$H$_{10}$ was also verified as a typical fast ionic conductor.[25a] When heated above 360 K, the ordered lattices of Na$_2$B$_{10}$H$_{10}$ converted to disordered fcc phase with vacancy-rich Na$^+$ sublattices, accompanied by a reduced activation energy of 190 meV. The large sizes and spheroidal shapes of B$_{10}$H$_{10}^{2-}$ offered remarkable liquid-like ionic conductivity at high temperature, e.g., ≈0.01 S cm^{-1} at 383 K, which was ≈2 orders of magnitude higher than for both Na$_2$B$_{12}$H$_{12}$ and ordered Na$_2$B$_{10}$H$_{10}$. The results based on neutron elastic-scattering fixed-window scans suggested that the reorientational mobility of B$_{10}$H$_{10}^{2-}$ experienced a dramatic change around the transition temperature. The obtained reorientational jump frequency (10^{10} s^{-1}) of the high-T disordered phase was ≈2 orders of magnitude higher than that in the low-T ordered phase (10^8 s^{-1}). The ellipsoidal-shaped B$_{10}$H$_{10}^{2-}$ anions could provide more spacious Na$^+$ corridors, resulting in better ionic conductivity and lower activation energy than the near-spherical B$_{12}$H$_{12}^{2-}$ anions.[25a] Appropriate modification of Na$_2$B$_{10}$H$_{10}$ may bring higher ionic conductivity. Remhof and co-workers reported a Na$_2$(B$_{12}$H$_{12}$)$_{0.5}$(B$_{10}$H$_{10}$)$_{0.5}$ SSE, which presented excellent Na$^+$ conductivity at lower temperature than those of the parent Na$_2$B$_{10}$H$_{10}$ and Na$_2$B$_{12}$H$_{12}$ SSEs.[25a,39,67] Further investigations were conducted on Na$_2$(B$_{12}$H$_{12}$)$_{1-x}$(B$_{10}$H$_{10}$)$_x$ with varying molar ratios of Na$_2$B$_{12}$H$_{12}$/Na$_2$B$_{10}$H$_{10}$. Na$_2$B$_{10}$H$_{10}$ and Na$_2$B$_{12}$H$_{12}$ show structural transitions at 373 and 533 K, respectively. The differential scanning calorimetry (DSC) results demonstrated that in Na$_2$(B$_{12}$H$_{12}$)$_{1-x}$(B$_{10}$H$_{10}$)$_x$, when x deviated from 0.5, visible endothermic peaks around 373 and 533 K were seen, indicating the presence of excess precursors in the mixture. There were no observed endothermic peaks for Na$_2$(B$_{12}$H$_{12}$)$_{0.5}$(B$_{10}$H$_{10}$)$_{0.5}$ SSEs, and only a single phase was observed in the XRD patterns, confirming the full reaction between Na$_2$B$_{12}$H$_{12}$ and Na$_2$B$_{10}$H$_{10}$ to form the Na$_2$(B$_{12}$H$_{12}$)$_{0.5}$(B$_{10}$H$_{10}$)$_{0.5}$ composite. As reflected by the cyclic voltammetry (CV) measurements using Na/ Na$_2$(B$_{12}$H$_{12}$)$_{0.5}$(B$_{10}$H$_{10}$)$_{0.5}$ SSE/Pt (1.6–5.5 V) for oxidative stability and Na/Na$_2$(B$_{12}$H$_{12}$)$_{0.5}$(B$_{10}$H$_{10}$)$_{0.5}$ SSE/Al (–0.5 to 6 V) for reductive stability, Na$_2$(B$_{12}$H$_{12}$)$_{0.5}$(B$_{10}$H$_{10}$)$_{0.5}$ presented a wide electrochemical window of 0–3 V.

2.2.2. LiCB$_n$H$_{n+1}$/NaCB$_n$H$_{n+1}$ (n = 9, 11) Monocarborane SSEs

Due to the isoelectronic properties of CH with BH$^-$, carbon substitution of one vertex B atom in the B$_{10}$H$_{10}^{2-}$ or B$_{12}$H$_{12}^{2-}$ group will give rise to hetero-polyborohydride anions, with formulas

of CB$_9$H$_{10}^-$ and CB$_{11}$H$_{12}^-$, respectively. CB$_{11}$H$_{12}^-$ as a monovalent hetero-polyborohydride anion presents distinctive features including weak coordinating properties (less-nucleophilic properties), hydrophobic properties, low metabolic reactivity, and highly delocalized negative charges.[68] SSEs with monovalent carborane anions (CB$_9$H$_{10}^-$ or CB$_{11}$H$_{12}^-$) could yield a reduced stoichiometric ratio (1:1) of cations:anions in comparison with those employing divalent anions (2:1 cations:anions). Owing to the weakly coordinating property and the halved negative charges of carborane anions (CB$_9$H$_{10}^-$ or CB$_{11}$H$_{12}^-$), the cations of the corresponding salts occupy sites with a smaller electrostatic well, which may reduce the activation energy barrier, facilitate the fast diffusion of cations, and make these materials ideal superionic-conductive SSEs.[12d,69]

Tang et al. developed the first carborane-type SSEs in 2015.[70] Both LiCB$_{11}$H$_{12}$ and NaCB$_{11}$H$_{12}$ were in ordered orthorhombic phase at room temperature, and, in comparison with their analogues Li$_2$B$_{12}$H$_{12}$ and Na$_2$B$_{12}$H$_{12}$, they presented decreased phase-transition temperatures (400 and 380 K, respectively). LiCB$_{11}$H$_{12}$ exhibited even higher ionic conductivity ≈0.15 S cm^{-1} at 403 K than that of Li$_{10}$GeP$_2$S$_{12}$ at the same temperature.[17d] Moreover, NaCB$_{11}$H$_{12}$ exhibited an ionic conductivity of 0.12 S cm^{-1} at 383 K. In addition, the DC conductivity measurements confirmed the near-unity cation transport numbers of LiCB$_{11}$H$_{12}$ and NaCB$_{11}$H$_{12}$. Although the utilization of Mg(CB$_{11}$H$_{12}$)$_2$ as an SSE has not been investigated at present, the applicability of Mg(CB$_{11}$H$_{12}$)$_2$ as a viable liquid–electrolyte component has been demonstrated in the Mg(CB$_{11}$H$_{12}$)$_2$/tetraglyme electrolyte system, coupled with favorable high anodic stability and good compatibility with Mg.[69a] Furthermore, the addition of water into Mg(CB$_{11}$H$_{12}$)$_2$/ tetraglyme electrolyte did not cause any chemical reactions, implying the benign nature of Mg(CB$_{11}$H$_{12}$)$_2$ as electrolyte.[69a] Tang et al. further investigated LiCB$_9$H$_{10}$ and NaCB$_9$H$_{10}$ SSEs, and what is more inspiring, they found that the superior structures can "freeze in" the superionic-conductive phase (in disordered hexagonal symmetry) at the low temperature of 332 and 290 K, respectively.[24a] The liquid-like ionic conductivities of LiCB$_9$H$_{10}$ and NaCB$_9$H$_{10}$ compounds were 0.03 S cm^{-1} (354 K) and 0.03 S cm^{-1} (297 K), respectively. Upon further transformation to the disordered phase, the CB$_9$H$_{10}^-$ anions losing their initial orientational specificity may adopt the form of fully spherical shaped entities, coupled with expanded cell volume. The volume expansions of disordered LiCB$_9$H$_{10}$ and NaCB$_9$H$_{10}$ lattices were verified. The cell volume of disordered NaCB$_9$H$_{10}$ (353 K, P31c; $a = 6.844$ Å, $c = 10.908$ Å, $V = 442.5$ Å^3) exceeded that of the disordered LiCB$_9$H$_{10}$ (383 K, P31c; $a = 6.829$ Å, $c = 10.754$ Å, $V = 434.3$ Å^3). Additionally, ^{7}Li NMR and ^{23}Na NMR investigations indicated that near the phase-transition temperature, the change in the spin–lattice relaxation rate R_1^{Na} was more abrupt than that of R_1^{Li}. The activation energy of high-T hexagonal NaCB$_9$H$_{10}$ was threefold higher than that

---

proton spin–lattice relaxation rates measured at 28 MHz for Li$_2$(CB$_9$H$_{10}$)(CB$_{11}$H$_{12}$) and Na$_2$(CB$_9$H$_{10}$)(CB$_{11}$H$_{12}$). The black lines represent the fits for the reported proton spin–lattice relaxation rates at the same frequency for LiCB$_{11}$H$_{12}$ and NaCB$_{11}$H$_{12}$. g) Reported ionic conductivity of polyhedral borohydrides as a function of temperature, which include NaCB$_{11}$H$_{12}$,[70] LiCB$_{11}$H$_{12}$,[70] LiCB$_9$H$_{10}$,[24a] Li$_7$P$_3$S$_{11}$,[11a] NaCB$_9$H$_{10}$,[24a] Na$_2$(CB$_9$H$_{10}$)(CB$_{11}$H$_{12}$),[24b] Li$_2$(CB$_9$H$_{10}$)(CB$_{11}$H$_{12}$),[24b] Na$_2$B$_{12}$H$_{12}$,[39] Li$_2$B$_{12}$H$_{12}$,[63a] LiNaB$_{12}$H$_{12}$,[64] NaPSe$_4$,[71] and Li$_{10}$GeP$_2$S$_{12}$.[17d] a) Reproduced with permission.[25a] Copyright 2014, Wiley-VCH. b) Reproduced with permission.[24a] Copyright 2016, Wiley-VCH. c) Reproduced with permission.[70] Copyright 2015, Royal Society of Chemistry. d–f) Reproduced with permission.[24b] Copyright 2016, American Chemical Society.

**ADVANCED
SCIENCE NEWS**

www.advancedsciencenews.com

**ADVANCED
MATERIALS**

www.advmat.de

of hexagonal $LiCB_9H_{10}$, which may come from the different ionic radii of Na^+ and Li^+ (25% contraction). Most lithium salts show lower diffusion barriers than sodium salts when cations migrate through similar channels.[24a] To further improve the ionic conductivity, Tang et al. developed $Li_2(CB_9H_{10})(CB_{11}H_{12})$ and $Na_2(CB_9H_{10})(CB_{11}H_{12})$ salts, which showed the state-of-the-art best ionic-conductive performances of borohydride SSEs.[24b] When heated above 350 K, the ionic conductivity of $Li_2(CB_9H_{10})(CB_{11}H_{12})$ could catch up with those of disordered $LiCB_9H_{10}$ and $Li_{10}GeP_2S_{12}$. $Na_2(CB_9H_{10})(CB_{11}H_{12})$ also exhibited outstanding ionic conductivity, surpassing both $NaCB_9H_{10}$ and $NaCB_{11}H_{12}$ over the whole temperature range. This demonstrates that ligand engineering plays an important role in controlling the ionic conductivity. Among the investigated polyhedral-borohydride SSEs, $Na_2(CB_9H_{10})(CB_{11}H_{12})$ presented the highest ionic conductivity of ≈ 70 mS cm^{-1} at room temperature and a low activation energy of 226 meV (Figure 5d). The neutron elastic-scattering fixed-window scans between 100 and 400 K for the Li and Na sample mixtures demonstrate that, in comparison with the FWSs for pure $NaCB_9H_{10}$, $NaCB_{11}H_{12}$, $LiCB_9H_{10}$, and $LiCB_{11}H_{12}$, the jump rates of highly mobile anion reorientational motions in $Na_2(CB_9H_{10})(CB_{11}H_{12})$ and $Li_2(CB_9H_{10})(CB_{11}H_{12})$ composites have already approached the order of 10^8 reorientaional jumps s^{-1} by around 240 and 210 K, showing transitions from immobile anions in ordered phases ($<10^8$ jumps s^{-1}) to more mobile anions in disordered phases ($>10^{10}$ jumps s^{-1}) at much lower temperature (Figure 5e). The NMR measurements showed that the maximum ^1H spin–lattice relaxation rates R_1^H (corresponding to the H jump rate of $\approx 10^8$ s^{-1}) of $Li_2(CB_9H_{10})(CB_{11}H_{12})$ and $Na_2(CB_9H_{10})(CB_{11}H_{12})$ were approached near 230 and 220 K, respectively (Figure 5f), indicating that the high anion reorientational mobility of $Li_2(CB_9H_{10})(CB_{11}H_{12})$ and $Na_2(CB_9H_{10})(CB_{11}H_{12})$ could be retained at low temperature. The cation mobility was also investigated by way of the ^{23}Na NMR spectra of $Na_2(CB_9H_{10})(CB_{11}H_{12})$, and the observed extremely narrow ^{23}Na NMR lineshape suggested a fast Na^+ diffusive motion at room temperature. The $Na_2(CB_9H_{10})(CB_{11}H_{12})$ delivered a slightly reduced ionic conductivity with decreasing temperature, from ≈ 70 mS cm^{-1} at 300 K to 5 mS cm^{-1} at 240 K (Figure 5g), indicating that the high ionic conductivity of $Na_2(CB_9H_{10})(CB_{11}H_{12})$ was well preserved over a broad temperature range. In comparison with its closest competitor Na_3PSe_4, the ionic conductivity of $Na_2(CB_9H_{10})(CB_{11}H_{12})$ at 300 K is 50 times higher than that of Na_3PSe_4.[71]

2.2.3. Theoretical Predictions of CN-Substituted Polyhedral Borohydride SSEs

Typically, from the viewpoint of designing a superionic conductor, the importance of searching electrophilic anions has been recognized. The anions with high electron affinities (EAs) and adopting large near-spherical borohydride skeletons are expected to deliver weaker cation–anion interactions and facilitate fast cation transport. Ligand manipulation has been proposed as an important and effective strategy to increase the electron affinities of anions. For example, in the case of C_6H_6, an increase in the electron affinity from -1.15 eV in C_6H_6 to 3.53 eV in $C_6(CN)_6$ was observed after replacing H by CN groups, indicating the increased electrophilic performance.[72] CN ligands with electron affinity up to 3.86 eV and large sizes mimic the chemistry of halogens as effective negative moieties. CN ligands are superior to H atoms, which possess a much smaller electron affinity (0.75 eV). $B_{12}(CN)_{12}^{2-}$ and $CB_{11}(CN)_{12}^{2-}$ groups are derived from $B_{12}H_{12}^{2-}$ and $CB_{11}H_{12}^{2-}$ when H atoms are fully replaced by CN groups.[73] Zhao et al. systematically surveyed the electron affinity of $B_{12}(CN)_{12}^{2-}$ and $CB_{11}(CN)_{12}^{2-}$, based on consistent calculations using both real space (Gaussian03) and reciprocal space (Vienna Ab Initio Simulation Package (VASP)) approaches.[72] The binding energy of the first electron in $B_{12}(CN)_{12}^{2-}$ (8.56 eV) was nearly twice as high as that of $B_{12}H_{12}^{2-}$ (4.57 eV). The binding energy of the second electron in $B_{12}(CN)_{12}^{2-}$ reached 5.28 eV, which was ≈ 6 times higher than for $B_{12}H_{12}^{2-}$, indicating a remarkable electrophilic property compared to halogen atoms. This demonstrated that M^{n+} (M = Li, Na, Mg, ...) in $M_2[B_{12}(CN)_{12}]_n$ should suffer from less diffusion restriction than the identical M^{n+} in $M_2(B_{12}H_{12})_n$. In the case of the $CB_{11}H_{12}$ group, only one extra electron was required to satisfy the Wade–Mingos rule, and the binding energy of the first electron was around 5.39 eV. One more electron added to $CB_{11}H_{12}^-$ would cause autodetachment of electrons, indicating the instability of $CB_{11}H_{12}^{2-}$ anions. Nevertheless, in comparison with the unstable isoelectronic $CB_{11}H_{12}^{2-}$, the $CB_{11}(CN)_{12}^{2-}$ divalent anion yielded an anomalously high EA of 1.07 eV for a second electron in a reduced point group symmetry C_1. This illustrates that $CB_{11}(CN)_{12}^{2-}$ groups are stable and could be potentially used for Mg ion batteries. The Li^+/Mg^{2+} dissociation energies in diverse salts are presented in **Figure 6**a. $CB_{11}(CN)_{12}^-$ presents the smallest Li^+ dissociation energy (4.09 eV), and this value is about 20% lower than that of $LiCB_{11}H_{12}$ (5.08 eV), predicting faster Li^+ mobility in $LiCB_{11}(CN)_{12}$ than in $LiCB_{11}H_{12}$.[72] In Mg salts, the Mg^{2+} dissociation energies of $MgCB_{11}(CN)_{12}$ and $MgB_{11}(CN)_{12}$ are 18.30 and 17.46 eV, respectively, and these values are smaller than that of $MgB_{12}H_{12}$ (21.31 eV). These calculated dissociation energies and electron affinities of cyano-borohydride derivatives (e.g., $LiCB_{11}(CN)_{12}$, $Li_2CB_{11}(CN)_{12}$, $Li_2B_{12}(CN)_{12}$, $MgB_{12}(CN)_{12}$, and $MgCB_{11}(CN)_{12}$) theoretically favor the further development of halogen-free superionic-conductive SSEs, with promising ionic conductivities, even surpassing 0.1 S cm^{-1}. The ligand replacement may additionally rectify the poor oxidation stability of borohydrides, but this requires verification through subsequent relevant research.

Ligand manipulation of polyhedral borohydrides is reminiscent of an interesting and thorough review on the substituted carba-closo-dodecaborate anion (Figure 6b–e), which studied a variety of $CB_{11}H_{12}^-$ derivatives.[68b] Nowadays, the substituted $CB_{11}H_{12}^-$ composites are mainly limited by their high costs, which require efficient high-yield one-step/two-step synthesis procedures. Michl and co-workers attempted to list all the known derivatives, involving 376 types of substituted $CB_{11}H_{12}^-$ in their research, and many of derivatives are considered as chemically inert to the most aggressive reagents and as having the uttermost oxidation stability.[68b] Nevertheless, it is important to note that anions with poor rotational mobility are not desirable for SSEs and may cancel out the benefits of their weak coordination properties. Anyway, in future research, with

**ADVANCED
SCIENCE NEWS**

www.advancedsciencenews.com

**ADVANCED
MATERIALS**

www.advmat.de
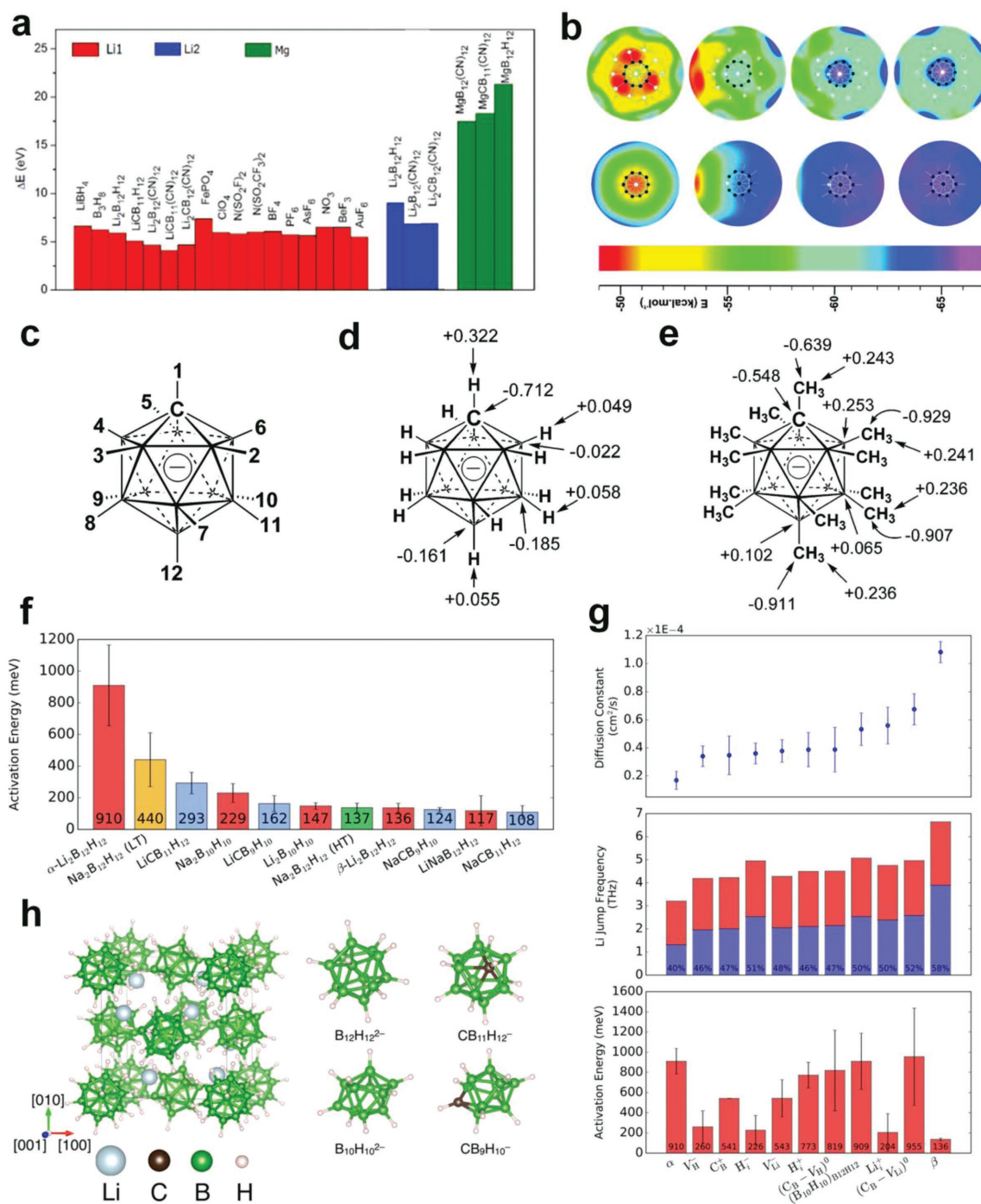
Figure 6. a) Dissociation energies of cations (ΔE_{Li1}, ΔE_{Li2}, ΔE_{Mg}) in Li and Mg borohydrides.[72,73] b) Electrostatic potential around (top) $CB_{11}(CH_3)_{11}^-$ icosahedron and (middle) $CB_{11}H_{11}^-$ icosahedron, respectively. The corresponding radii of the spheres are 5.2 and 5.7 Å, respectively, 2.5 Å from the hydrogen atoms in the $CB_{11}H_{11}^-$ icosahedron or methyl carbon atoms in the $CB_{11}(CH_3)_{11}^-$ icosahedron. Views along exocyclic bonds; from left to right, looking at vertex positions that are numbered 1, 2, 7, and 12 in (c). c) Vertex numbering in the $CB_{11}H_{11}^-$ icosahedron. d) Calculated natural atomic charges in $CB_{11}H_{11}^-$ icosahedron. e) Calculated natural atomic charges in $CB_{11}(CH_3)_{11}^-$ icosahedron. f) Calculated activation energies from ab initio molecular dynamics simulations for cation diffusivity in Li and Na closo-(carbo)boranes. The red, green, blue, and orange colors represent the point group symmetries of fcc, bcc, orthorhombic, and monoclinic structures, respectively. g) Trends in Li^+ diffusivity in $Li_2B_{12}H_{12}$ upon perturbations to the stoichiometry and composition: top) diffusion constants at 800 K calculated from the mean-squared displacement; middle) associated frequency of discrete jumps; and bottom) barriers computed from temperature-dependent Arrhenius plots. h) Illustration of fcc $Li_2B_{12}H_{12}$ in the low-temperature α phase. A structural chart of the different anion species is shown on the right ($B_{12}H_{12}^{2-}$, $B_{10}H_{10}^{2-}$, $CB_{11}H_{12}^-$, and $CB_9H_{10}^-$). b–e) Reproduced with permission.[68b] Copyright 2006, American Chemical Society. f–h) Reproduced with permission.[74] Copyright 2017, American Chemical Society.

**ADVANCED
SCIENCE NEWS**

www.advancedsciencenews.com

**ADVANCED
MATERIALS**

www.advmat.de

the support of high-throughput theoretical calculations, it will be promising to construct a candidate library for superionic-conductive borohydride SSEs according to specific criteria.

2.2.4. Thermodynamics Studies

Preliminary results suggest that polyhedral borohydrides follow the trends that carboranes have the highest conductivity, $B_{10}H_{10}$ are moderate, yet more conductive than $B_{12}H_{12}$, and Na salts are more conductive than Li salts. For readers and researchers wanting deeper details, more studies are needed to scrutinize the mechanisms behind high ionic conductivity and calculations that can predict the optimum SSE configurations. Based on AIMD simulations (with the Quantum Espresso code) and the Perdew–Burke–Ernzerhof (PBE) exchange correlation function, Varley et al. probed the effects of various perturbations on the ionic conductivities of polyhedral borohydrides (Figure 6f–h).[74] The calculations were conducted by taking $Li_2B_{12}H_{12}$ as an example. The point group symmetry of anions has been verified as being unrelated to the ionic conductivity of polyhedral borohydrides, with the investigated point group symmetry of anions involving bcc, fcc, orthorhombic, and monoclinic structures. Although high-T β-$Li_2B_{12}H_{12}$ shows higher ionic conductivity than low-T α-$Li_2B_{12}H_{12}$, the fcc symmetry of $Li_2B_{12}H_{12}$ is maintained through the transition from α- to β-phase at high temperature, while the volume and Li arrangement in the lattice changes, suggesting that the diffusivity of cations is independent of the point group symmetry of crystals. A defined angular autocorrelation function was introduced to depict the rotation of $B_{12}H_{12}^{2-}$ anions[74]

$$\phi(t) = \langle \hat{r}(t) \cdot \hat{r}(0) \rangle \tag{1}$$

where $\hat{r}$ is the unit vector from the mass center of the anion to a constituent boron atom. The decay of $\phi(t)$ is a function of volume so that $\phi(t)$ behaves as a bridge connecting volume changes and anion rotation rates. The test results indicated that a smaller volume ($V = 0.95V_\alpha$, where V_α is the volume of the α-phase $Li_2B_{12}H_{12}$) did not contribute to the enhancement of anion rotation rates, and only when the volume increased to V_α, the anion rotation process could be triggered. The enhancement of the anion rotation rate saturated at a volume around $1.2 V_\alpha$ and reached an exponential superfast rotation rate before declining at a larger volume. The observed volume ($1.08 V_\alpha$) of β-$Li_2B_{12}H_{12}$ reasonably explains the higher ionic conductivity and faster anion rotational frequencies compared to α-$Li_2B_{12}H_{12}$ with V_α. To elucidate the initially observed trends and isolate the effects of perturbations, related perturbations are summarized: i) hydrogen interstitials (H_i^+ and H_i^-), ii) aliovalent anion substitution by $CB_{11}H_{12}^-$ (C_B^+) or $B_{12}H_{11}^{3-}$ (V_H^-), iii) isovalent anion substitutions between $B_{12}H_{12}^{2-}$ and $B_{10}H_{10}^{2-}$ ($B_{10}H_{10(B12H12)}$), iv) Li vacancies (V_{Li}^-) or interstitials (Li_i^+), and v) volume expansion in the same point group symmetry. They are further grouped according to intrinsic cation population: charge-neutral systems ((C_B–V_H)^0, (C_B–V_{Li})^0, and ($B_{10}H_{10}$)$_{B12H12}$), cation over-population systems (V_H^- and Li_i^+), and cation-underpopulated systems (C_B^+ and V_{Li}^-). The computed barriers for creating different fluctuations fall in the order: charge-neutral system (above 773 meV) > cation-underpopulation system (540 meV)

> cation-overpopulation system (260 meV), indicating that the easiest cation hopping exists in the local cation-excess system. The Li^+-rich complexes showed a lower activation energy and faster diffusivity than the Li^+-depleted composites. This may have originated from the high-energy states of Li^+-excess complexes since it is much easier to form an undercoordinated complex than an overcoordinated complex. Creating perturbations of the charge-neutral systems, (C_B–V_H)^0, (C_B–V_{Li})^0, and ($B_{10}H_{10}$)$_{B12H12}$ were energetically the most expensive. For the charge-neutral systems, extra energy is consumed to initially transform them to intermediate pairs of overpopulated and underpopulated local complexes. This was in excellent agreement with the further confirmation provided by separating the barriers in the (C_B–V_{Li})^0 system. The calculated value of the binding energy between the constituent defect pairs was around 400 meV, which fitted well with the divergence between the Li^+-diffusion barrier (955 meV) and that of individual C_B^+ or V_{Li}^- defects (541–543 meV). Varley et al. rationally analyzed the previous studies and revealed the individual effects of different modifications. Furthermore, to improve the ionic conductivity of polyhedral borohydride, favorable perturbations are summarized, such as carbon doping, anion alloying, modified cation stoichiometry, large cation substitution, and chemically modified anions.

As seen above, after the transition to disordered phase (driven by thermodynamics), the ionic conductivity can increase by several orders of magnitude. This requires a better understanding of the correlation between cationic diffusion and entropy changes. Ganesh and co-workers addressed this issue through molecular-dynamics simulations using nanosized β-Li_3PS_4 as an example.[75] In SSEs, the cations occupy the free spaces between anions and accomplish the diffusive process through the hopping of mobile carriers (i.e., vacancies, interstitials, or a concerted motion of ions) from one lattice site to another. The self-diffusion coefficient can be estimated from the following equation[75]

$$D \sim fa^2\nu e^{\left(\frac{\Delta S}{k_B} - E_a/k_B T\right)} \tag{2}$$

where f is a geometric factor, and a, ΔS, E_a, and ν are the diffusion length, entropy change, activation energy, and jump frequency of the diffusion process, respectively.[75] As seen from this equation, a positive correlation between the diffusion coefficient and the entropy increase, ΔS, has been identified. ΔS at a given temperature is determined by finding the contributions of the configurational entropy term (S_{conf}) and the vibrational entropy term (S_{vib}) associated with diffusion mechanisms. According to the Nernst–Einstein relation, $\sigma_{dc} \sim e^{S_{conf}/k_B}$ (where σ_{dc} is the (dc) ionic conductivity), the configurational entropy has a dominant influence on the ionic conductivity. The configurational entropy is expressed as[75]

$$S_{conf} = k_B \ln(\Omega) \tag{3}$$

where Ω represents the possible configurational states, and it behaves as a bridge for connecting carriers (i.e., vacancies and mobile ions) and ionic conductivity. $\Omega \sim {}^N C_m$, where ${}^N C_m$ stands for the configurational states in one unit (where N is the number of Li-ion adsorption sites, and m represents the

number of mobile ions). When $m = N/2$, i.e., at the particular composition where the number of vacancies equals that the number of mobile ions (half of the Li$^+$ adsorption site number), the maximal Ω and optimal ionic conductivity are achieved.[75] This illustrates that the obtained maximal configurational entropy is the very condition for achieving the highest ionic conductivity, in which the number of mobile Li ions equals the number of mobile vacancies in a given topology of the host lattice.[75] This is also consistent with the knowledge that Li ions hop between lattice sites, and the increasing number of configurational states create more connections between different lattice sites, thus promoting the total ionic conductivity. In addition, the concentration of cation vacancies in Li(BH$_4^-$, B$_{10}$H$_{10}^{2-}$, and B$_{12}$H$_{12}^{2-}$), Na(BH$_4^-$, B$_{10}$H$_{10}^{2-}$, and B$_{12}$H$_{12}^{2-}$), and Mg(BH$_4^-$ and B$_{12}$H$_{12}^{2-}$) compounds is assessed by calculations of the vacancy-formation energies, which are estimated using two strategies depending on phase equilibria and the cation-extraction reaction, based on charge-neutral configurations.[76] According to the results from phase equilibria, BH$_4^-$-containing phases have a lower vacancy-formation barrier than B$_{12}$H$_{12}^{2-}$-containing phases, and monovalent cations have a lower one than divalent cations. Based on these informative discussions and results, insight into the intriguing interplay between thermodynamics and kinetics in cation diffusivity can be achieved, and the significance of manipulating certain compositions to achieve better configurational entropy has been recognized, which may further optimize the macroscopic ionic conductivity.

3. Borohydrides as Solid-State Electrolytes for All-Solid-State Batteries

During their short history, borohydrides have been becoming viable SSEs with incremental progress toward real implementation in ASSBs (**Table 1**). Aside from their impressive superionic conductivity, the unique feasibility of borohydrides as SSEs also arise from the following aspects: i) Light weight: Unemoto et al. compared the densities of oxides, sulfides, and complex hydrides. Complex hydrides appeared to be the lightest SSEs.[22] Borohydrides, which are composed of a few light atoms, inherit the favorable low densities. The light SSEs show superiority in terms of reducing the net weight of the battery, affording better efficiency and greater energy yield, which is helpful for the development and integration of ASSBs. ii) Good compatibility with Li/Na/Mg metals: Stable borohydride–Li interfaces are confirmed, suggesting reversible Li deposition and stripping in the battery operation.[23b] The compatibilities of borohydrides with Li/Na/Mg metals mainly originate from their high reducibility. iii) High ductility: the formation of the desired intimate interface between the electrode and borohydride is easily realized by a simple and straightforward cold-pressing process, owing to the favorable ductile nature of borohydrides. Recent research on the implementation of borohydride SSEs in ASSBs will be discussed in the following section.

3.1. Borohydrides as SSEs Paired with Different Anode Materials for ASSBs

3.1.1. MgH$_2$ Electrodes

As a representative complex hydride electrode material, MgH$_2$ with a promising theoretical capacity of 2038 mA h g^{-1} shows electrochemical reactivity toward Li in a relatively low working voltage range (0.1–1.0 V vs Li$^+$/Li).[77] Only small polarization (<0.2 V) at an average potential of 0.5 V versus Li$^+$/Li is observed, suggesting an excellent mass-transport process in

Table 1. Solid-state batteries based on borohydride SSEs and comparisons with other SSE.

Cell	SSEs	Discharge capacity [mA h g^{-1}]	T [K]	Current density	Cycles	Ref.
Li/TiS$_2$	$(100 - x)(0.75Li_2S \cdot 0.25P_2S_5) \cdot xLiBH_4$	200	293	0.064 mA cm^{-2}	5	[37]
LiIn/TiS$_2$	90LiBH$_4$:10P$_2$S$_5$	195	300	0.114 mA cm^{-2}	10	[38]
Li/TiS$_2$	LiBH$_4$	180	393	0.2C	300	[81]
Li/TiS$_2$	LiCB$_{11}$H$_{12}$	180	403	0.2C	5	[70]
Li/TiS$_2$	Li$_2$B$_{12}$H$_{12}$	190	333	–	10	[65]
Li/Li$_3$PO$_4$–LiCoO$_2$	LiBH$_4$	89	393	0.05 mA cm^{-2}	30	[88]
Li/MgH$_2$	LiBH$_4$	924	393	800 mA g^{-1}	50	[77a]
Li/S	LiBH$_4$	750	393	0.25 mA cm^{-2}	45	[25b]
Li/S	LiBH$_4$–LiCl	636	373	0.15 mA cm^{-2}	5	[86]
Li/S	MCM41-confined LiBH$_4$	1306	328	6.2 µA cm^{-2}	40	[85]
Li/S	Li$_2$S–P$_2$S$_5$	400	353	84 mA g^{-1}	17	[34d]
In/L$_2$S	75Li$_2$S·25P$_2$S$_5$	860	298	50.2 mA g^{-1}	20	[34e]
LiIn/S	Li$_6$PS$_5$Br	1080	–	167.5 mA g^{-1}	50	[34f]
LiAl/S-CMK-3	Li$_{3.25}$Ge$_{0.25}$P$_{0.75}$S$_4$	1300	298	0.13 mA cm^{-2}	20	[34g]
Li/naphthylene	LiBH$_4$	593	393	425 mA g^{-1}	65	[84]
Li/Li$_4$Ti$_5$O$_{12}$	Li(BH$_4$)$_{1-x}$(NH$_2$)$_x$ ($x = 2/3$)	140	313	175.1 mA g^{-1}	400	[31]
Na/NaCrO$_2$	Na$_2$(B$_{12}$H$_{12}$)$_{0.5}$–(B$_{10}$H$_{10}$)$_{0.5}$	80	–	24 mA g^{-1}	250	[67]

**ADVANCED
SCIENCE NEWS**

www.advancedsciencenews.com

**ADVANCED
MATERIALS**

www.advmat.de

MgH_2. A surprisingly fast H^- diffusivity from Mg-phase to Li-phase may contribute to the favorable performance. The electrochemical reaction of MgH_2 with Li involves the Li^+ insertion/extraction reaction[77a]

$$MgH_2 + 2Li^+ + 2e \leftrightarrow 2Mg + 2LiH \tag{4}$$

A MgH_2-based ASSB in the MgH_2–1%Nb_2O_5|80Li_2S:20P_2S_5|Li configuration was investigated, even though an ASSB with sulfide SSE presented fairly low initial Coulombic efficiency around 30% and was cycled for only one time.[78] Zeng et al. designed a MgH_2-based ASSB with the MgH_2–$LiBH_4$|$LiBH_4$|Li configuration after replacing 80Li_2S:20P_2S_5 with $LiBH_4$ SSE (**Figure 7**a,b). This design for a MgH_2-based ASSB with typical components was inspired by the following benefits: i) the good compatibility between MgH_2 and $LiBH_4$; ii) the accelerated H^- transport in MgH_2 after the introduction of $LiBH_4$, which may facilitate fast H^- mobility in MgH_2; and iii) the high ionic conductivity (>1 mS cm^{-1}, 393 K) of $LiBH_4$, which provides fast Li^+ transport.[77a] With the $LiBH_4$ SSE, the MgH_2-based ASSB delivered an initial reversible capacity of 1586 mA h g^{-1} at 800 mA g^{-1} and a preserved capacity of 924 mA h g^{-1} after 50 cycles, with Coulombic efficiency up to 99.5%. The initial Coulombic efficiency of the ASSB using the $LiBH_4$ SSE was much better than that utilizing the 80Li_2S:20P_2S_5 SSE. The benign nature and dual functions of $LiBH_4$ with MgH_2 electrode were further verified by comparing the cycling performance of two ASSBs using different electrodes (MgH_2–$LiBH_4$–VGCF and MgH_2–80Li_2S:20P_2S_5–VGCF electrodes, where VGCF represents "vapor grown carbon nanofiber") and the same 80Li_2S:20P_2S_5 SSEs. The ASSB with MgH_2–$LiBH_4$–VGCF electrode exhibits a high capacity ≈1000 mA h g^{-1}, while that with the MgH_2–80Li_2S:20P_2S_5–VGCF electrodes fades quickly to near 0 (Figure 7c,d), indicating that $LiBH_4$ SSEs may offer more convenient ionic-conduction paths than sulfide SSEs for the electrochemical reactions of MgH_2.[79]

Borohydride SSEs match well with complex hydride electrodes and have shed light on improving the cycling performance of ASSBs with electrodes based on other metal hydrides (i.e., TiH_2, Mg_2FeH_6, Mg_2CoH_5, Mg_2NiH_4, $ZrV_2H_{4.9}$, and $TiFeH_2$).

3.1.2. TiS$_2$ Electrodes

As an anode for the lithium-ion battery, TiS_2 presents a theoretical capacity of 239 mA h g^{-1}. The reversible lithiation and delithiation processes in TiS_2 proceed as[22,80]

$$TiS_2 + xLi^+ + xe^- \rightleftharpoons Li_xTiS_2 \tag{5}$$

A TiS_2-based ASSB utilizing a 67(0.75Li_2S·0.25P_2S_5)·33 $LiBH_4$ glass SSE was successfully operated at 298 K, and it delivered a discharge capacity of 223 mA h g^{-1} under 0.064 mA cm^{-2} in the first cycle, equivalent to 93% of the theoretical capacity.[37] In the following four cycles, high Coulombic efficiency (≈99%) and lithium-storage capacity (200 mA h g^{-1}) were achieved. The overlapping charge and discharge capacities indicated negligible irreversible capacity loss of this ASSB. Unemoto

et al. further investigated pure $LiBH_4$ SSE paired with TiS_2 and Li electrodes.[81] The cross-sectional scanning electron microscopy (SEM) image of a TiS_2–$LiBH_4$ electrode composite shown in Figure 7e demonstrates a favorable intimate active-material/electrolyte interface between TiS_2 and $LiBH_4$, and the TiS_2 component is entirely covered by $LiBH_4$ SSEs, demonstrating the highly deformable nature of both materials. The ASSB with a 2TiS_2–3$LiBH_4$|$LiBH_4$|Li configuration presented a stable capacity over 300 discharge–charge cycles, with a Coulombic efficiency of ≈99% at 0.2C (393 K) (Figure 7f). In addition, the preserved discharge capacity reached 75% of its theoretical capacity at the 300th cycle. The research further verified that exposing $LiBH_4$ to atmospheric-pressure oxygen had negligible side effects on battery life. A $Li_4(BH_4)_3I$ SSE (2 × 10^{-3} S cm^{-1} at 393 K and 6 × 10^{-4} S cm^{-1} at 363 K) was studied when paired with TiS_2 and lithium electrodes.[22] The performances of the TiS_2/$Li_4(BH_4)_3I$|$Li_4(BH_4)_3I$|Li ASSBs at 393 and 363 K were compared. The discharge capacity (2nd cycle, at 393 K) was 215 mA h g^{-1} at 0.05C, while that at 363 K was 200 mA h g^{-1} at 0.02C. At the 10th cycle, the corresponding discharge capacities were 205 and 185 mA h g^{-1}, respectively. In comparison with ASSBs using the $LiBH_4$ SSE, a slight deterioration of the battery cycling life was observed at both temperatures. The reason for the performance divergence may need further examination. Apart from SSEs with BH_4^- groups, the feasibility of polyhedral borohydride SSEs paired with a TiS_2 electrode was also probed. Unemoto et al. assembled ASSBs in 2TiS_2–3$Li_2B_{12}H_{12}$(-A)|$Li_2B_{12}H_{12}$(-A)|Li and 2TiS_2–3$Li_2B_{12}H_{12}$(-B)|$Li_2B_{12}H_{12}$(-B)|Li configurations, which utilized ball-milled $Li_2B_{12}H_{12}$, labeled as $Li_2B_{12}H_{12}$(-A), and anhydrous commercial $Li_2B_{12}H_{12}$, labeled as $Li_2B_{12}H_{12}$(-B), respectively.[65] The ASSB with the configuration of 2TiS_2–3$Li_2B_{12}H_{12}$(-A)|$Li_2B_{12}H_{12}$(-A)|Li was operated at 393 K with an initial discharge capacity of 207 mA h g^{-1} at 0.2C and further yielded a retained discharge capacity of 190 mA h g^{-1} at 0.2C after 10 cycles. When the temperature was decreased to 333 K, the battery could deliver a similar preserved capacity of 193 mA h g^{-1} at 0.05C after 10 cycles. On the other hand, after replacing $Li_2B_{12}H_{12}$(-A) with $Li_2B_{12}H_{12}$(-B), the 2TiS_2–3$Li_2B_{12}H_{12}$(-B)|$Li_2B_{12}H_{12}$(-B)|Li ASSB did not yield reproducible performance, even under a smaller current density (0.02C at 393 K), and the capacity underwent a fast deterioration to 15 mA h g^{-1} after three cycles. The divergence in the battery performance may arise from the different internal resistances, since $Li_2B_{12}H_{12}$(-A) possessed a higher ionic conductivity of 10$^{-2.6}$ S cm^{-1} than that (10$^{-4.4}$ S cm^{-1}) for $Li_2B_{12}H_{12}$(-B) at 393 K. This was further verified by utilizing highly conductive $LiBH_4$ (10$^{-2.7}$ S cm^{-1} at 393 K) as the SSE layer paired with 2TiS_2–3$Li_2B_{12}H_{12}$(-B) and Li electrodes. The ASSB with the 2TiS_2–3$Li_2B_{12}H_{12}$(-B)|$LiBH_4$|Li configuration showed discharge capacities of 171 and 116 mA h g^{-1} for the 2nd and 3rd cycles, respectively, and the performance was much enhanced over that when employing the $Li_2B_{12}H_{12}$(-B) SSE. Nonetheless, with a similar ionic conductivity to $Li_2B_{12}H_{12}$(-A) and $LiBH_4$, the performance of the 2TiS_2–3$Li_2B_{12}H_{12}$(-B)|$LiBH_4$|Li ASSB was still a bit inferior to that with the $Li_2B_{12}H_{12}$(-A) SSE, which may be attributed to the insufficient Li^+ conductivity of the TiS_2 composite electrodes. Tang et al. investigated the cycling performance of an ASSB utilizing highly conductive $LiCB_{11}H_{12}$ (0.15 S cm^{-1}, 403 K) as the SSE, and the ASSB with the
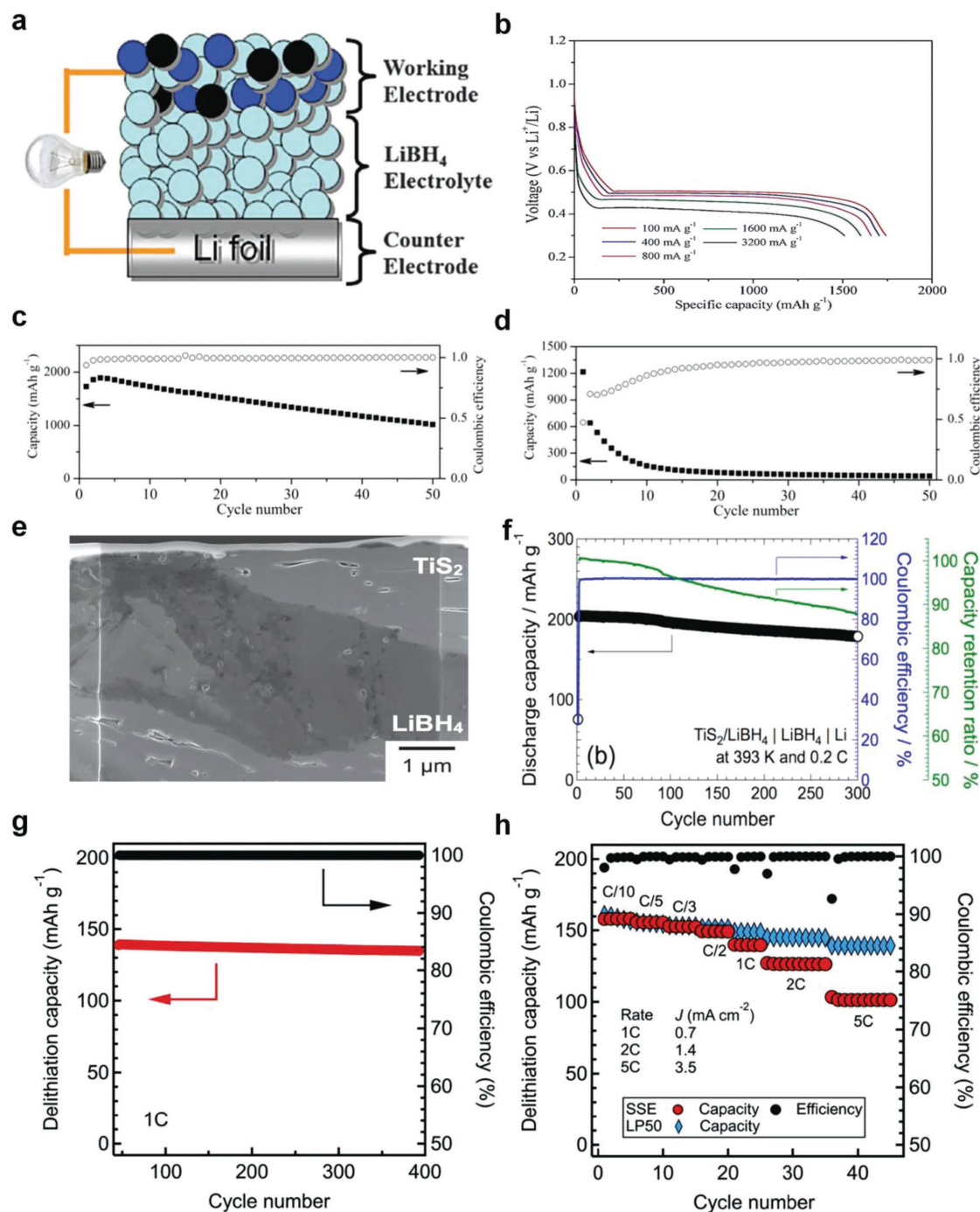
Figure 7. a) Schematic illustrations of ASSB in the MgH₂–LiBH₄|LiBH₄|Li configuration. The dark-blue, black, and light-blue balls in the schematic illustration represent MgH_2, acetylene black, and $LiBH_4$, respectively. b) Initial galvanostatic discharge curve for ASSB with a 1%Nb₂O₅–MgH₂–LiBH₄ electrode under different current densities at 393 K. c) Cycling performance in the voltage range of 0.3–1.0 V for the ASSB with MgH₂–VGCF electrode. The ASSBs were operated at 1000 mA g⁻¹ at 393 K. d) Cycling performance of the ASSB with a MgH₂–80Li₂S·20P₂S₅–VGCF electrode. The ASSBs were operated at 1000 mA g⁻¹ at 393 K. e) Cross-sectional focused-ion-beam SEM (FIB-SEM) image of a TiS₂–LiBH₄ electrode. f) Discharge–charge profiles of bulk-type all-solid-state TiS₂/Li battery paired with LiBH₄ solid-state electrolyte and operated at 393 K and 0.2C. g) Long-term galvanostatic discharge capacity and Coulombic efficiency of the Li₄Ti₅O₁₂ ASSB at 1C (0.7 mA cm⁻²), cycled after the rate test. h) Comparison of the rate performances and Coulombic efficiencies for an LTO ASSB with Li(BH₄)₁₋ₓ(NH₂)ₓ (x = 2/3) SSE and an LTO battery with liquid electrolyte consisting of 1 M LiPF₆ in EC:EMC 1:1 (v:v). The LTO ASSB was cycled at 313 K using Li(BH₄)₁₋ₓ(NH₂)ₓ (x = 2/3) as the SSE. a,b) Reproduced with permission.[77a] Copyright 2015, Royal Society of Chemistry. c,d) Reproduced with permission.[79] Copyright 2017, American Chemical Society. e) Reproduced with permission.[22] Copyright 2014, Wiley-VCH. f) Reproduced with permission.[81] Copyright 2015, American Chemical Society. g,h) Reproduced with permission.[31] Copyright 2017, Wiley-VCH.

**ADVANCED
SCIENCE NEWS**

www.advancedsciencenews.com

**ADVANCED
MATERIALS**

www.advmat.de

TiS$_2$/LiCB$_{11}$H$_{12}$|LiCB$_{11}$H$_{12}$|Li configuration was cycled for five cycles (403 K and 0.2C), with an available discharge capacity of ≈175 mA h g^{-1} after the 3rd cycle and a Coulombic efficiency of 95%.[70] We believe that, in the near future, with more knowledge of the physiochemical/electrochemical properties of polyborohydride SSEs and abundant experience of solid-state battery fabrication, the rational utilization of superionic conductive polyhedral borohydride SSEs will provide a solid future for solid-state batteries.

3.1.3. Li$_4$Ti$_5$O$_{12}$ Electrodes

Owing to the lithiation/delithiation potential (≈1.55 V vs Li/Li$^+$) lying conveniently within the stable operation windows of borohydride SSEs, Li$_4$Ti$_5$O$_{12}$ with fast lithium-storage kinetics was chosen as the electrode for fabricating borohydride-based ASSBs (Figure 7g,h).[31,82] Yan et al. fabricated an ASSB with Li$_4$Ti$_5$O$_{12}$ (LTO) as the working electrode and Li(BH$_4$)$_{1/3}$(NH$_2$)$_{2/3}$ pellet (thickness of 1 mm) as the SSE. The rate performance of the ASSB was tested at different current loads from 0.1C to 5C at 313 K, which was compared with that of a reference battery employing liquid electrolyte.[31] The cycling performance of the two cells overlapped at rates of 0.1–0.5C, and at all tested current rates, the Coulombic efficiencies of both cells approached 100%. At higher rates, the cell with liquid electrolyte possessed higher capacity than the solid-state battery, and the slightly lower capacity might be attributed to the smaller contact area between the LTO electrode and the Li(BH$_4$)$_{1/3}$(NH$_2$)$_{2/3}$ electrolyte in the solid-state battery. On the other hand, after rate testing, the solid-state battery was further cycled at a constant current density of 1C, and it demonstrated very stable cycling performance up to 400 cycles with a capacity of 140 mA h g^{-1}, indicating the high stability of the LTO–Li(BH$_4$)$_{1/3}$(NH$_2$)$_{2/3}$ interface and fast Li$^+$ mobility in the ASSB. A better cycling performance of this ASSB was anticipated when a thinner Li(BH$_4$)$_{1/3}$(NH$_2$)$_{2/3}$ SSE pellet was attached. Vegge and co-workers assembled an ASSB in the LTO|LiBH$_4$–LiI|Li configuration, which was operated with a LiBH$_4$–LiI SSE (1 mS cm^{-1}, 333 K) at 333 K.[83] This ASSB delivered a discharge capacity surpassing 110 mA h g^{-1} in the initial 10 cycles under a current density of 12.7 μA cm^{-2}, but it showed capacity fading of 1.6% per charge–discharge cycle. A strong correlation between discharge capacity and resistance was verified over 200 charge–discharge cycles, and the loss of contact area between the electrolyte and electrodes may account for the capacity fading.

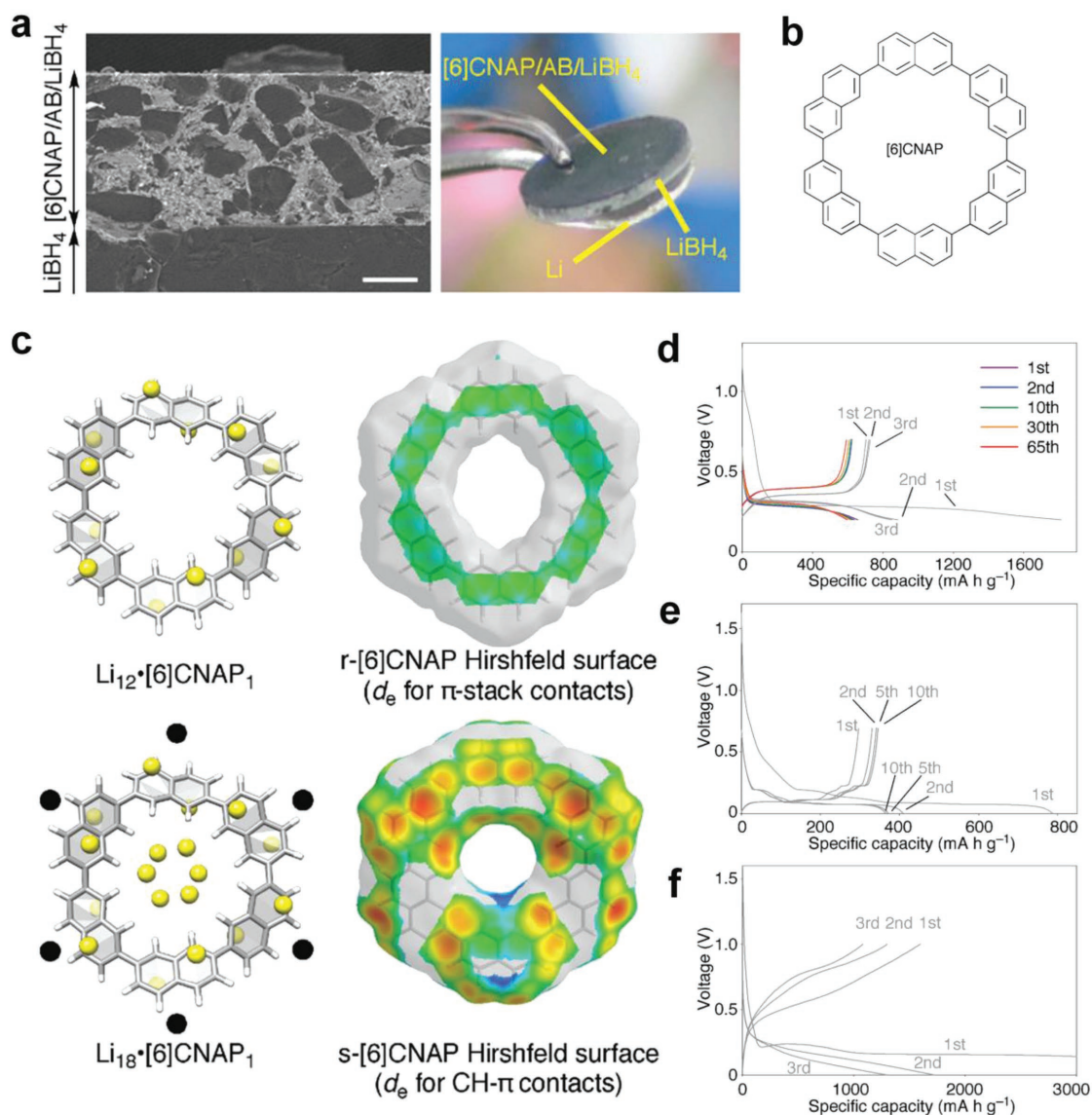### 3.1.4. Cyclo-2,7-Naphthylene Organic Electrodes

Organic electrodes have proven problematic in liquid–electrolyte batteries, partially due to their dissolution in the organic solvent.[84] Organic electrodes paired with SSEs have been seldom reported, although SSE separators could function as robust shields to overcome this problem by suppressing the loss of organic electrode.[84] [6]Cyclo-2,7-naphthylene ([6]CNAP), with the composition of C$_{60}$H$_{36}$ and a central opening macrocyclic structure with a diameter of 0.9 nm, is a promising carbon-rich negative electrode material, and Sato et al.

evaluated the cycling performance of an ASSB utilizing LiBH$_4$ electrolyte and two types of [6]CNAP electrode (including recrystallized [6]CNAP powder, labeled as r-[6]CNAP, and sublimation-collected [6]CNAP, labeled as s-[6]CNAP), at 393 K (**Figure 8**). The performances of the assembled ASSBs using organic electrodes were compared with that of a reference ASSB employing a graphite electrode, as shown in Figure 8d–f. Using acetylene black (AB) as the conductive carbon, the ASSB in the r-[6]CNAP/AB/LiBH$_4$(40:6:60)|LiBH$_4$|Li configuration underwent an initial maturing process at the low charging rate of 85 mA g^{-1}. Then, it was cycled at 425 mA h g^{-1}, and showed a capacity of 593 mA h g^{-1} (95% of the initial value) and Coulombic efficiency of 97% at 65th cycle, with an average voltage around 0.4 V (vs Li/Li$^+$). As for the reference ASSB in the graphite/AB/LiBH$_4$(40:6:60)|LiBH$_4$|Li configuration, it presented capacities around 340 mA h g^{-1} at a smaller current density of 74.4 mA g^{-1}, which is close to the theoretical capacity (372 mA h g^{-1}) of graphite. This illustrates the reliability for evaluating anode materials using the graphite/AB/LiBH$_4$(40:6:60)|LiBH$_4$|Li configuration. Another reference ASSB in the s-[6]CNAP/AB/LiBH$_4$(40:6:60)|LiBH$_4$|Li configuration delivered an ultrahigh initial capacity around 1600 mA h g^{-1} at 85 mA g^{-1}, but dramatic capacity fading to below 70% of the initial value occurred at the 3rd cycle. The r-[6]CNAP as electrode material appeared to be more stable than s-[6]CNAP, which indicates that the battery performance is partially dependent on the preprocessing method of the electrode. Among the three solid-state batteries, the ASSB utilizing r-[6]CNAP exhibited the longest cycling life and the best cycling stability at high current density. The successful operation of the organic-electrode-based ASSBs verified the good compatibility between the borohydrides and organic electrodes.

3.2. Borohydrides as SSEs for ASSBs (Employing Sulfur or Oxide Cathode)

3.2.1. All-Solid-State Li–S Batteries

Borohydride SSEs paired with a S electrode for ASSBs were also investigated. Unemoto et al. assembled a typical S–KB–Maxsorb/LiBH$_4$|LiBH$_4$|Li ASSB, which was operated at 0.25 mA cm^{-2} (0.05C), using fast Li-ion conductive LiBH$_4$ electrolyte and carbon mixtures of Ketjenblack (KB) and Maxsorb to build convenient ionic and electronic conductive channels.[25b] The combined advantages of Maxsorb with a large surface area (3083 g cm^{-3}) and KB with high electrical conductivity can ensure sufficient S–C interfacial area and electric conductivity, which could further facilitate the electron transfer in the insulating elemental sulfur. The ASSB in the S–KB–Maxsorb/LiBH$_4$|LiBH$_4$|Li configuration presented good cycling performance (1140 mA h g^{-1}, 1st cycle, 0.05C; and 710 mA h g^{-1}, 45th cycle, 0.05C) with nearly 100% Coulombic efficiency, which was superior to both reference ASSBs. Limited cycling performances were observed in the two reference solid-state cells of S-KB/LiBH$_4$|LiBH$_4$|Li (950 mA h g^{-1}, 1st cycle, 0.02C; and 400 mA h g^{-1}, 20th cycle) and S–Maxsorb/LiBH$_4$|LiBH$_4$|Li (810 mA h g^{-1}, 1st cycle; 450 mA h g^{-1}, 10th cycle). Das et al. developed a solid-state lithium–sulfur battery

**ADVANCED
SCIENCE NEWS**

www.advancedsciencenews.com

**ADVANCED
MATERIALS**

www.advmat.de

Figure 8. a) Left: SEM image of interfaces between the electrode and electrolyte. The black regions are the LiBH$_4$ electrolyte, and the gray regions are the [6]CNAP active materials; scale bar = 50 μm. Right) Photograph of ASSB with [6]CNAP electrode and LiBH$_4$ SSE. b) Chemical structure of [6]CNAP organic electrode. c) Model structures represent Li storage in [6]CNAP: top left) model structure of Li$_{12}$·[6]CNAP$_1$ (Li$_{1.2}$C$_6$); top right) Hirshfeld surface of [6]CNAP in the r-[6]CNAP crystal; bottom left) model structure of Li$_{18}$·[6]CNAP$_1$ (Li$_{1.8}$C$_6$); bottom right) Hirshfeld surface of [6]CNAP in the s-[6]CNAP crystal. The d_e color mapping for CH–π contacts was scaled in the range of 1.0–2.8 Å. d) Typical discharge–charge profiles of ASSBs in the configuration of r-[6]CNAP electrode/AB/LiBH$_4$ (40:6:60)|LiBH$_4$|Li, where AB = acetylene black, at 393 K. The profiles in gray represent cycling at low current density (85 mA g^{-1} for [6]CNAP), and profiles in color represent cycling at the high current density of 425 mA g^{-1} after three cycles at the low current density. e) Typical discharge–charge profiles of ASSB at the current density of 74.4 mA g^{-1} at 393 K in the configuration of graphite electrode/AB/LiBH$_4$ (40:6:60)|LiBH$_4$|Li. f) Typical discharge–charge profiles of ASSB at the current density of 85 mA g^{-1} at 393 K in the configuration of s-[6]CNAP electrode/AB/LiBH$_4$ (40:6:60)|LiBH$_4$|Li. a–f) Reproduced with permission.[84] Copyright 2016, Wiley-VCH.

using a MCM-41-confined LiBH$_4$ SSE (0.2 mS cm^{-1} at 328 K). When this ASSB was cycled at 6.2 μA cm^{-2} (corresponding to a C-rate of 0.03C), high Coulombic efficiencies (near 100%) were recorded in the first three cycles.[85] It delivered a discharge capacity of 1570 mA h g^{-1} in the second cycle, equivalent to a sulfur utilization rate of 94%, and the capacity gradually dropped after 40 cycles. As the cycle number increased, the resistance of the ASSB also increased, from 1.2 kΩ (before the initial cycle) to 1.8 kΩ (after the 1st cycle) and to 5 kΩ (40th cycle),

verifying that the gradual capacity loss may stem from deteriorating contact between the electrolyte and the electrode and the ultimate formation of an insulating interface. Unemoto et al. assembled a bulk-type solid-state Li–S battery utilizing LiBH$_4$–LiCl SSE (10$^{-3.3}$ S cm^{-1} at 373 K), which was successfully operated at 373 K and 0.03C.[86] An ASSB in the S–KB–Maxsorb/LiBH$_4$–LiCl|LiBH$_4$–LiCl|Li configuration showed an initial discharge capacity of 1377 mA h g^{-1}, and a capacity of 636 mA h g^{-1} at the 5th cycle.[86] In comparison with the Li/S

**ADVANCED
SCIENCE NEWS**

www.advancedsciencenews.com

**ADVANCED
MATERIALS**

www.advmat.de

ASSBs using sulfide SSEs, those using borohydride SSEs currently work under much smaller current densities, and there is still a need for greater improvement.

3.2.2. ASSBs Employing an Oxide Cathode (LiCoO₂, NaCrO₂)

Generally, for oxide cathodes, a protective layer between the cathode and the complex hydride SSE could help to maintain good cycling in ASSBs. For example, a Li/LiBH₄/LiCoO₂ ASSB with a Li₃PO₄ protective intermediate layer (40 nm thick) had a retained capacity ratio of 95% after 30 cycles.[87] Remhof and co-workers studied a Na/Na₂(B₁₂H₁₂)₀.₅(B₁₀H₁₀)₀.₅/NaCrO₂ ASSB, which was assembled under 900 MPa pressure to ensure intimate interface contact between the electrolyte and the electrode.[67] The ASSB was cycled below 3 V to avoid redox reactions of the Na₂(B₁₂H₁₂)₀.₅(B₁₀H₁₀)₀.₅ SSE. When the current density changed from C/20 to C/5, only negligible capacity loss was observed, suggesting the excellent rate performance of this ASSB. In long term cycling, this ASSB presented excellent reversible capacity ≈80 mA h g⁻¹ at C/5 (24 mA g⁻¹) with a capacity retention ratio of 85% at C/5 after 250 cycles. At present, although the performances of borohydride-based ASSBs still require big enhancements, the validity of borohydrides pairing with complex hydrides (such as MgH₂), Li₄Ti₅O₁₂, TiS₂, coated oxides, bare sulfur, organic electrodes, etc., has been well confirmed, which sheds light on their future practical applicability for all-solid-state batteries.

## 4. Performance Optimization of Borohydride-Based Solid-State Batteries

Improving the ionic conductivity of borohydride SSEs has been a priority research focus in the past several decades, with the production of a series of RT stabilized superionic-conductive borohydrides and the achievement of an understanding of the basic structural and chemical features required for high ionic conductivity. Thanks to the development of superionic-conductive borohydrides that can operate at low temperature, nowadays, all-solid-state batteries with borohydride SSEs have been successfully fabricated and cycled at a much-reduced temperature. Unlike some NASICON-, perovskite-, and garnet-type oxides facing difficulties in pellet pressing and sintering, ductile borohydrides do not suffer from similar problems. For the good operation of ASSBs with borohydride SSEs, three key issues usually govern their performances: i) ionic transport kinetics (ionic conductivity), ii) compatibility between the electrode materials and the borohydride SSEs, and iii) electrochemical stability of both the borohydride SSE and the interface layer.

Given the available superionic conductivity of borohydride SSEs, maximizing the ionic conductivity is no longer the dominant consideration for the development of borohydride-based ASSBs, and the challenges have shifted toward cell integration, which is correlated with issues of how to preserve both the electrochemical and the mechanical stability of electrodes and SSEs. Understanding these two issues and overcoming the integration restraints of ASSBs are essential to fully realize the potential of borohydride SSEs. To the best of our knowledge, there has been no systematic

study nor any insight into these two issues in the system of borohydride-based ASSBs. Thus, in this section, the optimization of borohydride-based ASSBs was selected as a research subject. We believe that, with the imminent development of borohydride SSEs, valuable perspectives on this subject will be transferred from the edge of research to the mainstream. Several approaches to the chemical amelioration of battery integration and typical designs of battery shells, etc. have been presented within previous research for optimizing the performance of all-solid-state batteries. The former will involve the selection of a compatible cathode, precise evaluation of available electrochemical windows, the manipulation of interface stability, and achieving intimate contact at the electrode–electrolyte interface. The optimization of borohydride-based ASSBs is expected to be energized through advances and experience by analogy with preliminary investigations of other SSEs.

4.1. Selection of Compatible Cathodes to Optimize Borohydride-Based ASSBs

Borohydride SSEs with reductive stability are well matched with an alkaline-metal anode (e.g., lithium negative electrode), however, they might react with oxidative cathode materials, leading to a detrimental loss of the cathode material and fading performance of ASSBs. For example, a LiCoO₂ cathode paired with a LiBH₄ SSE was found to irreversibly decompose after 30 cycles. New peaks in the Raman spectra ascribed to Co₃O₄ and CoO(OH) were observed, accompanied by reduced peak intensities of LiCoO₂. This demonstrated that LiBH₄ easily reacted with charged-state Li₁₋ₓCoO₂.[88] The estimated reaction might follow the route below[88]

$$Li_{0.5}CoO_2 + 1/8LiBH_4 \rightarrow 1/4Co_3O_4 + 1/4CoO(OH)$$
$$+ 1/8LiBO_2 + 1/4Li_2O + 1/8H_2 \tag{6}$$
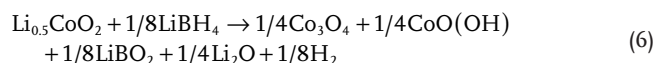
In comparison with the initial resistance of around 400 Ω, the interface resistance increased to ≈10⁴ Ω after 30 cycles, which was accompanied by the detrimental decomposition of LiCoO₂. To avoid side reactions originating from mismatched cathodes with borohydride SSEs, a convenient evaluation method is needed, either theoretical or experimental, and proper selection criteria are highly desirable to screen compatible electrode/electrolyte pairs.

Recently, Ceder and co-workers reported some insightful research, noting general trends in many ASSB systems and putting forward an effective methodology for the selection of compatible components.[4,9] By drawing on this methodology, probing the compatibility of different electrode/borohydride pairs and investigation of the practical utilization of borohydride SSEs can possibly be conducted in-depth. The methodology is based on calculation of thermodynamic forces,[9] which play important roles in determining the interface reaction energies and enable more visible observation of the interface stability so that interface reaction energies can be used as indicators to predict the reactions between the electrode materials and SSEs. The calculated results suggest that LiBH₄ was more stable against LiTiS₂, Li₂S, and LiVS₂ electrodes in comparison with other high-voltage oxide electrodes, such as LiCoO₂, LiFePO₄, LiMnO₂, and LiNiO₂ (**Figure 9**a). In addition, the study showed

**ADVANCED
SCIENCE NEWS**

www.advancedsciencenews.com

**ADVANCED
MATERIALS**

www.advmat.de
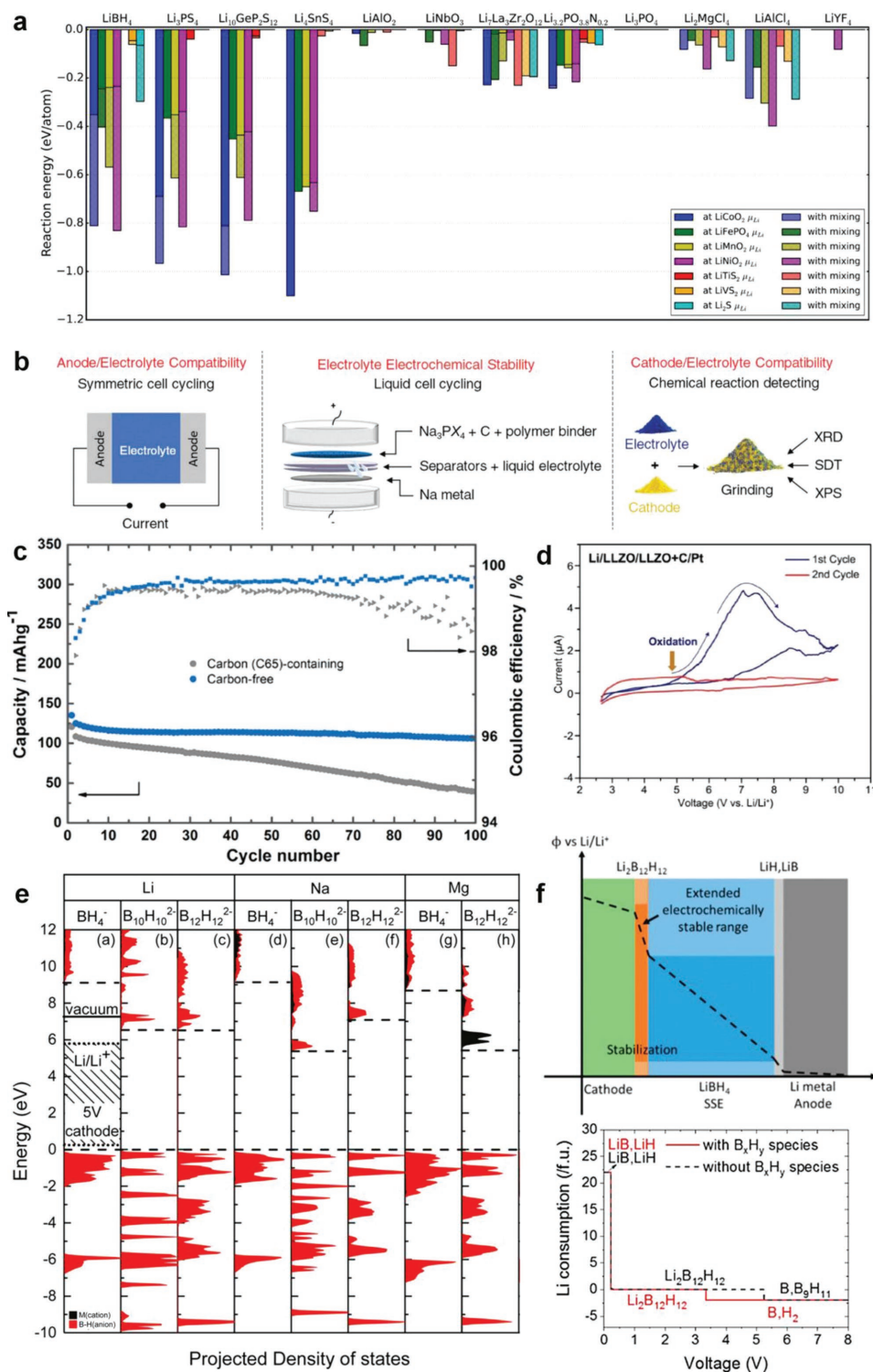
Figure 9. a) Calculated reaction energies at electrode/electrolyte interfaces at μ_{Li}, referring to the average cathode voltage. Energies are shown both for the energy of delithiation only (no mixing) and for the energy of cathode/electrolyte mixing open to lithium. Cathode/electrolyte pairs with reaction energies close to zero are supposed to possess stable interfaces. b) Summary of the compatibility and stability issues in ASSBs, and the experimental strategies to address these by taking the sodium system as an example. c) Long-term cycling performances and Coulombic efficiencies of ASSB (In/LGPS/LCO) with 5.7 wt% C65 additive and a comparable carbon-free ASSB. d) Cyclic voltammetry curves for the first two cycles of a Li/LLZO/LLZO+C cell within the voltage range of 2.6–10.0 V, where LLZO refers to $Li_7La_3Zr_2O_{12}$. e) Calculated density of states of M (M = Li, Na, Mg, and Ca) with borohydride anion species in the relevant stable/metastable phases. All the energies are with reference to the corresponding Fermi level of the borohydride. The valence band maximums (VBMs) and conduction band minimums (CBMs) are represented by dashed lines. f) Schematic illustration of decomposition

**ADVANCED
SCIENCE NEWS**

www.advancedsciencenews.com

**ADVANCED
MATERIALS**

www.advmat.de

that the Li_3PO_4 phase displayed good electrochemical stability when in contact with $LiCoO_2$, $LiFePO_4$, $LiMnO_2$, and $LiNiO_2$. This rationally explained why, in a previous study,[87] a Li_3PO_4 intermediate layer is more superior to Al_2O_3 and $LiNbO_3$ as a protective layer between a $LiCoO_2$ cathode and a $LiBH_4$ SSE.

Ceder et al. further examined the compatibility issues by taking the Na solid-state system as an example, according to the combined evidence of DFT calculations and experimental inspection (Figure 9b).[4] First, the reaction energies of the pristine cathode ($NaMO_2$, M = Cr, Mn, Fe, Co, and Ni) and SSE (Na_3PX_4, X = S, Se) pairs were computed to estimate the chemical stability at the interfaces of the pairs. Further repeated calculations were conducted to predict the equally important charge-state chemical stability involving the combinations of partially desodiated $Na_{0.5}MO_2$–electrolyte (Na_3PX_4, X = S, Se) pairs. The onset reaction temperature with SSEs decreased gradually from $NaCrO_2$ to $NaNiO_2$, accompanied by increased reaction driving forces, suggesting that $NaNiO_2$ had the lowest reaction barrier. This general trend was also confirmed by experimental results, which assessed the possible reactions on the basis of the combined results of simultaneous differential scanning calorimetry, thermogravimetric analysis (TGA), and XRD. The onset reaction temperature of $NaMO_2$–Na_3PS_4 combinations fell from $NaCrO_2$ (773 K) to $NaNiO_2$ (303 K), and that of $NaMO_2$–Na_3PSe_4 pairs decreased from $NaCrO_2$ (653 K) to $NaNiO_2$ (298 K), indicating that Na_3PS_4 featured higher chemical stability than Na_3PSe_4. Through this analysis, the chemical stability could be well evaluated. For example, the combination of $NaCrO_2$ and Na_3PSe_4 was free of chemical reactions at 573 K, and the pair could be used as available components for ASSBs at room temperature. Above 773 K, $NaCrO_2$ and Na_3PSe_4 would react with each other, with the observed product being $NaCrSe_2$.

To test the compatibility between charged-state Na_xMO_2 ($x < 1.0$) cathodes and Na_3PX_4 SSEs, first, chemically desodiated $NaMO_2$ (M = Cr, Fe, Co, and Ni) cathodes were prepared using a highly concentrated iodine solution in acetonitrile, a method equivalent to the desodiation of $NaMO_2$ near 3.7 V.[89] $NaMnO_2$ was not considered due to Mn extraction by acetonitrile solvent. The obtained products were verified by XRD as $Na_{0.5}CrO_2$, $Na_{0.5}FeO_2$ +β-$NaFeO_2$, $Na_{0.5}CoO_2$, and $Na_{0.5}NiO_2$ + $Na_{0.4}NiO_2$, respectively, and x of Na_xMO_2 was calculated according to the refined lattice parameters and electrochemical capacity. The experimental results suggested that $Na_{0.5}CrO_2$ was the most stable desodiated compound among all investigated desodiated $NaMO_2$ (M = Cr, Fe, Co, and Ni) cathodes in combination with Na_3PX_4 at RT. Other desodiated intermediates were found to react with SSEs directly, and sparks were even observed upon mixing desodiated $NaNiO_2$ with Na_3PX_4 in a Ar-filled glove box.

This methodology utilizing both theoretical computations and simple experimental tools such as XRD and TGA characterizations was promising and reliable for the assessment of the interfacial reactions between SSEs and electrodes. In the near future, a multidimensional evaluation system with predictive modeling may be established for borohydride SSEs,

by screening through all promising cathode materials and calculating the reaction energies between the cathode and borohydride SSEs, as well as for the repeated chemical reactions between charge/discharge-state products and borohydride SSEs. A better understanding of the thermodynamics and kinetics interplay of borohydride SSEs in the operation of solid-state batteries will be approached by visible observation of the reactions between electrolyte/electrode pairs using more in operando characterization techniques. We believe that the long-term cycling stability can be greatly ameliorated by using the most stable combinations and that we can further realize the performance optimization of borohydride-based ASSBs.

4.2. Precise Evaluation of the Available Electrochemical Windows to Optimize Borohydride SSEs for ASSBs

Electrochemical windows reflecting the electrochemical stability limits of SSEs determine the proper functioning of SSEs in solid-state batteries.[90] For a long time, the decomposition of SSEs has rarely been considered as the origin of the fading performance of ASSBs. Recently, calculations suggested that some thiophosphates with high ionic conductivity actually have narrower electrochemical windows than that measured by cyclic voltammetry.[9,91] In addition, more experimental proof has challenged the claimed electrochemical stability of SSEs and suggested that electrochemical windows may be overestimated by conventional methods.[9,18,92] In this section, we mainly focus on more precise determination of the electrochemical windows of borohydride SSEs, within which the irreversible degradation of borohydrides will be suppressed, thus contributing to the performance optimization of borohydride-based ASSBs.

The conventional cyclic voltammetry technique merely utilizes a simple inert metal/SSE/alkali-metal semiblocking electrode,[9] and the limitations may come due to the following reasons. First, the small contact area between the inert metal and the SSE results in slow kinetics of the SSE decomposition, and the degradation current may be too small to be captured by the semiblocking electrode. Second, the semiblocking electrode is different from a real ASSB configuration, where more homogeneously mixed carbon/cathode/electrolyte composites not only possess larger contact areas, but also efficient electron-transfer pathways.[18] Furthermore, carbon additives are reported to accelerate the decomposition of SSEs, curtailing the cycle life of ASSBs (Figure 9c), so the additional influences of carbon additives on the electrochemical stability of SSEs should not be ignored.[10] Zhang et al. observed larger interfacial resistance and faster capacity fading using a carbon-incorporated cathode composite than a carbon-free cathode composite, although the introduction of carbon commonly contributes to high power densities through a more homogeneous current distribution.[10] Ex situ X-ray photoelectron spectroscopy (XPS) analysis demonstrated that carbon

---

products of $Li_2B_{12}H_{12}$ at different voltages versus Li^+/Li. a) Reproduced with permission.[9] Copyright 2016, American Chemical Society. b) Reproduced with permission.[4] Copyright 2017, Royal Society of Chemistry. c) Reproduced with permission.[10] Copyright 2017, American Chemical Society. d) Reproduced with permission.[18] Copyright 2016, Wiley-VCH. e,f) Reproduced with permission.[76] Copyright 2017, American Chemical Society.

Table 2. Electrochemical stability tested by conventional cyclic voltammetry.

Borohydride SSE	Battery configuration	Electrochemical windows by CV	T [K]	Ref.
$Na(BH_4)_{0.5}(NH_2)_{0.5}$	$Mo/Na(BH_4)_{0.5}(NH_2)_{0.5}/Na$	−1 to 6 V	333 K	[19c]
$(100 - x)(0.75Li_2S \cdot 0.25P_2S_5) \cdot xLiBH_4$	Stainless steel/$(100 - x)(0.75Li_2S \cdot 0.25P_2S_5) \cdot xLiBH_4$/Li	−0.1 to 5 V	–	[37]
$LiBH_4$–$LiCl$	$Mo/LiBH_4$–$LiCl$/Li	−0.5 to 5 V	373 K	[86]
$Na_3BH_4B_{12}H_{12}$	$Au/Na_3BH_4B_{12}H_{12}/Na$	0–10 V	293 K	[58]

accelerates the electrochemical decomposition of $Li_{10}GeP_2S_{12}$. Inactive decomposition products such as S, S_8, and long-chain polysulfide species were observed on the interface layer, which blocked the Li^+-migration paths in solid-state batteries and explained the fading performance after the addition of carbon. Han et al. introduced an SSE-carbon/SSE/alkali metal solid-state cell to replace the simple inert metal/SSE/alkali-metal semiblocking electrode (Figure 9d). The former cell could mimic the components in practical ASSBs, and was anticipated to approach the intrinsic electrochemical windows of SSEs in the operation of ASSBs.[18] In the case of borohydride SSEs, as seen in **Table 2**, most of the previously reported electrochemical windows of borohydride SSEs span over 0–5 V based on the conventional CV method using inert metal/SSE/alkali metal semiblocking electrodes, and these properties may need to be reevaluated.[19b,25a,37,58,86] Theoretical predictions have also emerged in parallel with the development of experimental testing. Lu and Ciucci conducted a first-principles study on the electrochemical stability of metal borohydrides (Figure 9e).[76] An upper bound of the electrochemical window was assessed by calculating the bandgaps of the metal borohydrides, and a lower bound of the electrochemical window was evaluated according to the constructed grand-potential phase diagrams of metal borohydrides.[18,76,93] The bandgaps of all materials Li(BH_4^-, $B_{10}H_{10}^{2-}$, and $B_{12}H_{12}^{2-}$), Na(BH_4^-, $B_{10}H_{10}^{2-}$, and $B_{12}H_{12}^{2-}$) and Mg(BH_4^- and $B_{12}H_{12}^{2-}$) were measured to be larger than 5 eV, based on density-of-state calculations using the modified Becke–Johnson meta-generalized gradient approximation (mBJ meta-GGA) function, which indicated wide electrochemical windows of all materials against the inert electrodes. This still suggested the possible oxidization of $LiBH_4$, however. The grand-potential phase diagrams, which were previously used to estimate the electrochemical stability of several oxide and sulfide SSEs,[93] suggested that both $NaBH_4$ and $LiBH_4$ possessed electrochemical windows of ≈2 V versus Li/Li^+ and that the values were much narrower than experimentally reported. This may stem from a protective mechanism: the BH_4^--containing SSE in direct contact with the cathode could initially react with it, and the corresponding $B_{12}H_{12}^{2-}$-containing products with wider electrochemical windows can behave as protective interfacial layers, leading to wide electrochemical windows of ≈5 V (Figure 9f).

At present, how to measure the exact electrochemical windows of borohydrides is still being disputed. After a decade of research efforts that have contributed to superionic conductivity, the problem of identifying the precise electrochemical windows of borohydrides should not be ignored. Meanwhile, the development of suitable cell components, as well as proper additives, is critical for the fabrication of solid-state batteries with high power density and long cycle life.

4.3. Manipulation of Interface Stability and Intimate Contact to Optimize Borohydride-Based ASSBs

The chemical stability of the cathode/borohydride SSE interface is among the decisive factors affecting the electrochemical performances of borohydride-based SSEs, because reactions initially occur at the interfaces between the electrode and the SSE, and the resultant high interfacial resistance could degrade the power capabilities of batteries. In this section, we will mainly focus on the performance optimization of borohydride-based ASSBs through enhancing the interface stability and intimate contact at the electrode/SSE interface. Xiao and co-workers investigated the interface stability of some representative SSEs,[5b] leading to some inspiring ideas that could be used for borohydride SSEs. During the operation of borohydride-based ASSBs, the formation of a detrimental interphase layer,[94] lattice mismatch,[95] and insufficient contact among triple phases (electrode, conductive additive, and SSE)[6] may play important roles in generating high interfacial resistance. Here, we show the current strategies to mitigate these problems, with the expectation of improving the interface stability and further optimizing the performance of borohydride-based ASSBs. For oxide cathode/borohydride SSE pairs, borohydride SSEs are often assumed to be unstable at high potentials, with the consequent formation of an intermediate layer. An intermediate layer is not always detrimental. When the intermediate layer is a passivating layer with high ionic conductivity, it will prevent further reaction between the electrode and the SSE, and enable good cycling stability of ASSBs.[81] Unemoto et al. discovered that an intermediate layer of amorphous $Li_2B_{12}H_{12}$ was formed between TiS_2 electrode and $LiBH_4$ SSE in bulk-type all-solid-state lithium batteries.[81] The battery delivered a retained capacity of 180 mA h g⁻¹ (equivalent to 75.3% TiS_2 utilization) and nearly 100% Coulombic efficiency after 300 cycles. With ionic conductivity of $10^{-4.4}$ S cm⁻¹ and higher oxidative stability than $LiBH_4$, $Li_2B_{12}H_{12}$ can act as a stable intermediate layer that enables numerous discharge–charge cycles. When inactive decomposition products are formed at the cathode/borohydride interface, increased interfacial resistance will be generated after repeated cycles and obstruct the conduction of electrons and/or Li ions in the cathode. In contrast to this, the $LiCoO_2$/$LiBH_4$ interface deteriorated quickly, with an initial resistance around 400 Ω, and a greatly elevated interface resistance, ≈10^4 Ω after 30 cycles, accompanied by the detrimental decomposition of $LiCoO_2$. This is similar to the case of oxide electrolytes. Yamamoto et al. observed the formation of huge resistance when conducting a dynamic investigation of the electrical potential distribution at the $LiCoO_2$/$Li_{1+x+y}Al_yTi_{2-y}Si_xP_{3-x}O_{12}$ (LCO/LATSPO) interface in the charge–discharge process.[96] In the inner SSE, a gradual change in the electrical potential was

ADVANCED
SCIENCE NEWS
www.advancedsciencenews.com

ADVANCED
MATERIALS
www.advmat.de

observed, and a sharp potential drop was observed near the interface, suggesting that the resistance was mainly contributed by the area near the interface. An artificial buffer layer is commonly used to suppress this detrimental high resistance. Buffer layers of $LiNbO_3$, $Li_4Ti_5O_{12}$, $LiTaO_3$, Li_2SiO_3, etc., inserted between the oxide electrode ($LiCoO_2$, $LiMn_2O_4$) and the oxide/sulfide SSE were proven to be effective for significantly reducing the interfacial resistance.[7b,94,97] Improvement mechanisms utilizing buffer layers are different depending on the nature of the different electrode/SSE pairs, and they can act as key components for the elimination of the space-charge layer, suppression of mutual diffusion, or prevention of chemical reactions between the electrode and the SSE. Detrimental mutual diffusion or space-charge layers have not been reported in borohydride SSEs, and a buffer layer with high ionic conductivity will mainly act to prevent direct contact between borohydrides and cathodes.[98] Takahashi et al. investigated the effects of three types of intermediate layers: Li_3PO_4, $LiNbO_3$, and Al_2O_3 on the interfacial resistance of borohydride-based ASSBs. The intermediate layers were anchored between the $LiCoO_2$ electrode and the $LiBH_4$ SSE by pulsed laser deposition (PLD).[87] The calculated ionic conductivity of the Al_2O_3 layer was around 10^{-10} S cm^{-1}.[99] A nonporous ultrathin Al_2O_3 layer (approximately several nanometers) may restrict the interfacial resistance to a suitable value around 300 Ω, since the interfacial resistance decreased linearly with the reduced thickness of Al_2O_3 intermediate layer. With a 5 or 15 nm thick $LiNbO_3$ intermediate layer, the capacity faded quickly. For an ASSB with a 15 nm thick $LiNbO_3$ intermediate layer, the interfacial resistance increased from ≈250 Ω (1st cycle) to 800 Ω (30th cycle). When the thickness was increased to 40 or 130 nm, the batteries showed greatly stabilized cycling, with capacity maintained at 95% at the 30th cycle. A comparison of Raman spectra showed that peaks corresponding to Co_3O_4 and $CoO(OH)$ (≈800 cm^{-1}) emerged in the battery with a 15 nm thick $LiNbO_3$ layer, while no particular change took place in the spectra before and after cycling with the 40 nm thick $LiNbO_3$. 25 nm thick Li_3PO_4 layers appeared to be the most favorable intermediate layers among the three types of buffer materials, and the battery exhibited a 3 orders of magnitude reduction of interfacial resistance (21 Ω) compared to the battery without a Li_3PO_4 intermediate layer. The battery with 25 nm thick Li_3PO_4 maintained 97% of its capacity at the 30th cycle. Thus, based on the above analysis, an appropriate buffer layer between the cathode and borohydride SSE makes it possible to enhance the reversibility and durability of borohydride-based ASSBs. At present, there have been few reports on effective buffer layers for borohydride SSEs, and future research to develop novel buffer materials is necessary for the development of borohydride-based ASSBs. Lattice mismatches, which involve mismatches between grain boundaries or at the SSE/electrode interface, represent structural and chemical deviation in SSE pellets, and often emerge among electrode materials with lithiation-induced volume changes.[5b] Lattice mismatches often give rise to reduced ionic conductivity of borohydride SSEs, typical structural discontinuity, interrupted Li^+-conduction pathways, and increased grain-boundary resistance. To suppress lattice mismatch, approaches such as the incorporation of ductile components, adjustment of cell structures, and grain refinement are

effective to mitigate the small volume change (<10%) in most intercalation electrodes.[5b]

In addition, applying external working pressures, using a solution-processable cathode slurry, and polymer additives can contribute to ensuring sufficient contact and good interfacial connection between the borohydride SSE and the electrode (**Figure 10**a,c–e,g).[6,86,100] Remhof and co-workers proved the better cycling performance of ASSBs using $NaCrO_2$–$Na_2(B_{12}H_{12})_{0.5}(B_{10}H_{10})_{0.5}$–super-P composites in a solution-processable way (impregnated cathode) rather than simply mixing these composites (mixed cathode).[67] As observed by SEM (Figure 10f,h), only a few cracks were observed in the pellets of impregnated cathodes, while many cracks over 1 µm in length were observed in the mixed cathodes. The ASSB with the impregnated $NaCrO_2$–$Na_2(B_{12}H_{12})_{0.5}(B_{10}H_{10})_{0.5}$–super-P cathode presented 94.6% capacity retention after 20 cycles at C/20, while the ASSB with the mixed cathode showed a lower retained capacity after 20 cycles, equivalent to 15.8% of the initial capacity (Figure 10i). In addition, the resistance of the ASSB with the impregnated cathode increased from 50 to 125 Ω after 10 cycles, while the resistance increased from 100 to 1000 Ω using the mixed cathode, indicating the intimate ionic contact between the impregnated cathode and the SSE. Jung and co-workers assembled an ASSB using a solution-processable $NaCrO_2$ cathode, and a reduced resistance (600 Ω) was observed using solution-processable cathode in comparison with 30 000 Ω when utilizing a conventional mixed electrode.[101] The battery with the solution-processable $NaCrO_2$ cathode presented an initial discharge capacity of 108 mA h g^{-1}, which reached the performance of a battery containing a liquid electrolyte.

As discussed above, by manipulation of the interface stability and intimate contact between the electrode and the borohydride SSE, the performance and cycling stability of ASSBs can be remarkably enhanced.

4.4. Ameliorating Battery Designs to Optimize Borohydride-Based ASSBs

Special solid-state battery designs are beneficial to meet a high working pressure and guarantee intimate interfacial contact between the SSE and the electrode during electrochemical reactions. Figure 10b shows a useful solid-state cell design allowing high dwell pressure. In some work, the advanced engineering polymer polyetheretherketone (PEEK) was utilized as the battery shell material because it is superior in hardness, insulating property, high tensile strength, and good self-lubricating property in comparison with poly(tetrafluoroethylene) (PTFE).[86,102] A powerful battery device is fundamental yet significant for optimizing the electrochemical performance of borohydride-based ASSBs and the subsequent systematic investigations of intrinsic electrochemical behaviors of battery components.

5. Summary and Perspective

All-solid-state batteries based on borohydride solid-state electrolytes have experienced rapid progress and aroused increasing interest owing to their potential safety and other benefits for
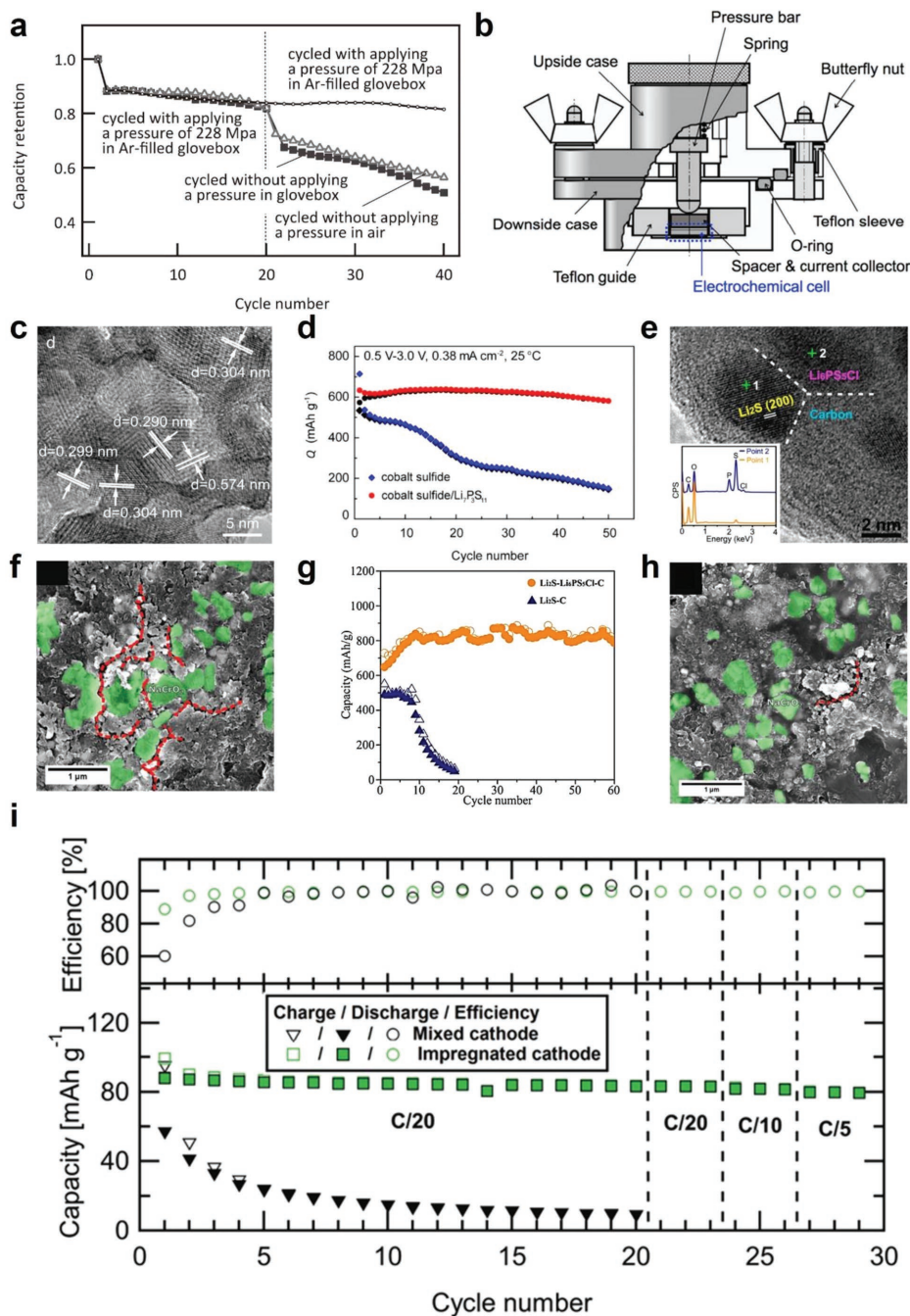
Figure 10. a) Comparison of the capacity retention at 0.88 mA g^{-1} for two TiS$_2$/Li$_{10}$GeP$_2$S$_{12}$/In-Li ASSBs operated under pressure of 230 MPa and without applying pressure in a glove box. b) Schematic illustration of battery device for cycling at high pressure. c) High-resolution transmission electron microscopy (TEM) image of cobalt sulfide–Li$_7$P$_3$S$_{11}$ nanocomposite. Clear lattices with interplanar distances of 0.299, 0.574 nm and 0.290, 0.304 nm match well with the d_{311}, d_{111} and d_{1-33}, d_{2-1-1} spacings of cobalt sulfide and Li$_7$P$_3$S$_{11}$ electrolyte, respectively. d) Long-term cycling performances at a constant current density of 0.38 mA cm^{-2} for two ASSBs containing the CoS$_2$–Li$_7$P$_3$S$_{11}$ nanocomposite electrode and the CoS$_2$ nanosheet electrode. e) High-resolution TEM image of the Li$_2$S–Li$_6$PS$_5$Cl–C nanocomposite, with the inset showing the energy-dispersive spectroscopy results at point 1 and point 2, respectively. f) SEM images of the mixed Na$_2$(B$_{12}$H$_{12}$)$_{0.5}$(B$_{10}$H$_{10}$)$_{0.5}$–NaCrO$_2$ electrode after pressing into a pellet. The green areas and red lines represent cathode particles and cracks, respectively. g) Long-term cycling performances of two ASSBs containing Li$_2$S–C and Li$_2$S–Li$_6$PS$_5$Cl–C nanocomposite electrodes at 50 mA g^{-1}. h) SEM images of the impregnated Na$_2$(B$_{12}$H$_{12}$)$_{0.5}$(B$_{10}$H$_{10}$)$_{0.5}$–NaCrO$_2$ electrode after pressing into a pellet. The green areas and red lines represent cathode particles and cracks, respectively. i) Comparison of cycling stability and Coulombic efficiency for ASSBs with the mixed Na$_2$(B$_{12}$H$_{12}$)$_{0.5}$(B$_{10}$H$_{10}$)$_{0.5}$–NaCrO$_2$ electrode and the impregnated Na$_2$(B$_{12}$H$_{12}$)$_{0.5}$(B$_{10}$H$_{10}$)$_{0.5}$–NaCrO$_2$ electrode, respectively. a) Reproduced with permission.[34c] Copyright 2016, Japan Society of Powder and Powder Metallurgy. b) Reproduced with permission.[86] Copyright 2015, IOP Publishing Ltd. c,d) Reproduced with permission.[100b] Copyright 2016, American Chemical Society. e,g) Reproduced with permission.[100a] Copyright 2016, American Chemical Society. f,h,i) Reproduced with permission.[67] Copyright 2017, Royal Society of Chemistry.

**ADVANCED
SCIENCE NEWS**

www.advancedsciencenews.com

**ADVANCED
MATERIALS**

www.advmat.de

high-performance batteries; nevertheless, at present, investigations and knowledge on the fundamentals of borohydride-based ASSBs, especially from the aspects of correlated interfacial behavior, available electrochemical stability, and cell components and architectures, are still limited. To unlock the energy capabilities of borohydride-based ASSBs, some perspectives are provided based on their current research status.

a) Theoretical prediction and design of high-ionic-conductivity borohydride SSEs with novel structure.

Designing novel borohydride derivative SSEs could be guided by high-throughput calculations and big-data predictions based on suitable models and metrics, with careful consideration of electrochemistry/oxidation stability, ionic conductivity, electronic insulation, cost, etc., since freezing the high ionic conductivity at low temperature is still a prerequisite to improve the applicability of borohydride SSEs. Some members of the borohydride SSE family, such as the carborane series, have exhibited remarkably high ionic conductivities, as well as oxidation stability and chemical inertness towards aggressive reagents. For the convenience of experimentalists and further development of borohydride solid-state electrolytes, it is necessary to tabulate the thermal/electrochemical stability and possible decomposition products for a wide range of high-performance combinations of borohydride solid-state electrolytes, intermediate layers, additives, and compatible electrode materials.

In the meantime, the synthesis of borohydride derivatives still needs further efforts from experimentalists. Obtaining novel hybrid borohydride SSEs through smart methods appears to be an interesting prospect. The pertinent methods to fabricate bulk/thin-film/hierarchical nanostructured borohydride SSEs may include sputtering and atomic-layer deposition, self- and field-induced assembly of molecules, polymers, and solution-phase layer-by-layer deposition methods.

b) Optimization of the interfacial kinetics of borohydride-based ASSBs.

The electron- and ion-transfer processes, cycling performances, and polarization phenomenon in borohydride-based ASSBs greatly depend on the interfacial kinetics between the electrodes and the borohydride SSEs. To overcome the sluggish interfacial kinetics of borohydride-based ASSBs, compatible electrode/borohydride SSE pairs should be chosen first, and at the same time, future research should pay more attention to developing high-quality intermediate layers that possess good ionic conductivity and are compatible with both the electrode side and borohydride SSE side. Volume changes in anode materials during continuous plating/stripping often induce poor physical contact between solids, and thus, more techniques to maintain intimate contact between the electrode and the borohydride SSE are essential. Approaches such as nanotechnology, external mechanical pressure, preloading Li metal into a stable host, and inserting a soft polymer interlayer between the solid components may clarify such problematic issues. To date, the interfacial control of borohydride-based ASSBs is still at an early stage, which requires interdisciplinary knowledge of the properties involving electrode materials, borohydride SSEs, and conductive additives. More in operando characterization

techniques will be useful to precisely evaluate these fundamental aspects and provide solutions to these existing problems and challenges.

c) Enhancing the practical applicability of borohydride SSEs for commercializing affordable ASSBs.

To further improve the capacity and energy density of borohydride-based ASSBs, increasing the loading mass of active materials in the cathode composites is the key objective, and this could be approached by hosting active phases in efficient electronic and ionic-conductive networks, which may depend on promising advanced nanotechnology and techniques.

Even though many issues are just beginning to be recognized, solutions are beginning to be researched, and ASSBs with smart electrode configurations and well-defined parameters are challenging. The rapid development of borohydride SSEs is inspiring, well worth further in-depth investigation, and it is of high scientific value to fully explore their potential for large-scale energy storage in ASSBs in the near future.

Acknowledgements

Conflict of Interest

The authors declare no conflict of interest.

Keywords

[1] a) R. J. Chen, W. J. Qu, X. Guo, L. Li, F. Wu, *Mater. Horiz.* **2016**, *3*, 487; b) J. M. Tarascon, M. Armand, *Nature* **2001**, *414*, 359; c) Q. W. Lu, Y. B. He, Q. P. Yu, B. H. Li, Y. V. Kaneti, Y. W. Yao, F. Y. Kang, Q. H. Yang, *Adv. Mater.* **2017**, *29*, 1604460; d) Y. S. Zhao, L. L. Daemen, *J. Am. Chem. Soc.* **2012**, *134*, 15042; e) A. Emly, E. Kioupakis, A. V. D. Ven, *Chem. Mater.* **2013**, *25*, 4663; f) J. C. Li, C. Ma, M. F. Chi, C. D. Liang, N. J. Dudney, *Adv. Energy Mater.* **2015**, *5*, 1401408; g) Y. Meesala, A. Jena, H. Chang, R. S. Liu, *ACS Energy Lett.* **2017**, *2*, 2734; h) Z. H. Gao, H. B. Sun, L. Fu, F. L. Ye, Y. Zhang, W. Luo, Y. H. Huang, *Adv. Mater.* **2018**, *30*, 1705702.

[2] a) B. K. Zhang, R. Tan, L. Y. Yang, J. X. Zheng, K. C. Zhang, S. J. Mo, Z. Lin, F. Pan, *Energy Storage Mater.* **2018**, *10*, 139; b) J. G. Kim, B. Son, S. Mukherjee, N. Schuppert, A. Bates,

**ADVANCED
SCIENCE NEWS**

www.advancedsciencenews.com

**ADVANCED
MATERIALS**

www.advmat.de

O. Kwon, M. J. Choi, H. Y. Chung, S. Park, *J. Power Sources* **2015**, *282*, 299; c) Y. J. Liu, P. He, H. S. Zhou, *Adv. Energy Mater.* **2018**, *8*, 1701602.

[3] a) D. C. Lin, Y. Y. Liu, Y. Cui, *Nat. Nanotechnol.* **2017**, *12*, 194; b) X. L. Wu, J. Zong, H. Xu, W. Wang, X. J. Liu, *RSC Adv.* **2016**, *6*, 57346; c) D. P. Lv, J. M. Zheng, Q. Y. Li, X. Xie, S. Ferrara, Z. M. Nie, L. B. Mehdi, N. D. Browning, J. G. Zhang, G. L. Graff, J. Liu, J. Xiao, *Adv. Energy Mater.* **2015**, *5*, 1402290; d) J. W. Choi, D. Aurbach, *Nat. Rev. Mater.* **2016**, *1*, 16013.

[4] Y. S. Tian, T. Shi, W. D. Richards, J. C. Li, J. C. Kim, S. H. Bo, G. Ceder, *Energy Environ. Sci.* **2017**, *10*, 1150.

[5] a) X. R. Lin, M. Salari, L. M. Arava, P. M. Ajayan, M. W. Grinstaff, *Chem. Soc. Rev.* **2016**, *45*, 5848; b) B. B. Wu, S. Y. Wang, W. J. E. Iv, D. Z. Deng, J. H. Yang, J. Xiao, *J. Mater. Chem. A* **2016**, *4*, 15266; c) S. H. Jiao, J. M. Zheng, Q. Y. Li, X. Li, M. H. Engelhard, R. G. Cao, J. G. Zhang, W. Xu, *Joule* **2018**, *2*, 110.

[6] H. Duan, Y. X. Yin, Y. Shi, P. F. Wang, X. D. Zhang, C. P. Yang, J. L. Shi, R. Wen, Y. G. Guo, L. J. Wan, *J. Am. Chem. Soc.* **2018**, *140*, 82.

[7] a) W. B. Zhang, D. A. Weber, H. Weigand, T. Arlt, I. Manke, D. Schröder, R. Koerver, T. Leichtweiss, P. Hartmann, W. G. Zeier, J. Janek, *ACS Appl. Mater. Interfaces* **2017**, *9*, 17835; b) N. Ohta, K. Takada, I. Sakaguchi, L. Q. Zhang, R. Z. Ma, K. Fukuda, M. Osada, T. Sasaki, *Electrochem. Commun.* **2007**, *9*, 1486.

[8] a) W. B. Zhang, D. Schröder, T. Arlt, I. Manke, R. Koerver, R. Pinedo, D. A. Weber, J. Sann, W. G. Zeier, J. Janek, *J. Mater. Chem. A* **2017**, *5*, 9929; b) J. M. Whiteley, J. W. Kim, C. S. Kang, J. S. Cho, K. H. Oh, S. H. Lee, *J. Electrochem. Soc.* **2015**, *162*, A711.

[9] W. D. Richards, L. J. Miara, Y. Wang, J. C. Kim, G. Ceder, *Chem. Mater.* **2016**, *28*, 266.

[10] W. B. Zhang, T. Leichtweiss, S. P. Culver, R. Koerver, D. Das, D. A. Weber, W. G. Zeier, J. Janek, *ACS Appl. Mater. Interfaces* **2017**, *9*, 35888.

[11] a) Y. Seino, T. Ota, K. Takada, A. Hayashi, M. Tatsumisago, *Energy Environ. Sci.* **2014**, *7*, 627; b) R. Murugan, V. Thangadurai, W. Weppner, *Angew. Chem., Int. Ed.* **2007**, *46*, 7778; c) T. Thompson, S. Yu, L. Williams, R. D. Schmidt, R. Garcia-Mendez, J. Wolfenstine, J. L. Allen, E. Kioupakis, D. J. Siegel, J. Sakamoto, *ACS Energy Lett.* **2017**, *2*, 462.

[12] a) K. Fu, Y. H. Gong, B. Y. Liu, Y. Z. Zhu, S. M. Xu, Y. G. Yao, W. Luo, C. W. Wang, S. D. Lacey, J. Q. Dai, Y. N. Chen, Y. F. Mo, E. Wachsman, L. B. Hu, *Sci. Adv.* **2017**, *3*, 1601659; b) C. Deviannapoorani, L. Dhivya, S. Ramakumar, R. Murugan, *J. Power Sources* **2013**, *240*, 18; c) Y. T. Li, J. T. Han, C. A. Wang, H. Xie, J. B. Goodenough, *J. Mater. Chem.* **2012**, *22*, 15357; d) J. C. Bachman, S. Muy, A. Grimaud, H. H. Chang, N. Pour, S. F. Lux, O. Paschos, F. Maglia, S. Lupart, P. Lamp, L. Giordano, Y. Shao-Horn, *Chem. Rev.* **2016**, *116*, 140.

[13] Y. X. Wang, P. F. Yan, J. Xiao, X. C. Lu, J. G. Zhang, V. L. Sprenkle, *Solid State Ionics* **2016**, *294*, 108.

[14] Y. Kato, S. Hori, T. Saito, K. Suzuki, M. Hirayama, A. Mitsui, M. Yonemura, H. Iba, R. Kanno, *Nat. Energy* **2016**, *1*, 16030.

[15] V. Thangadurai, S. Narayanan, D. Pinzaru, *Chem. Soc. Rev.* **2014**, *43*, 4714.

[16] a) A. Sakuda, A. Hayashi, M. Tatsumisago, *Sci. Rep.* **2013**, *3*, 2261; b) Y. S. Jung, D. Y. Oh, Y. J. Nam, K. H. Park, *Isr. J. Chem.* **2015**, *55*, 472; c) M. Kotobuki, H. Munakata, K. Kanamura, Y. Sato, T. Yoshida, *J. Electrochem. Soc.* **2010**, *157*, A1076.

[17] a) A. Kuhn, O. Gerbig, C. Zhu, F. Falkenberg, J. Maier, B. V. Lotsch, *Phys. Chem. Chem. Phys.* **2014**, *16*, 14669; b) P. Bron, S. Johansson, K. Zick, J. S. A. D. Gunne, S. Dehnen, B. Roling, *J. Am. Chem. Soc.* **2013**, *135*, 15694; c) J. M. Whiteley, J. H. Woo, E. Y. Hu, K. W. Nam, S. H. Lee, *J. Electrochem. Soc.* **2014**, *161*, A1812; d) N. Kamaya, K. Homma, Y. Yamakawa, M. Hirayama, R. Kanno, M. Yonemura,

T. Kamiyama, Y. Kato, S. Hama, K. Kawamoto, A. Mitsui, *Nat. Mater.* **2011**, *10*, 682; e) W. D. Richards, T. Tsujimura, L. J. Miara, Y. Wang, J. C. Kim, S. P. Ong, I. Uechi, N. Suzuki, G. Ceder, *Nat. Commun.* **2016**, *7*, 11009.

[18] F. D. Han, Y. Z. Zhu, X. F. He, Y. F. Mo, C. S. Wang, *Adv. Energy Mater.* **2016**, *6*, 1501590.

[19] a) P. Schouwink, M. B. Ley, A. Tissot, H. Hagemann, T. R. Jensen, L. Smrcok, R. Cerny, *Nat. Commun.* **2014**, *5*, 5706; b) M. Matsuo, S. I. Orimo, *Adv. Energy Mater.* **2011**, *1*, 161; c) M. Matsuo, S. Kuromoto, T. Sato, H. Oguchi, H. Takamura, S. I. Orimo, *Appl. Phys. Lett.* **2012**, *100*, 203904.

[20] A. Manthiram, X. W. Yu, S. F. Wang, *Nat. Rev. Mater.* **2017**, *2*, 16103.

[21] B. Boukamp, R. Huggins, *Phys. Lett. A* **1979**, *72*, 464.

[22] A. Unemoto, M. Matsuo, S. I. Orimo, *Adv. Funct. Mater.* **2014**, *24*, 2267.

[23] a) M. Matsuo, Y. Nakamori, S. I. Orimo, H. Maekawa, H. Takamura, *Appl. Phys. Lett.* **2007**, *91*, 224103; b) H. Maekawa, M. Matsuo, H. Takamura, M. Ando, Y. Noda, T. Karahashi, S. I. Orimo, *J. Am. Chem. Soc.* **2009**, *131*, 894.

[24] a) W. S. Tang, M. Matsuo, H. Wu, V. Stavila, W. Zhou, A. A. Talin, A. V. Soloninin, R. V. Skoryunov, O. A. Babanova, A. V. Skripov, A. Unemoto, S. I. Orimo, T. J. Udovic, *Adv. Energy Mater.* **2016**, *6*, 1502237; b) W. S. Tang, K. Yoshida, A. V. Soloninin, R. V. Skoryunov, O. A. Babanova, A. V. Skripov, M. Dimitrievska, V. Stavila, S. I. Orimo, T. J. Udovic, *ACS Energy Lett.* **2016**, *1*, 659.

[25] a) T. J. Udovic, M. Matsuo, W. S. Tang, H. Wu, V. Stavila, A. V. Soloninin, Roman V. Skoryunov, O. A. Babanova, A. V. Skripov, J. J. Rush, A. Unemoto, H. Takamura, S. I. Orimo, *Adv. Mater.* **2014**, *26*, 7622; b) A. Unemoto, S. Yasaku, G. Nogami, M. Tazawa, M. Taniguchi, M. Matsuo, T. Ikeshoji, S. I. Orimo, *Appl. Phys. Lett.* **2014**, *105*, 083901.

[26] a) V. Epp, M. Wilkening, *Phys. Rev. B* **2010**, *82*, 020301; b) J. S. G. Myrdal, D. Blanchard, D. Sveinbjörnsson, T. Vegge, *J. Phys. Chem. C* **2013**, *117*, 9084.

[27] P. C. Aeberhard, S. R. Williams, D. J. Evans, K. Refson, W. I. David, *Phys. Rev. Lett.* **2012**, *108*, 095901.

[28] T. Ikeshoji, E. Tsuchida, T. Morishita, K. Ikeda, M. Matsuo, Y. Kawazoe, S. I. Orimo, *Phys. Rev. B* **2011**, *83*, 144301.

[29] D. Sveinbjörnsson, J. S. G. Myrdal, D. Blanchard, J. J. Bentzen, T. Hirata, M. B. Mogensen, P. Norby, S. I. Orimo, T. Vegge, *J. Phys. Chem. C* **2013**, *117*, 3249.

[30] M. Matsuo, A. Remhof, P. Martelli, R. Caputo, M. Ernst, Y. Miura, T. Sato, H. Oguchi, H. Maekawa, H. Takamura, A. Borgschulte, A. Züttel, S. I. Orimo, *J. Am. Chem. Soc.* **2009**, *131*, 16389.

[31] Y. G. Yan, R. S. Kühnel, A. Remhof, L. Duchêne, E. C. Reyes, D. Rentsch, Z. Łodziana, C. Battaglia, *Adv. Energy Mater.* **2017**, *7*, 1700294.

[32] a) Y. E. Filinchuk, K. Yvon, G. P. Meisner, F. E. Pinkerton, M. P. Balogh, *Inorg. Chem.* **2006**, *45*, 1433; b) G. P. Meisner, M. L. Scullin, M. P. Balogh, F. E. Pinkerton, M. S. Meyer, *J. Phys. Chem. B* **2006**, *110*, 4186.

[33] Y. Wang, W. D. Richards, S. P. Ong, L. J. Miara, J. C. Kim, Y. F. Mo, G. Ceder, *Nat. Mater.* **2015**, *14*, 1026.

[34] a) K. Takada, T. Ohno, N. Ohta, T. Ohnishi, Y. Tanaka, *ACS Energy Lett.* **2017**, *3*, 98; b) N. F. Zheng, X. H. Bu, P. Feng, *Nature* **2003**, *426*, 428; c) W. J. Li, M. Hirayama, K. Suzuki, R. Kanno, *Mater. Trans.* **2016**, *57*, 549; d) M. Agostini, Y. Aihara, T. Yamada, B. Scrosati, J. Hassoun, *Solid State Ionics* **2013**, *244*, 48; e) M. Nagao, A. Hayashi, M. Tatsumisago, T. Ichinose, T. Ozaki, Y. Togawa, S. Mori, *J. Power Sources* **2015**, *274*, 471; f) M. H. Chen, S. Adams, *J. Solid State Electrochem.* **2015**, *19*, 697; g) M. Nagao, Y. Imade, H. Narisawa, T. Kobayashi, R. Watanabe, T. Yokoi, T. Tatsumi, R. Kanno, *J. Power Sources* **2013**, *222*, 237.

[35] M. Murayama, *J. Solid State Chem.* **2002**, *168*, 140.

[36] E. Rangasamy, G. Sahu, J. K. Keum, A. J. Rondinone, N. J. Dudney, C. D. Liang, *J. Mater. Chem. A* **2014**, *2*, 4111.

[37] A. Yamauchi, A. Sakuda, A. Hayashi, M. Tatsumisago, *J. Power Sources* **2013**, *244*, 707.

[38] A. Unemoto, H. Wu, T. J. Udovic, M. Matsuo, T. Ikeshoji, S. I. Orimo, *Chem. Commun.* **2016**, *52*, 564.

[39] T. J. Udovic, M. Matsuo, A. Unemoto, N. Verdal, V. Stavila, A. V. Skripov, J. J. Rush, H. Takamurag, S. I. Orimo, *Chem. Commun.* **2014**, *50*, 3750.

[40] a) M. B. Ley, S. Boulineau, R. Janot, Y. Filinchuk, T. R. Jensen, *J. Phys. Chem. C* **2012**, *116*, 21267; b) M. B. Ley, D. B. Ravnsbæk, Y. Filinchuk, Y. S. Lee, R. Janot, Y. W. Cho, J. Skibsted, T. R. Jensen, *Chem. Mater.* **2012**, *24*, 1654.

[41] M. Brighi, P. Schouwink, Y. Sadikin, R. Cerný, *J. Alloys Compd.* **2016**, *662*, 388.

[42] T. Mezaki, Y. Kuronuma, I. Oikawa, A. Kamegawa, H. Takamura, *Inorg. Chem.* **2016**, *55*, 10484.

[43] a) H. Takamura, Y. Kuronuma, H. Maekawa, M. Matsuo, S. I. Orimo, *Solid State Ionics* **2011**, *192*, 118; b) H. Yamawaki, H. Fujihisa, Y. Gotoh, S. Nakano, *J. Phys. Chem. Solids* **2015**, *76*, 40.

[44] D. Sveinbjörnsson, D. Blanchard, J. S. G. Myrdal, R. Younesi, R. Viskinde, M. D. Riktor, P. Norby, T. Vegge, *J. Solid State Chem.* **2014**, *211*, 81.

[45] H. Mehrer, *Diffusion in Solids: Fundamentals, Methods, Materials, Diffusion-Controlled Processes*, Springer, Berlin **2007**.

[46] S. Hull, *Rep. Prog. Phys.* **2004**, *67*, 1233.

[47] X. F. He, Y. Z. Zhu, Y. F. Mo, *Nat. Commun.* **2017**, *8*, 15893.

[48] D. Blanchard, A. Nale, D. Sveinbjörnsson, T. M. Eggenhuisen, M. H. W. Verkuijlen, Suwarno, T. Vegge, A. P. M. Kentgens, P. E. de Jongh, *Adv. Funct. Mater.* **2015**, *25*, 184.

[49] Y. S. Choi, Y. S. Lee, K. H. Oh, Y. W. Cho, *Phys. Chem. Chem. Phys.* **2016**, *18*, 22540.

[50] a) A. R. Polu, R. Kumar, H. W. Rhee, *High Perform. Polym.* **2014**, *26*, 628; b) A. R. Polu, R. Kumar, *Bull. Mater. Sci.* **2014**, *37*, 309.

[51] C. Gerbaldi, J. R. Nair, M. A. Kulandainathan, R. S. Kumar, C. Ferrara, P. Mustarelli, A. M. Stephan, *J. Mater. Chem. A* **2014**, *2*, 9948.

[52] Z. D. Hood, H. Wang, Y. C. Li, A. S. Pandian, M. P. Paranthaman, C. D. Liang, *Solid State Ionics* **2015**, *283*, 75.

[53] C. F. Yuan, J. Li, P. F. Han, Y. Q. Lai, Z. A. Zhang, J. Liu, *J. Power Sources* **2013**, *240*, 653.

[54] E. Quartarone, P. Mustarelli, *Chem. Soc. Rev.* **2011**, *40*, 2525.

[55] B. B. Wei, X. Wang, Y. F. Jiang, Y. Yang, *Bull. Chin. Ceram. Soc.* **2009**, *28*, 542.

[56] E. Kendrick, J. Kendrick, K. S. Knight, M. S. Islam, P. R. Slater, *Nat. Mater.* **2007**, *6*, 871.

[57] M. Matsuo, H. Oguchi, T. Sato, H. Takamura, E. Tsuchida, T. Ikeshoji, S. I. Orimo, *J. Alloys Compd.* **2013**, *580*, S98.

[58] Y. Sadikin, M. Brighi, P. Schouwink, R. Černý, *Adv. Energy Mater.* **2015**, *5*, 1501016.

[59] T. Ikeshoji, E. Tsuchida, S. Takagi, M. Matsuo, S. I. Orimo, *RSC Adv.* **2014**, *4*, 1366.

[60] E. Roedern, R. S. Kuhnel, A. Remhof, C. Battaglia, *Sci. Rep.* **2017**, *7*, 46189.

[61] S. Higashi, K. Miwa, M. Aoki, K. Takechi, *Chem. Commun.* **2014**, *50*, 1320.

[62] H. W. Li, E. Akiba, S. I. Orimo, *J. Alloys Compd.* **2013**, *580*, S292.

[63] a) J. A. Teprovich Jr., H. Colón-Mercado, A. L. Washington II, P. A. Ward, S. Greenway, D. M. Missimer, H. Hartman, J. Velten, J. H. Christiana, R. Zidan, *J. Mater. Chem. A* **2015**, *3*, 22853; b) I. A. Ellis, D. F. Gaines, R. Schaeffer, *J. Am. Chem. Soc.* **1963**, *85*, 3884; c) J. W. Johnson, J. F. Brody, *J. Electrochem. Soc.* **1982**, *129*, 2213.

[64] L. Q. He, H. W. Li, H. Nakajima, N. Tumanov, Y. Filinchuk, S. J. Hwang, M. Sharma, H. Hagemann, E. Akiba, *Chem. Mater.* **2015**, *27*, 5483.

[65] A. Unemoto, K. Yoshida, T. Ikeshoji, S. I. Orimo, *Mater. Trans.* **2016**, *57*, 1639.

[66] A. V. Skripov, O. A. Babanova, A. V. Soloninin, V. Stavila, N. Verdal, T. J. Udovic, J. J. Rush, *J. Phys. Chem. C* **2013**, *117*, 25961.

[67] L. Duchêne, R. S. Kühnel, E. Stilp, E. Cuervo-Reyes, A. Remhof, H. Hagemann, C. Battaglia, *Energy Environ. Sci.* **2017**, *10*, 2609.

[68] a) P. Kaszyński, B. Ringstrand, *Angew. Chem., Int. Ed.* **2015**, *54*, 6576; b) S. Körbe, P. J. Schreiber, J. Michl, *Chem. Rev.* **2006**, *106*, 5208.

[69] a) O. Tutusaus, R. Mohtadi, T. S. Arthur, F. Mizuno, E. G. Nelson, Y. V. Sevryugina, *Angew. Chem., Int. Ed.* **2015**, *54*, 7900; b) C. Douvris, J. Michl, *Chem. Rev.* **2013**, *113*, PR179.

[70] W. S. Tang, A. Unemoto, W. Zhou, V. Stavila, M. Matsuo, H. Wu, S. I. Orimo, T. J. Udovic, *Energy Environ. Sci.* **2015**, *8*, 3637.

[71] L. Zhang, K. Yang, J. L. Mi, L. Lu, L. R. Zhao, L. M. Wang, Y. M. Li, H. Zeng, *Adv. Energy Mater.* **2015**, *5*, 1501294.

[72] H. M. Zhao, J. Zhou, P. Jena, *Angew. Chem., Int. Ed.* **2016**, *55*, 3704.

[73] S. Giri, S. Behera, P. Jena, *Angew. Chem., Int. Ed. Engl.* **2014**, *53*, 13916.

[74] J. B. Varley, K. Kweon, P. Mehta, P. Shea, T. W. Heo, T. J. Udovic, V. Stavila, B. C. Wood, *ACS Energy Lett.* **2017**, *2*, 250.

[75] G. K. P. Dathar, J. Balachandran, P. R. C. Kent, A. J. Rondinonea, P. Ganesh, *J. Mater. Chem. A* **2017**, *5*, 1153.

[76] Z. H. Lu, F. Ciucci, *Chem. Mater.* **2017**, *29*, 9308.

[77] a) L. Zeng, K. Kawahito, S. Ikeda, T. Ichikawa, H. Miyaokad, Y. Kojima, *Chem. Commun.* **2015**, *51*, 9773; b) Y. Oumellal, A. Rougier, G. A. Nazri, J. M. Tarascon, L. Aymard, *Nat. Mater.* **2008**, *7*, 916; c) W. Zaïdi, Y. Oumellal, J. P. Bonnet, J. Zhang, F. Cuevas, M. Latroche, J. L. Bobet, L. Aymard, *J. Power Sources* **2011**, *196*, 2854; d) S. Brutti, G. Mulas, E. Piciollo, S. Panero, P. Reale, *J. Mater. Chem.* **2012**, *22*, 14531; e) Y. Oumellal, A. Rougier, J. M. Tarascon, L. Aymard, *J. Power Sources* **2009**, *192*, 698.

[78] S. Ikeda, T. Ichikawa, K. Kawahito, K. Hirabayashi, H. Miyaokac, Y. Kojima, *Chem. Commun.* **2013**, *49*, 7174.

[79] L. Zeng, T. Ichikawa, K. Kawahito, H. Miyaoka, Y. Kojima, *ACS Appl. Mater. Interfaces* **2017**, *9*, 2261.

[80] M. S. Whittingham, *Science* **1976**, *192*, 1126.

[81] A. Unemoto, T. Ikeshoji, S. Yasaku, M. Matsuo, V. Stavila, T. J. Udovic, S. I. Orimo, *Chem. Mater.* **2015**, *27*, 5407.

[82] T. Ohzuku, A. Ueda, N. Yamamoto, *J. Electrochem. Soc.* **1995**, *142*, 1431.

[83] D. Sveinbjörnsson, A. S. Christiansen, R. Viskinde, P. Norby, T. Vegge, *J. Electrochem. Soc.* **2014**, *161*, A1432.

[84] S. Sato, A. Unemoto, T. Ikeda, S. I. Orimo, H. Isobe, *Small* **2016**, *12*, 3381.

[85] S. Das, P. Ngene, P. Norby, T. Vegge, P. E. de Jongh, D. Blanchard, *J. Electrochem. Soc.* **2016**, *163*, A2029.

[86] A. Unemoto, C. L. Chen, Z. C. Wang, M. Matsuo, T. Ikeshoji, S. I. Orimo, *Nanotechnology* **2015**, *26*, 254001.

[87] K. Takahashi, H. Maekawa, H. Takamura, *Solid State Ionics* **2014**, *262*, 179.

[88] K. Takahashi, K. Hattori, T. Yamazaki, K. Takada, M. Matsuo, S. I. Orimo, H. Maekawa, H. Takamura, *J. Power Sources* **2013**, *226*, 61.

[89] A. R. Wizansky, P. E. Rauch, F. J. Disalvo, *J. Solid State Chem.* **1989**, *81*, 203.

[90] H. Y. Che, S. L. Chen, Y. Y. Xie, H. Wang, K. Amine, X. Z. Liao, Z. F. Ma, *Energy Environ. Sci.* **2017**, *10*, 1075.

[91] a) Y. Z. Zhu, X. F. He, Y. F. Mo, *J. Mater. Chem. A* **2016**, *4*, 3253; b) Y. Z. Zhu, X. F. He, Y. F. Mo, *ACS Appl. Mater. Interfaces* **2015**, *7*, 23685.

[92] a) F. D. Han, T. Gao, Y. J. Zhu, K. J. Gaskell, C. S. Wang, *Adv. Mater.* **2015**, *27*, 3473; b) A. Schwöbel, R. Hausbrand,

W. Jaegermann, *Solid State Ionics* **2015**, *273*, 51; c) L. Duchene, R. S. Kuhnel, D. Rentsch, A. Remhof, H. Hagemann, C. Battaglia, *Chem. Commun.* **2017**, *53*, 4195.

[93] S. P. Ong, Y. F. Mo, W. D. Richards, L. Miara, H. S. Lee, G. Ceder, *Energy Environ. Sci.* **2013**, *6*, 148.

[94] A. Sakuda, A. Hayashi, M. Tatsumisago, *Chem. Mater.* **2010**, *22*, 949.

[95] C. Ma, K. Chen, C. D. Liang, C. W. Nan, R. Ishikawa, K. More, M. F. Chi, *Energy Environ. Sci.* **2014**, *7*, 1638.

[96] K. Yamamoto, Y. Iriyama, T. Asaka, T. Hirayama, H. Fujita, C. A. Fisher, K. Nonaka, Y. Sugita, Z. Ogumi, *Angew. Chem., Int. Ed. Engl.* **2010**, *49*, 4414.

[97] a) N. Ohta, K. Takada, L. Q. Zhang, R. Z. Ma, M. Osada, T. Sasaki, *Adv. Mater.* **2006**, *18*, 2226; b) K. Takada, N. Ohta, L. Q. Zhang,

K. Fukuda, I. Sakaguchi, R. Ma, M. Osada, T. Sasaki, *Solid State Ionics* **2008**, *179*, 1333; c) A. Sakuda, H. Kitaura, A. Hayashi, K. Tadanaga, M. Tatsumisago, *J. Electrochem. Soc.* **2009**, *156*, A27.

[98] K. Takada, N. Ohta, L. Q. Zhang, X. X. Xu, B. T. Hang, T. Ohnishi, M. Osada, T. Sasaki, *Solid State Ionics* **2012**, *225*, 594.

[99] A. Glass, K. Nassau, *J. Appl. Phys.* **1980**, *51*, 3756.

[100] a) F. D. Han, J. Yue, X. L. Fan, T. Gao, C. Luo, Z. H. Ma, L. M. Suo, C. S. Wang, *Nano Lett.* **2016**, *16*, 4521; b) X. Y. Yao, D. Liu, C. S. Wang, P. Long, G. Peng, Y. S. Hu, H. Li, L. Q. Chen, X. X. Xu, *Nano Lett.* **2016**, *11*, 7148.

[101] A. Banerjee, K. H. Park, J. W. Heo, Y. J. Nam, C. K. Moon, S. M. Oh, S. T. Hong, Y. S. Jung, *Angew. Chem., Int. Ed. Engl.* **2016**, *55*, 9634.

[102] I. H. Chu, C. S. Kompella, H. Nguyen, Z. Y. Zhu, S. Hy, Z. Deng, Y. S. Meng, S. P. Ong, *Sci. Rep.* **2016**, *6*, 33733.